

**Measurement of the  $W$  mass using  
semi-leptonic events at LEP**



# Measurement of the $W$ mass using semi-leptonic events at LEP

Een wetenschappelijke proeve op het gebied van de  
Natuurwetenschappen, Wiskunde en Informatica

Proefschrift

ter verkrijging van de graad van doctor  
aan de Radboud Universiteit Nijmegen  
op gezag van de rector magnificus prof. mr. S.C.J.J. Kortmann  
volgens besluit van het College van Decanen  
in het openbaar te verdedigen op donderdag 20 maart 2008  
om 13:30 uur precies

door

Joana Ferreira Montenegro

geboren op 4 april 1977  
te Rio de Janeiro, Brazilië

Promotor: Prof. dr. N. de Groot  
Co-Promotor: Dr. J. Timmermans

Manuscriptcommissie: Prof. dr. H. Falcke  
Dr. F. Filthaut  
Prof. dr. M. Merk

ISBN: 90-6464-509-4

The work described in this thesis is part of the research program of the ‘Nationaal Instituut voor Kernfysica en Hoge-Energie Fysica’ (NIKHEF). The author was financially supported by the ‘Stichting voor Fundamenteel Onderzoek der Materie’ (FOM).

Cover: photo and design by Elisa de Magalhães, concept Elisa de Magalhães and Joana Montenegro. Based on the work of Elisa de Magalhães.

*Para minha mãe<sup>†</sup>*



# Contents

<b>1</b>	<b>Introduction</b>	<b>1</b>
<b>2</b>	<b>Theory</b>	<b>3</b>
2.1	The Standard Model . . . . .	3
2.2	The electroweak theory . . . . .	4
2.2.1	The Higgs boson . . . . .	5
2.2.2	The Higgs mass and the W mass . . . . .	6
2.3	W physics and the Standard Model . . . . .	7
2.3.1	WW production . . . . .	7
2.3.2	WW cross-section . . . . .	8
2.3.3	W decay . . . . .	10
2.4	Theoretical uncertainties . . . . .	11
2.4.1	Electroweak radiative corrections . . . . .	11
2.4.2	Fragmentation and hadronisation . . . . .	14
2.4.3	Colour Reconnection . . . . .	15
2.4.4	Bose-Einstein Correlations . . . . .	16
2.5	Event generation . . . . .	16
<b>3</b>	<b>Setup</b>	<b>19</b>
3.1	The LEP machine . . . . .	19
3.1.1	The accelerator chain . . . . .	19
3.1.2	LEP Beam Energy Model . . . . .	20
3.2	The DELPHI detector . . . . .	22
3.2.1	Tracking system . . . . .	22
3.2.2	Calorimetry . . . . .	25
3.2.3	Other sub-detectors . . . . .	26
3.3	The trigger and the offline processing . . . . .	26
3.3.1	The trigger . . . . .	26
3.3.2	The offline processing . . . . .	26
3.4	Luminosity measurement and data-taking in 2000 . . . . .	27

<b>4</b>	<b>Event selection</b>	<b>29</b>
4.1	Track selection . . . . .	29
4.2	Hadronic pre-selection and lepton identification . . . . .	30
4.2.1	Electron identification . . . . .	30
4.2.2	Muon identification . . . . .	31
4.3	Tau identification . . . . .	31
4.4	WW pre-selection . . . . .	32
4.5	Discriminant analysis . . . . .	32
4.5.1	The method . . . . .	34
4.6	Application to the selection of semi-leptonic events . . . . .	36
4.7	Selection performance . . . . .	47
<b>5</b>	<b>W mass analysis</b>	<b>51</b>
5.1	The constrained fit . . . . .	51
5.1.1	Jet and lepton parameterisation . . . . .	52
5.1.2	Jet breadth . . . . .	54
5.2	Jet clustering . . . . .	54
5.3	The Ideogram method . . . . .	55
5.3.1	First steps for building the event likelihood . . . . .	56
5.3.2	Event purity calculation . . . . .	56
5.3.3	Building a 2-dimensional ideogram . . . . .	58
5.3.4	Ambiguity in the tau channel . . . . .	59
5.4	Extracting the W mass . . . . .	60
5.5	Calibration curves . . . . .	62
5.6	Pull distribution . . . . .	64
5.7	Impact of the selection on the W mass measurement . . . . .	65
5.8	Results . . . . .	66
<b>6</b>	<b>Systematic Uncertainties</b>	<b>69</b>
6.1	Detector effects . . . . .	69
6.1.1	Muon inverse momentum scale . . . . .	70
6.1.2	Difference between $\mu^+$ and $\mu^-$ inverse momentum . . . . .	71
6.1.3	Muon inverse momentum resolution . . . . .	72
6.1.4	Electron energy scale . . . . .	73
6.1.5	Electron energy resolution . . . . .	74
6.1.6	Electron energy linearity . . . . .	75
6.1.7	Tau reconstruction . . . . .	76
6.1.8	Jet energy scale . . . . .	76
6.1.9	Jet energy resolution . . . . .	78
6.1.10	Jet energy linearity . . . . .	79

6.1.11	Forward tracks correction . . . . .	81
6.1.12	Aspect ratio . . . . .	82
6.2	Mixed Lorentz Boosted Zs (MLBZ) . . . . .	83
6.2.1	The Z samples and the Z tag . . . . .	83
6.2.2	Generating the MLBZs . . . . .	85
6.2.3	Results and “error on the error” . . . . .	85
6.2.4	Coverage of the MLBZs . . . . .	86
6.3	Electroweak radiative corrections . . . . .	87
6.3.1	Initial State Radiation . . . . .	88
6.3.2	Non factorisable corrections . . . . .	88
6.3.3	Final State Radiation . . . . .	88
6.3.4	4-fermion background diagrams: single W . . . . .	88
6.3.5	Ambiguities in the Leading Pole Approximation definition . . . . .	89
6.4	Background description . . . . .	90
6.5	LEP beam energy measurement . . . . .	90
<b>7</b>	<b>Final results and conclusions</b>	<b>93</b>
7.1	Correlations . . . . .	93
7.2	Results and combination . . . . .	94
7.3	Conclusions and outlook . . . . .	95
<b>A</b>	<b>Selection variables</b>	<b>99</b>
A.1	Variables at 189 GeV and 206 GeV . . . . .	99
<b>B</b>	<b>Event-by-event purity</b>	<b>119</b>
	<b>Bibliography</b>	<b>121</b>
	<b>Summary</b>	<b>127</b>
	<b>Samenvatting</b>	<b>129</b>
	<b>Acknowledgements</b>	<b>131</b>



# Chapter 1

## Introduction

The Standard Model of elementary particle physics is the theory which describes the interactions between fundamental particles at distances of less than one attometer ( $10^{-18}\text{m}$ ). Since its inception, almost 40 years ago it has been the subject of an impressive experimental program to challenge its validity. So far the Standard Model has withstood all tests.

Perhaps the life of the high energy physicists would be a lot more exciting if large deviations from the Standard Model predictions would be found. But this has not happened so far. Thousands of physicists analysed many millions of events taken in different experiments and in the end there are no statistically significant deviations observed. Maybe it is because particles do interact in a pretty standard way after all.

The Large Electron Positron (LEP) collider was in operation for almost 12 years at CERN near Geneva. At the first stage, from 1989 until 1995, which was known as LEP-1, many precision measurements were performed around the Z resonance. The Z boson and its charged counterpart the W boson are the carriers of the weak interaction. At the next stage, called LEP-2, the accelerator was operated at higher energies, which allowed the production of events containing a pair of W bosons. The higher energies also enabled the search for the Higgs boson and processes beyond the Standard Model to widen. At the end of 2000 LEP was shut down to make room for the next generation collider, the Large Hadron Collider. Up until this moment all results produced with the data collected at LEP only ratified the Standard Model. The work described in this thesis contributes one more grain of sand to the large pile of results that corroborate the validity of the Standard Model.

The subject of this thesis is the direct measurement of the mass of the W boson in semi-leptonic events. In this kind of events one of the two W bosons decays into a quark and an anti-quark and the other decays into a lepton and its neutrino. This measurement was performed using the data collected by the DELPHI experiment at LEP. A precision measurement of the mass of the charged carrier of the weak interaction, the W boson, is in itself a very relevant measurement. Besides that it provides a test of the Standard Model, which as mentioned above, has been extensively tested. A precise knowledge of the W mass enables an improved prediction of the mass of the much searched for Higgs boson, the one particle

in the Standard Model which has not yet been observed.

The outline of this thesis is as follows. Chapter 2 will give a short overview of the relevant theoretical background for measuring the W mass. It will give a brief introduction on the Standard model, concentrating on the electroweak sector. Chapter 3 describes the experimental setup with which data was collected. It includes a description of the LEP accelerator and of the DELPHI experiment. In Chapter 4 the selection of WW semi-leptonic events is described. Chapter 5 goes into the details of the analysis method used to extract the W mass and it presents the results found for the various centre-of-mass energies analysed. After that in chapter 6 comes an extensive discussion of the possible systematic uncertainties that might affect the measurement as well as an estimate of the magnitude of these uncertainties. Finally chapter 7 shows the combined results, for all centre-of-mass energies and discusses the validity of the results.

# Chapter 2

## Theory

### 2.1 The Standard Model

The Standard Model is the theory that describes the properties of the fundamental constituents of matter and how they interact. These constituents are called fermions, spin-1/2 particles. Fermions can be divided in leptons and quarks. The leptons and quarks are classified in families. Their quantum numbers can be seen in table 2.1. The first lepton discovered was the electron, by Thomson in 1897. The last of them was the tau neutrino, which was directly observed at the DONUT experiment at Fermilab in 2000.

There are four interactions present in nature, weak, strong, electromagnetic and gravitational (the gravitational force is negligible at the scale relevant for this thesis). Each interaction is mediated by a gauge boson. Gluons are the mediators of the strong interaction, photon exchange characterises an electromagnetic interaction and finally Z and W bosons are the carriers of the weak force. In this chapter we will concentrate on the description of the electroweak interaction which is the most relevant for this thesis.

Fermion families				Electric charge	Weak Isospin
Quarks	u	c	t	$+\frac{2}{3}$	$+\frac{1}{2}$
	d	s	b	$-\frac{1}{3}$	$-\frac{1}{2}$
Leptons	$\nu_e$	$\nu_\mu$	$\nu_\tau$	0	$+\frac{1}{2}$
	e	$\mu$	$\tau$	-1	$-\frac{1}{2}$

Table 2.1: *The table shows the Standard Model fermion families and some of their corresponding quantum numbers. The weak isospin numbers quoted are actually the third component of the weak isospin for the left hand chirality state.*

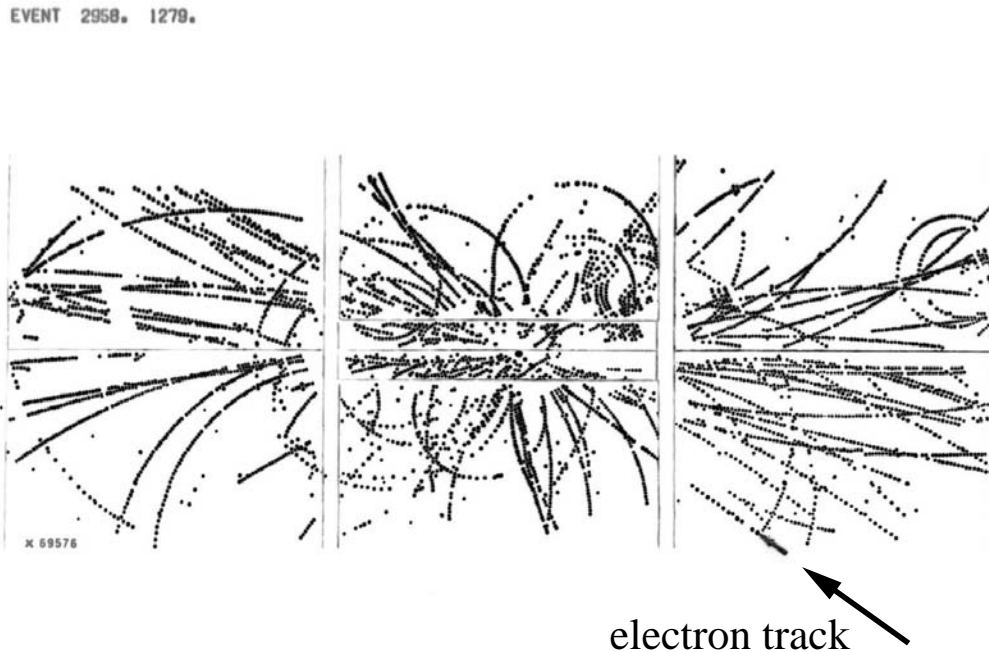


Figure 2.1: A  $W \rightarrow e\nu$  event recorded in the UA1 detector. The arrow, bottom right, points to the track of a high  $p_T$  electron from  $W$  decay.

## 2.2 The electroweak theory

Fermi was the first one to formulate a theory that tried to explain the  $\beta$  decay in 1933. He described it as a 4-point interaction with strength  $G_F$ . Soon after that, in 1934, Yukawa proposed the existence of the weak mediator. This would be the same mediator he had proposed for the strong interaction. It was Klein, a couple of years later, who stated this mediator should have spin-1 instead of spin-0 like Yukawa had thought. In 1957 Lee and Yang proposed that parity violation would be observed in weak interactions, which was in agreement with the currently accepted V-A structure of the couplings. This was confirmed experimentally later that year. In 1964 the spontaneous symmetry breaking mechanism that gives masses to the bosons was proposed by Higgs, Englert and Brout [1]. At the end of the sixties Glashow, Weinberg and Salam [2] managed to unify the weak and the electromagnetic interactions into a non-abelian gauge theory. The introduction of neutral currents made it possible for the theory to become renormalisable. The renormalisability of the theory was proven by 't Hooft and Veltman in 1972 [3]. In 1973 at the Gargamelle experiment [4] at CERN the neutral currents were finally observed. In 1983 the W and Z bosons were observed for the first time by the UA1 and UA2 experiments [5, 6] also at CERN. Figure 2.1 shows an event recorded by UA1, the electron track corresponds to a high transverse momentum

electron which is a decay product from the W boson.

### 2.2.1 The Higgs boson

The Standard Model describes the particles as if they were massless. In order to introduce mass in the theory one has to break the Electroweak symmetry and this is what the Higgs mechanism does. Below we will briefly describe how this happens. When introducing a new complex scalar field to break the symmetry, the bosons will acquire mass, this is known as the Higgs mechanism. A new complex scalar doublet  $\Phi$  is introduced in the theory: the Higgs field. The energy potential associated with this field can be written as:

$$V(\Phi) = \mu^2|\Phi|^2 + \lambda|\Phi|^4 \quad (2.1)$$

with two free parameters,  $\mu$  and  $\lambda$ , where  $\lambda > 0$ . When  $\mu^2 < 0$  the minimal potential that defines the vacuum is given by the condition:

$$|\Phi|^2 \equiv -\frac{\mu^2}{2\lambda} = \frac{1}{2}v^2 \quad (2.2)$$

where  $v$  is the vacuum expectation value. There are an infinite amount of configurations that satisfy 2.2, when choosing a minimum the symmetry is broken. When this happens two out of four degrees of freedom of the Higgs field give masses to the W bosons. The other two are not mass terms. However one can make two linear combinations of them, which will lead to a mass term and that gives mass to the Z boson and the other will be a massless term which is associated with the photon:

$$m_W = \frac{1}{2}vg \quad (2.3)$$

$$m_Z = \frac{vg}{2 \cos \theta_W} \quad (2.4)$$

$$m_\gamma = 0 \quad (2.5)$$

where  $g$  is the the weak coupling constant and  $\theta_W$  is known as the electroweak mixing angle which is a free parameter in the theory. The fermions also acquire mass by coupling to the Higgs field. This is done by imposing a Yukawa coupling between the Higgs scalar field and the fermions. The mass term is:

$$m_f = g_f \frac{v}{\sqrt{2}} \quad (2.6)$$

where  $g_f$  is a coupling constant specific to each fermion and it is a free parameter.

The Higgs boson is the only particle in the Standard Model which has not yet been observed and its existence is excluded for masses below 114.4 GeV at 95%CL [7].

## 2.2.2 The Higgs mass and the W mass

At tree level the following expressions for the W and Z masses can be derived:

$$m_W = \cos \theta_W \cdot m_Z = \frac{1}{\sin \theta_W} \sqrt{\frac{\pi \alpha}{\sqrt{2} G_F}} \quad (2.7)$$

where  $\alpha$  is the electromagnetic coupling. However the high experimental precision calls for a more accurate description of the theory. By taking into account electromagnetic and weak radiative corrections equation 2.7 becomes:

$$m_W^2 \left(1 - \frac{m_W^2}{m_Z^2}\right) = \frac{\pi \alpha}{\sqrt{2} G_F} \cdot \frac{1}{1 - \Delta r} \quad (2.8)$$

where  $\Delta r$  represents all the modifications due to higher order corrections. The correction  $\Delta r$  can be split into two separate contributions,  $\Delta \alpha$ , the electromagnetic component and  $\Delta r_w$ , the weak component:

$$\frac{1}{1 - \Delta r} = \frac{1}{1 - \Delta \alpha(m_Z^2)} \cdot \frac{1}{1 - \Delta r_w} \quad (2.9)$$

$\Delta \alpha(m_Z^2)$  is the contribution due to the photon self-energy. The strength of the coupling depends on the scale  $s$ :

$$\alpha(s) = \frac{\alpha(0)}{1 - \Delta \alpha(s)} \quad (2.10)$$

$\alpha$  is therefore referred to as a running coupling. All charged fermions contribute to  $\Delta \alpha(s)$ :

$$\Delta \alpha = \Delta \alpha_{leptons} + \Delta \alpha_{5quarks} + \Delta \alpha_{top} \quad (2.11)$$

All three contributions, namely, the one from the leptons, the one from the light quarks and the one from the top quark can be calculated and at the  $m_Z$  scale  $\alpha(s)$  becomes [8]:

$$\frac{1}{\alpha(m_Z^2)} = 128.940 \pm 0.048 \quad (2.12)$$

The terms contributing to  $\Delta r_w$  are the vacuum polarisation, vertex and box corrections. An example of one of the contributions to  $\Delta r_w$  is shown in figure 2.2 where one can see the corrections to the W propagator due to the Higgs boson, bottom and top quarks. A rigorous description of all terms contributing to  $\Delta r_w$  is outside the scope of this thesis. However, what is of interest is to know how  $\Delta r_w$  depends on  $m_H$  and on  $m_t$ . In order to illustrate that, here follows an approximate formula for  $\Delta r_w$  where  $m_H \gg m_W$  is assumed [9]:

$$\begin{aligned} \Delta r_w = & -\frac{G_F m_W^2}{8\sqrt{2}\pi^2} \left[ 3 \cot^2 \theta_W \frac{m_t^2}{m_W^2} + 2(\cot^2 \theta_W - \frac{1}{3}) \ln \frac{m_t^2}{m_W^2} \right. \\ & \left. - \frac{11}{3} \ln \frac{m_H^2}{m_W^2} + \frac{4}{3} \ln \cos^2 \theta_W + \cot^2 \theta_W + \frac{41}{18} + \dots \right]. \end{aligned} \quad (2.13)$$

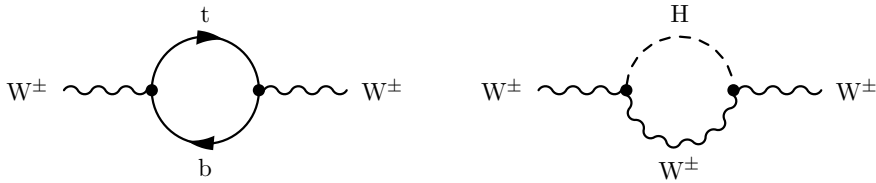


Figure 2.2: *Feynman diagrams representing the self energy corrections to the W propagator involving the Higgs boson and the bottom and top quarks*

From relation 2.13 one can observe that a precise knowledge of the W mass and the top mass helps constraining the Higgs mass. First of all one can verify if the relation 2.13 holds, which is a test of the standard model. One should notice the quadratic dependence of  $\Delta r_w$  on  $m_t$ , which means that  $\Delta r_w$  is quite sensitive to changes in  $m_t$ . On the other hand the dependence on  $m_H$  is logarithmic hence compared to  $m_t$  the uncertainty on  $m_H$  from indirect determination will be much larger. In figure 2.3 one can see a plot which illustrates how a precise knowledge of  $m_t$  and  $m_W$  can constrain the Higgs mass. The figure shows the top mass on the  $x$  axis and the W mass on the  $y$  axis. The two ellipses represent the 68% confidence level limit on  $m_t$  and  $m_W$ . The full line one uses only the LEP-1 and the SLD Z lineshape and asymmetries data (indirect measurement) and the dashed one uses the LEP-2 and the Tevatron data (direct measurement). The diagonal lines represent the theoretical dependence of  $m_W$  versus  $m_t$  for three different values of the Higgs mass.

## 2.3 W physics and the Standard Model

### 2.3.1 WW production

In  $e^+e^-$  collisions W pairs can be produced through 4 Feynman diagrams, via photons, neutrino, Z and Higgs exchange which are shown in figure 2.4. The latter is suppressed with respect to the other ones. The remaining three are known as the CC03 diagrams.

The W pair production at  $e^+e^-$  colliders is very advantageous compared to the production at  $p\bar{p}$  machines, because the background level is low. Besides that, the centre-of-mass energy is known which allows full reconstruction of the event kinematics. There are two different possibilities to measure the W mass in  $e^+e^-$  collisions. One of them is measuring the cross-section near threshold and extracting the mass from this measurement (this is not included in this thesis). The other is the direct reconstruction of the decay products of the W bosons which is the one done in this thesis and will be discussed in greater detail in the following chapters.

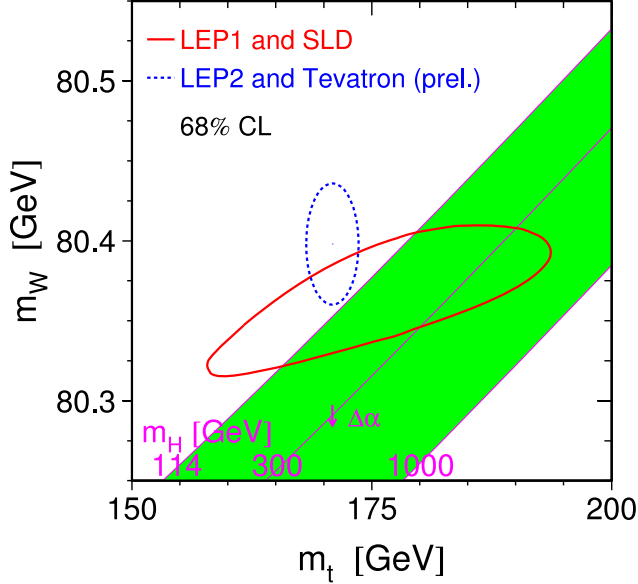


Figure 2.3: A plot of the top mass versus the  $W$  mass which shows the current constraints on the Higgs mass due to the knowledge of these two observables.

### 2.3.2 WW cross-section

The cross-section around threshold is dominated by the  $t$ -channel contribution. At a higher energy the  $s$ -channel contribution becomes more significant as can be seen in figure 2.5. The calculation at Born level assumes zero width and no radiative corrections. However we know the  $W$  bosons are unstable particles and hence have a finite width. Once the finite width is taken into account the shape of the cross-section changes. As can be seen in figure 2.6, it leads to a smoother rise of the cross-section at threshold. The leading order cross-section for off-shell  $W$  boson resonances with finite width can be written as:

$$\sigma(s) = \int_0^{s_1} ds_1 \int_0^{(\sqrt{s}-\sqrt{s_1})^2} ds_2 \rho(s_1) \rho(s_2) \sigma_0(s, s_1, s_2) \quad (2.14)$$

where  $s_1$  and  $s_2$  are the virtualities of the two  $W$  bosons and  $\rho(s)$  is a relativistic Breit-Wigner.

$$\rho(s) = \frac{1}{\pi} \frac{s}{(s - m_W^2)^2 + m_W^2 \Gamma^2(s)} \quad (2.15)$$

where  $\Gamma(s)$  is given by:

$$\Gamma(s) = \frac{s}{m_W^2} \Gamma_W. \quad (2.16)$$

This definition of  $\Gamma$  as a function of the scale  $s$  is called the running width and it is used to take into account higher order electroweak corrections. This is the same approach used at

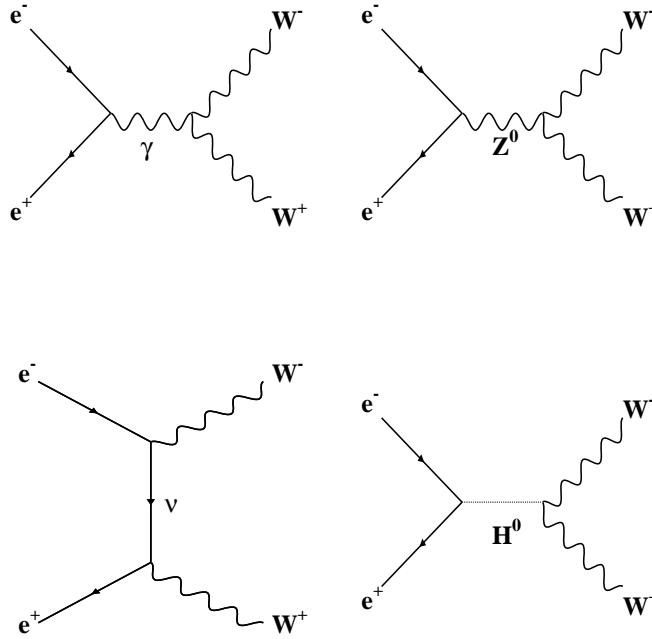


Figure 2.4:  $e^+e^- \rightarrow W^+W^-$  Feynman diagrams. The two diagrams on top are referred to as *s-channel*, the one on the bottom left as *t-channel*, while the right bottom one is suppressed.

LEP-1 for the Z lineshape. If one considers the width to be fixed with respect to the scale  $s$  the relativistic Breit-Wigner can be written as:

$$\bar{\rho}(s) = \frac{\bar{\Gamma}}{\pi \bar{m}} \frac{s}{(s - \bar{m}_W^2)^2 + \bar{m}_W^2 \bar{\Gamma}^2(s)}. \quad (2.17)$$

Around the pole the equivalent mass and width are related to those in equation 2.15 by the following expressions:

$$\begin{aligned} \bar{m} &= m_W - \frac{\Gamma_W^2}{2m_W} = m_W - 26.9 \text{ MeV} \\ \bar{\Gamma} &= \Gamma_W - \frac{\Gamma_W^3}{2m_W^2} = \Gamma_W - 0.7 \text{ MeV}. \end{aligned} \quad (2.18)$$

The inclusion of the ISR in the total cross-section determination will also change the shape of the cross-section, it basically decreases the cross-section as a whole, as can also be seen in figure 2.6.

The cross-section results for WW production at LEP can be seen in figure 2.7, the dots represent the measurements and the curves represent the theoretical predictions.

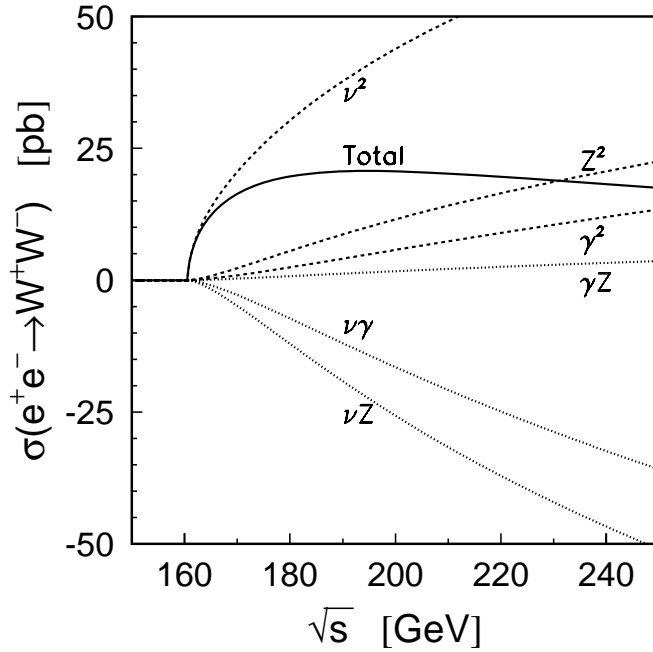


Figure 2.5: Contribution of CC03 diagrams and their interferences to  $e^+e^- \rightarrow W^+W^-$  cross section as a function of  $\sqrt{s}$ .

### 2.3.3 W decay

A W boson can decay into a pair of quarks,  $q\bar{q}$  or into a lepton and its neutrino,  $l\nu_l$ . The final state is formed by four fermions, which are the decay products of the two W bosons. There are three possible configurations, fully hadronic final state, when both W's decay hadronically, semi-leptonic, when one W decays into  $l\nu_l$  and the other into  $q\bar{q}'$  and finally the fully-leptonic, when both W's decay into a lepton and its neutrino. The branching fractions of the final state are as follows:

- fully hadronic: 45.6%
- semi-leptonic: 43.9%
- fully-leptonic: 10.5%

In this thesis the only channel studied is the semi-leptonic channel. The fully hadronic channel also plays an important role in the measurement of the W mass. The fully-leptonic one is not a useful one as the missing energy in this channel is very high making it impossible to reconstruct the event kinematics.

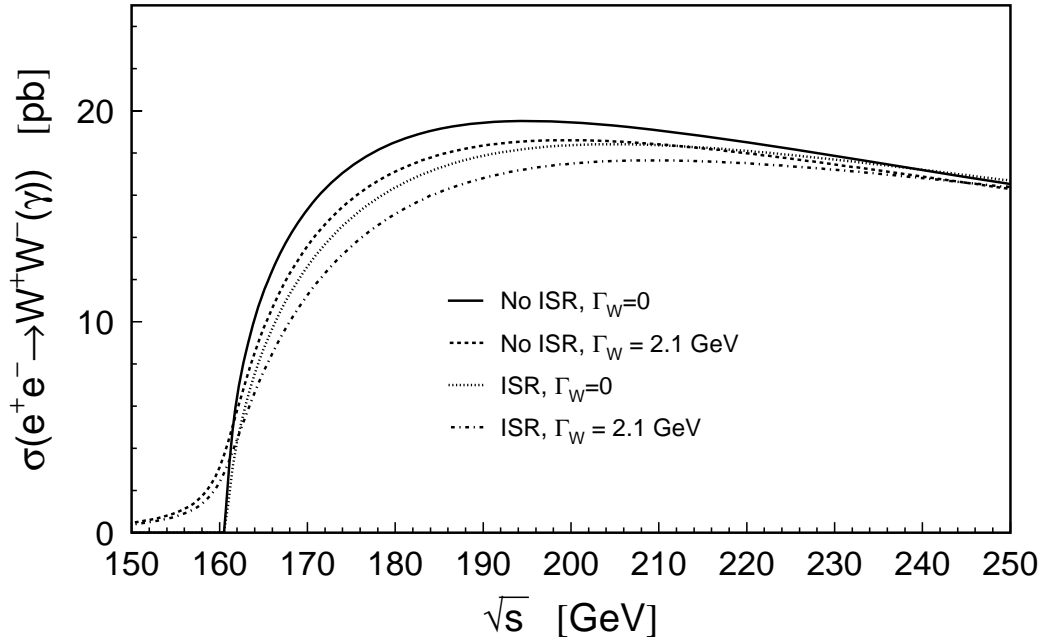


Figure 2.6: *Effects of the finite  $W$  width and ISR corrections on the total CC03 cross section for  $e^+e^- \rightarrow W^+W^-$ .*

## 2.4 Theoretical uncertainties

### 2.4.1 Electroweak radiative corrections

The model accuracy of electroweak radiative corrections in the Monte Carlo generators is of great importance to the  $W$  mass measurement. The possible sources of systematic uncertainties will be briefly discussed here. The magnitude of the uncertainties as well as the methods used to extract them are discussed in section 6.3.

The Monte Carlo generators used in the past included only the universal electroweak corrections such as Coulomb corrections, initial state radiation and final state radiation. The precision achieved by these generators on the estimate of the  $WW$  cross-section was typically 2%. However already at that time the experimental precision was about 1%. Hence it was clear that there was a need for improvement in the theoretical side. In 2000 calculations implementing full  $\mathcal{O}(\alpha)$  electroweak radiative corrections for four fermion events in the so-called Double Pole Approximation (DPA) [10] were made available by the theory community. The two Monte Carlo generators which implemented these calculations are

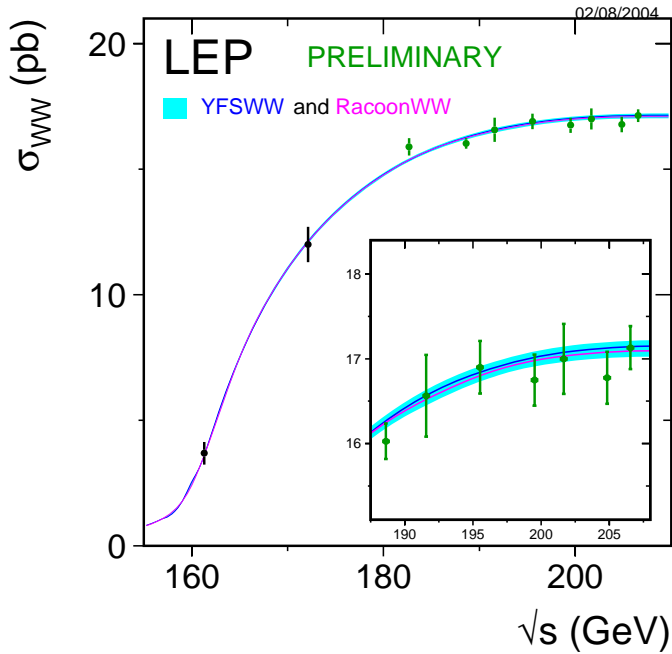


Figure 2.7:  $WW$  production cross-section results for the four LEP experiments combined. The points represent the data and the lines represent the predictions from the two Monte Carlo generators, YFSWW and RacoonWW.

RacoonWW [11] and YFSWW [12].

### Initial State Radiation (ISR)

ISR plays a very important role in the  $W$  mass measurement since it can influence the effective centre-of-mass energy. Real photons as well as virtual photon exchange [13] have to be taken into account. In first approximation the effect of ISR can be factorised as the convolution of a radiator function with a cross-section at the effective centre-of-mass energy  $\sqrt{s'}$ . There are several programs which implement ISR in this fashion in the Monte Carlo generators. In the DELPHI collaboration this was done using the YFS exponentiation approach [14] which uses leading logarithm  $\mathcal{O}(\alpha^3)$  matrix elements.

### Non-factorisable corrections

The virtual corrections can be divided in factorisable and non-factorisable ones. The first are the ones associated to either the  $W$ -pair production or the  $W$ -boson decay while for the latter the production and decay do not occur independently. For the non-factorisable corrections

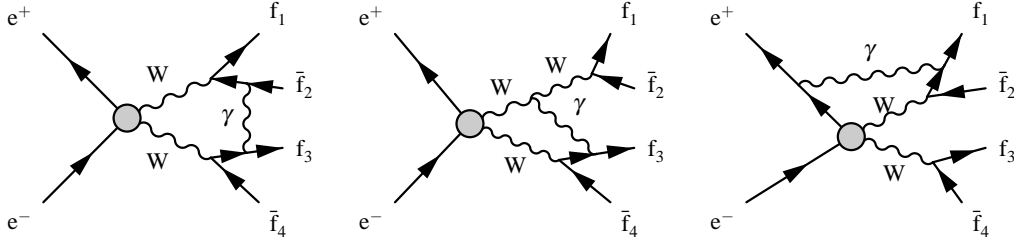


Figure 2.8: Examples of virtual non-factorisable radiative corrections in  $W$  pair production

the photon links two different subprocesses as can be seen in figure 2.8. The virtual photon exchange between  $W$ 's is referred to as Coulomb corrections. The non-factorisable  $\mathcal{O}(\alpha)$  corrections are implemented in DELPHI through the so-called Khoze-Chapovsky ansatz [15].

### Final State Radiation (FSR)

The description of Final State Radiation is very much dependent on the final state in question. Consider for example quarks in the final state. In this case radiation of photons happens most likely in the direction of the quark itself and therefore it will be included in the jet. The quarks can radiate both photons and gluons and a rigorous approach would require both processes to be described in a single process. This makes it impossible to separate FSR from the fragmentation process and one can consider that this uncertainty is already included in the fragmentation uncertainty. In DELPHI for leptons in the final state FSR is treated with PHOTOS [16] which includes leading  $\log \mathcal{O}(\alpha^2)$  photon emission.

### Radiative corrections on 4-f background diagrams: single $W$

The double pole approximation is valid only within a few  $\Gamma_W$  intervals around the double resonant pole. Therefore the DPA correction is applied only to the matrix elements from CC03 diagrams and to some interference terms. This means that the uncertainty for non-CC03 diagrams and the interference terms due to radiative corrections still needs to be addressed. The ISR studies discussed above cover most of the radiative corrections uncertainty for the four fermion background diagrams, e.g., the non-CC03 part. The one exception however is the  $q\bar{q}e\nu$  final state of single  $W$  diagrams. The interference between this diagram and the CC03 is sizeable and will therefore affect the  $W$  mass measurement.

### Ambiguities in Leading Pole Approximation definition

Two effects need to be considered when using the Leading Pole Approximation. One is the effect of the missing terms in the approximation. The other is the ambiguity present in the

way of expanding the amplitude around the double resonant  $W$  pole. The assessment of the uncertainty introduced by these effects will be done in chapter 6.

## 2.4.2 Fragmentation and hadronisation

The process of how quarks react from the moment they are produced until the moment they combine themselves to form new hadrons is known as fragmentation or hadronisation. Quarks interact via the strong interaction which is described by Quantum Chromo Dynamics (QCD). The interaction between quarks and gluons can be characterised by the strong coupling  $\alpha_s$ . The strong coupling is small at the beginning of the fragmentation process where the virtuality scale  $Q^2$  is high. The scale  $Q^2$  will decrease through the fragmentation process and it will vanish asymptotically while  $\alpha_s$  will increase.

The fragmentation process can be divided into two main parts as it can be seen in figure 2.9. Before the fragmentation begins the electroweak process takes place. This process can be described by electroweak theory to a great level of precision. After that comes the first part of the fragmentation, the perturbative jet evolution, which means one can use perturbation theory to calculate what is needed. The perturbative jet evolution is well described by the Parton Shower model. In this approach the shower is seen as a sequence of branchings where the mother particle, a gluon or a quark, branches into two daughters. These daughters will branch further creating a shower like structure. The partons can split in the following ways:  $q \rightarrow qg$ ,  $g \rightarrow q\bar{q}$  and  $g \rightarrow gg$ . The shower evolves until the virtuality scale  $Q^2$  reaches a cut-off value which is normally of the order of  $1 - 2$  GeV.

The last part of the process is the non-perturbative hadronisation where the need for phenomenological models comes in. The non-perturbative hadronisation is the least understood part in the whole process. In this case the soft gluon radiation can not be calculated exactly using perturbative QCD.

There are a few models available to describe the fragmentation and hadronisation processes. The Monte Carlo programs JETSET [17], ARIADNE [18] and HERWIG [19] all use the parton shower approach for the perturbative phase. Hereby ARIADNE uses the colour dipole approach while the other two use repetitive emission from individual partons.

For the non-perturbative phase JETSET and ARIADNE use the Lund string model. In this model the quark anti-quark pair is described as if they were connected by a colour flux tube that stretches as they move apart. This tube is called a string. The string has a certain tension that increases as the pair moves apart. When the tension is too high the string breaks and this means a new quark anti-quark pair has been created.

HERWIG [19] uses a different approach for the non-perturbative phase which is known as the cluster fragmentation model. In this model the gluons which remain after the parton shower are made to decay into  $q\bar{q}$  pairs. These pairs and quark pairs from shower form colourless clusters of various masses. These clusters can decay into lighter clusters or directly into hadrons, depending on their masses.

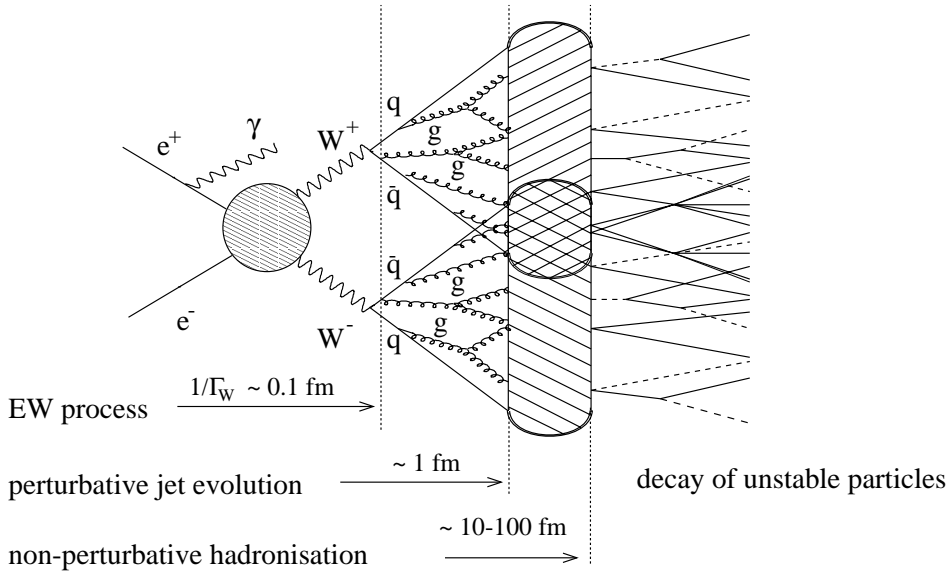


Figure 2.9: Schematic illustration of the process of fragmentation and hadronisation, see text.

All the models described above have a number of free parameters and these are used to tune the models so they describe the data. The program used to describe fragmentation in this thesis was JETSET. The other two models mentioned, HERWIG and ARIADNE were used for the systematics studies.

### 2.4.3 Colour Reconnection

In the hadronisation models described in section 2.4.2 the end products  $q_1\bar{q}_2$  and  $q_3\bar{q}_4$  of the reaction  $e^+e^- \rightarrow W^+W^- \rightarrow (q_1\bar{q}_2)(q_3\bar{q}_4)$  are treated independently. However cross-talk effects between the two colour singlets may occur. This can happen because the lifetime of a  $W$  boson is  $0.1 \text{ fm}/c$  while the hadronisation scale is of the order of  $1 \text{ fm}$ . This means that the decay products of the  $W$ 's which are originally colour singlets might interact with each other since they are decaying in the same region of space-time. This interaction can modify the properties of the final hadronic system and therefore it can influence the measurement of the  $W$  mass in the fully hadronic channel.

The effect of colour reconnection is expected to be small at perturbative level [20], however at hadronisation level the large number of soft gluons can make the effect much larger. The models available to describe Colour Reconnection in the non-perturbative phase of hadronisation rely on phenomenology. All the hadronisation models described in 2.4.2 have a Colour Reconnection option built-in. The most tested model is the Sjöstrand-Khoze I (SK-I) model [20] which is based on the Lund string model. The strings are considered

as colour flux tubes with a certain volume and the reconnection occurs when the strings overlap. The reconnection probability in an event  $\mathcal{P}_{reco}$  is parameterised as a function of the parameter  $\kappa$  which is set by the user.  $\mathcal{P}_{reco}$  is given by:

$$\mathcal{P}_{reco} = 1 - e^{-\kappa V_{overlap}} \quad (2.19)$$

where  $V_{overlap}$  is the space-time volume overlap of the two strings. The results obtained by the DELPHI collaboration for the reconnection probability are:

$$0.31 < \mathcal{P}_{reco} < 0.68 \quad (2.20)$$

at 68% confidence level with its best value at 0.52 [21]. The corresponding systematic uncertainty in W mass measurement in the fully hadronic channel amounted up to 212 MeV [22]. For a description of other Colour Reconnection models the reader is referred to references like [18], [23] and [19].

#### 2.4.4 Bose-Einstein Correlations

Bose-Einstein correlation is a purely quantum mechanical phenomenon which occurs when identical bosons (pions and kaons) are close to each other in phase-space. The net effect of Bose-Einstein correlations is that multiplets of identical bosons are produced with a smaller energy-momentum difference than non-identical ones. The effect of BEC in Z hadronic decays has been measured and it is well understood. It is natural to expect the same behaviour on single W hadronic decays. In the case of two hadronically decaying W's BEC for particles produced from the same W boson affect the normal fragmentation and are therefore treated implicitly by the fragmentation models. However it is not clear what the effect of these correlations would be if the two identical bosons in the final state came from different W's. This creates a cross-talk between the W's which may have an effect in the W mass measurement in the fully hadronic channel.

This effect is not correctly modelled in the currently available phenomenological models. The decay amplitudes are not calculated by these models, in fact what they do is to use *ad-hoc* algorithms that try to reproduce these amplitudes. The model which was used by all four LEP collaborations to implement Bose-Einstein correlations is LUBOEI [24]. A model-independent measurement of the BEC effect was also performed by the LEP experiments. The DELPHI collaboration observed a 2.4 standard deviation evidence for BEC between different W's [25]. The uncertainty due to this effect in the W mass measurement in the fully hadronic channel was found to be 31 MeV.

## 2.5 Event generation

Throughout this chapter some aspects of the event generators used in the DELPHI collaboration were described, however a more condensed description is still desirable and will

follow now. The  $W^+W^-$  events and all other four fermion processes were generated using WPHACT [26]. WPHACT was interfaced with JETSET which was used for the fragmentation process. TAUOLA [27] was used to simulate  $\tau$  lepton decay. The electroweak radiative corrections in the Double Pole Approximation were included in the generation of signal events via weights computed by YFSWW. The radiation of photons by leptons in the final state was done by PHOTOS. The main source of background in  $W^+W^-$  events comes from  $e^+e^- \rightarrow q\bar{q}(\gamma)$  events. This process was simulated by KK2f [28] interfaced again with JETSET for fragmentation. The two-photon background leading to the final states  $e^+e^-q\bar{q}'$ , not included in the four fermion generator above, was produced with PYTHIA [17]. For a complete description of the four fermion event generation in DELPHI the reader is referred to [29].



# Chapter 3

## Setup

### 3.1 The LEP machine

The Large Electron Positron collider (LEP) was operated between 1989 and 2000. The LEP ring had a circumference of 26.7 km and it was located approximately 100 m under the ground on the French-Swiss border near Geneva. It consisted of 8 straight sections which were connected by curved ones. In four of the straight sections the electron and positron beams were collided and around each interaction point a multi-purpose detector was built, namely ALEPH [30], DELPHI [31], L3 [32] and OPAL [33]. In figure 3.1 one can see the location of the experiments around the LEP ring. During the first phase of its physics program, LEP operated at the Z resonance, around 91 GeV. After 1995 the accelerator was upgraded in order to reach energies capable of producing two W bosons, this was known as the LEP-2 phase. The highest centre-of-mass energy ever reached at LEP was 209.2 GeV. At the end of year 2000, after a last effort was made to try to find the Higgs boson, the LEP accelerator was shut down for good to make room for the LHC (Large Hadron Collider).

#### 3.1.1 The accelerator chain

The machinery needed to get to the desired energies consisted of a chain of accelerators [34] that could gradually increase the energy of the electrons and the positrons until the wanted level. A schematic drawing of the injector chain can be seen in figure 3.2. The process starts with electrons being produced by an electron gun and then being accelerated up to 200 MeV in a high intensity linear accelerator, the *LEP injecteur linéaire* (LIL). The beam which comes out of the LIL hits a tungsten converter target creating the positrons. In the next step, both the electron and positron beams are accelerated in another linear accelerator up to 600 MeV. After that the electrons and positrons are accumulated in the Electron-Positron Accumulation ring (EPA). The following energy levels are achieved through acceleration at the PS and the SPS and they are respectively 3.5 GeV and 20 GeV. These are the last two

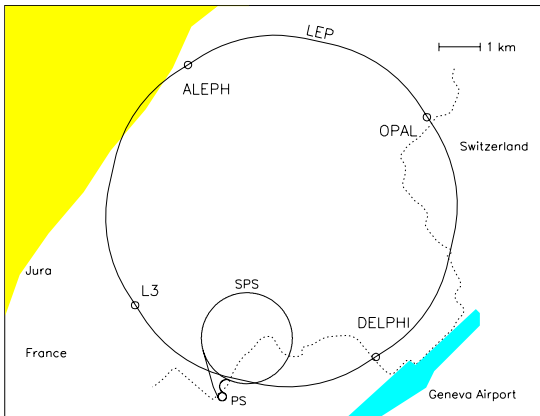


Figure 3.1: Top view of the LEP collider and storage ring. The locations of the four LEP experiments are indicated.

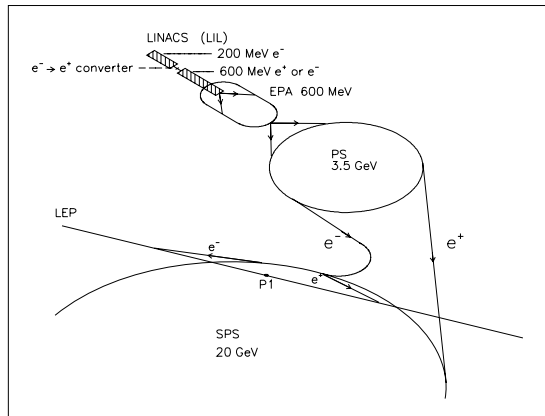


Figure 3.2: Pre-accelerator chain for the electron and positron beams.

steps before the particles are injected in the LEP ring. In the LEP ring the electrons and positrons are accelerated by RF cavities until they reach the desired energy for collision. Once the collision energy is reached the RF cavities continue to work in order to restore the energy lost by synchrotron radiation. If  $E_{beam}$  is the beam energy and  $r$  is radius of the ring, the energy lost per revolution is proportional to  $E_{beam}^4/r$ . This corresponds to a loss of approximately 2 GeV per turn at a centre-of-mass energy of 200 GeV.

### 3.1.2 LEP Beam Energy Model

A precise knowledge of the LEP beam energy is very important to set the absolute energy scale for the measurement of the  $W$  mass. The LEP Energy Working Group has been in charge of determining the centre-of-mass energy as accurately as possible. For that purpose the beam energy was measured at the four interaction points as a function of time, taking into account the precise configuration of the RF cavities and the magnets. At LEP-1 the energy was determined very precisely using a method called Resonant Depolarisation, or RDP. The technique relied on the fact that in  $e^+e^-$  storage rings the beams acquire a natural transverse polarisation due to the emission of synchrotron radiation. This polarisation can be destroyed by applying a small RF magnetic field transverse to the LEP bending field, with the RF frequency matching the spin precession frequency per revolution. The latter is proportional to the beam energy and is given by:

$$\nu = \frac{g_2 - 2}{2} \frac{E_b}{m_e c^2} \quad (3.1)$$

Where  $E_b$  is the beam energy,  $(g_2 - 2)/2$  is the anomalous magnetic moment of the electron and  $m_e$  is the mass of the electron. Since this frequency could be measured very precisely this led to a very accurate estimate of the beam energy with an uncertainty of less than 1 MeV.

Unfortunately this method could not be used for energies above 55 GeV. Because depolarisation effects increase rapidly with beam energy, the transverse polarisation of the beam becomes insufficient to perform a measurement. Hence for the LEP-2 phase the energy scale was set by a different method, the Nuclear Magnetic Resonance (NMR) model. The magnetic bending field was continuously measured by 16 NMR probes which were positioned in selected LEP dipoles. Since the beam energy is proportional to this field, one can derive the energy from such measurement. These probes were calibrated against the RDP energy measurements in the range between 41 GeV and 61 GeV. The relation between the energy and the field is assumed to be linear and in order to obtain measurements at higher energies linear extrapolation was used. The linearity of the field is the main assumption of the LEP Energy Model. On top of it the effects of the earth tide, orbit corrections, oscillations in the RF frequency and other smaller effects are also taken into account. In order to check if the linearity assumption is valid three other methods were used:

- **Flux Loop:** This method measures the field integral. Each dipole was equipped with a single-turn flux loop which provided a measurement of 96.5% of the field integral. The change in flux was measured as the machine was ramped in dedicated experiments. The field measurements were made in all years of LEP-2 running.
- **Spectrometer Magnet:** In 1999 a high quality steel dipole with a very well known magnetic field was installed in the LEP ring. The spectrometer measured the beam position at the entry and exit of the magnet. The beam energy was derived from the measurement of the bending angle of the beam in passing through the dipole.
- **$Q_s$  versus  $V_{RF}$ :** The synchrotron tune  $Q_s$  can be expressed as a function of the beam energy, the energy loss per turn and the total RF voltage  $V_{RF}$ . Since the energy loss itself depends on the beam energy the latter can be obtained by fitting  $Q_s$  as a function of  $V_{RF}$ . These measurements were performed from 1998 to 2000.

The final results for the uncertainty on the beam energy above the W threshold are shown in table 3.1. A full description of the centre-of-mass energy determination by the LEP Energy Working Group can be found in [35].

The four LEP experiments also have determined the centre-of-mass energy using radiative return to the Z events [36, 37, 38, 39]. The DELPHI analysis consisted of determining the centre-of-mass energy from radiative returns using energy and momentum constraints in the channels  $e^+e^- \rightarrow \mu^+\mu^-(\gamma)$  and  $e^+e^- \rightarrow q\bar{q}(\gamma)$ . The results obtained were compared with the measurements reported by the LEP Energy Working Group. The difference

$E_{cm}$ ( GeV)	161	172	183	189	192	196	200	202	205	207
error on $E_{beam}$ ( MeV)	12.7	13.7	10.2	10.8	10.8	11.6	11.8	11.9	18.5	20.8

Table 3.1: The top row shows the nominal centre-of-mass energy and the bottom one the corresponding error on the beam energy

in centre-of-mass energy between the DELPHI result and the LEP Energy Working group measurement was found to be:

$$\Delta E_{cm} = +0.073 \pm 0.094(Stat.) \pm 0.065(Syst.) \text{ GeV} \quad (3.2)$$

The DELPHI results are thus in agreement (albeit with large errors) with those from the LEP Energy Working Group.

## 3.2 The DELPHI detector

The DELPHI detector was located at the collision point IP8, one of the four collision points of LEP.

Here follows a description of the detector parts that were relevant for this analysis. DELPHI (DEtector with Lepton, Photon and Hadron Identification) was a  $4\pi$  general purpose detector and consisted of various sub-detectors for tracking, calorimetry and particle identification. A full description of it can be found in [40] and [41] and a schematic view of the detector can be seen in figure 3.3. The detector consisted of a barrel part which is a cylinder around the beam pipe and two end-caps to complete the  $4\pi$  solid angular coverage. Its coordinate system was right-handed, having the origin in the interaction point. The  $z$  positive axis pointed in the direction of the electron beam, the  $x$  direction pointed towards the centre of LEP and the  $y$  axis pointed up.

### 3.2.1 Tracking system

The aim of the tracking detectors is to reconstruct the 3D trajectory of the charged particles that were produced in the collision. The tracking in DELPHI was done with the Micro Vertex Detector (VD), the Inner Detector (ID), the Time Projection Chamber (TPC), the Outer Detector (OD), the Forward Chambers (FCA and FCB) and the Muon Chambers (MUC). All the above sub-detectors, with the exception of the Muon Chambers, were surrounded by a superconducting coil with a magnetic field of 1.23 T along the  $z$  axis. A brief description of each of these sub-detectors will follow.

- **Micro Vertex Detector (VD):** The micro-vertex detector was the closest one to the interaction point and consisted of two parts: the Vertex Detector (VD) for which the

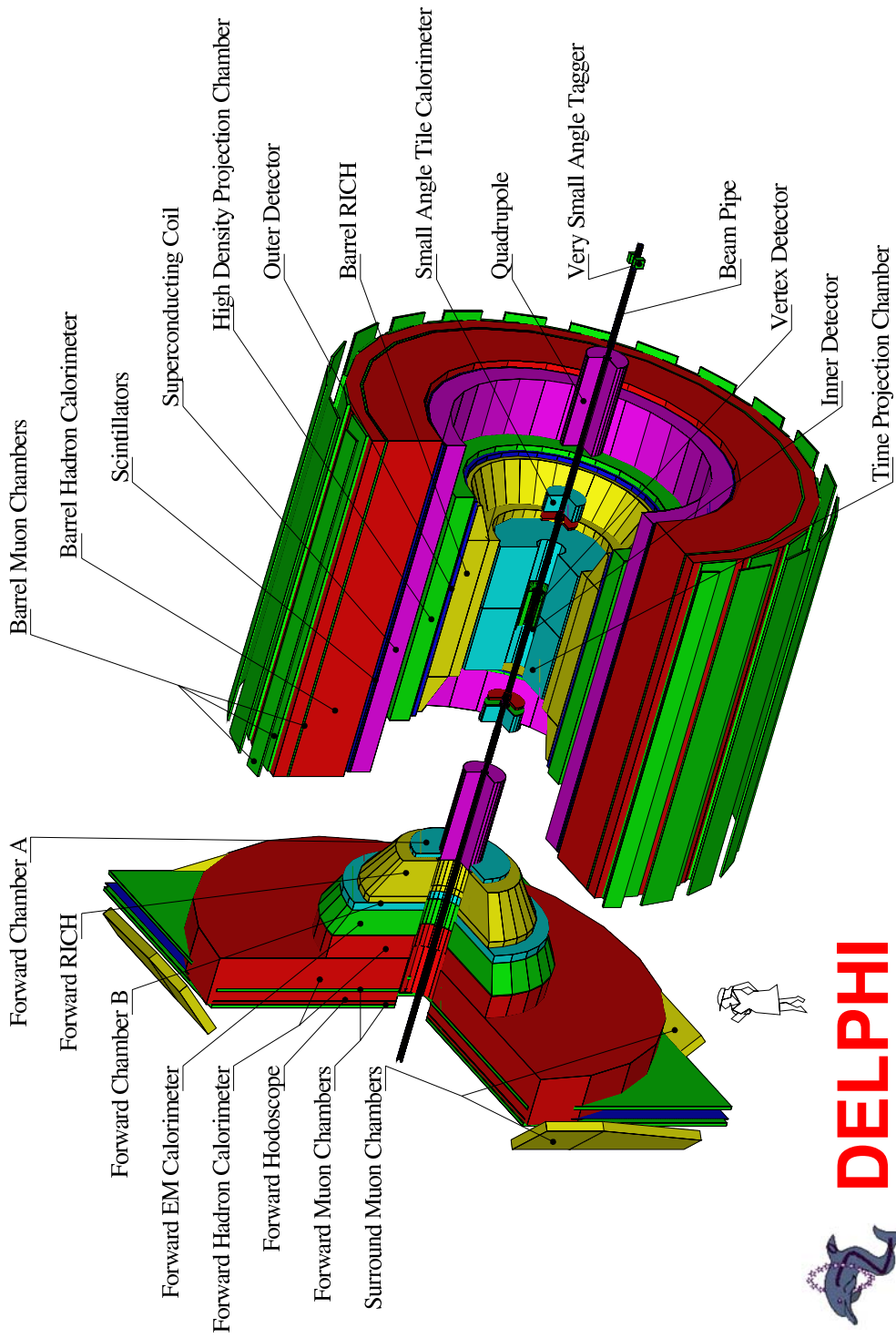


Figure 3.3: The DELPHI detector

polar angle acceptance was of  $21^\circ \leq \theta \leq 159^\circ$  and the Very Forward Tracker (VFT) which covered the angles between  $11^\circ$  and  $25^\circ$ . The VD consisted of 3 cylindrical layers of Silicon strip detectors and the average radii of these 3 layers were 6.6 cm, 9.2 cm and 10.6 cm. The single hit precision in  $R\phi$  was  $8 \mu\text{m}$  and in  $z$  it was a function of the incidence angle, reaching  $9 \mu\text{m}$  for a polar angle of  $90^\circ$ . The micro-vertex detector is essential to determine whether tracks come from primary or secondary vertices .

- **Inner Detector (ID):** The inner detector directly surrounded the VD and it was composed of two concentric shells, an inner drift chamber and a straw tube detector. The detector was used for tracking and trigger information. The ID polar angle acceptance was of  $15^\circ \leq \theta \leq 165^\circ$  and its inner and outer radii were respectively 12 cm and 28 cm. The inner drift chamber was a jet chamber and it was separated in 24 azimuthal parts each containing 24 sense wires. The straw tube detector contained 192 straws in each of its 5 layers. This detector gave additional  $R\phi$  measurements that helped solving the left-right ambiguity from the drift chamber.
- **Time Projection Chamber (TPC):** The TPC was DELPHI's main tracking device. It consisted of two drift chambers separated by a high voltage plane with an electric field parallel to the  $z$  axis. The chambers were filled with a gas mixture consisting of Argon and  $\text{CH}_4$  in the proportion of 4:1. The acceptance covered polar angles between  $20^\circ$  and  $160^\circ$  and inner and outer radii between 35 cm and 111 cm respectively. When a charged particle passed through the chamber it caused ionisation in the gas which liberated electrons, the latter drifted towards the end-plates of the detector. At the end-plates Multi Wire Proportional Chambers (MWPC) were placed, 6 of them on each end-plate. The MWPCs allowed 3D reconstruction of up to 16 points with an  $R\phi$  resolution of  $250 \mu\text{m}$ . The  $z$  information was determined from the arrival time of the particles. Its resolution was  $880 \mu\text{m}$ . Information about  $dE/dx$  was also provided by the TPC through pulse height measurement in the 192 anodes of the MWPC'S. The resolution for minimum ionising particles was 6.2%. The size of the TPC was small when compared to similar LEP main tracking detectors. This was due to the presence of the RICH detector, which was not present in the other LEP experiments.
- **Outer Detector (OD):** The Outer Detector's main purpose is to improve the momentum resolution measured by the TPC, as a compensation for the presence of the RICH. The OD comprises 5 layers of streamer drift tubes, its inner and outer radii are 197 cm and 206 cm and the polar acceptance is of  $40^\circ \leq \theta \leq 140^\circ$ . The single hit resolution in  $R\phi$  is  $110\mu\text{m}$  and 3.5 cm in  $z$ . Since the detector has a fast response it was also used for the trigger.
- **Forward Chambers (FCA and FCB):** The Forward Chambers were both placed in the end-caps. The FCA consisted of 3 half-discs made of 2 staggered layers of drift tubes operating in limited streamer mode. Their polar angle acceptance lay between

	Energy Resolution ( $E$ in $GeV$ )
HPC	$\sigma(E)/E = 0.043 \oplus 0.32/\sqrt{E}$
FEMC	$\sigma(E)/E = 0.03 \oplus 0.12/\sqrt{E} \oplus 0.11/E$
STIC	$\sigma(E)/E = 0.0152 \oplus 0.135/\sqrt{E}$
HAC	$\sigma(E)/E = 0.21 \oplus 1.12/\sqrt{E}$

Table 3.2: Energy resolution of the electromagnetic and Hadronic calorimeters

$11^\circ$  and  $32^\circ$  and between  $148^\circ$  and  $169^\circ$ . The FCB were 2 drift chambers consisting each of 12 read-out planes of wires. Their function was analogous to the OD in the barrel, *i.e.* improvement of the momentum measurement at high momentum.

- **Muon Chambers (MUB, MUF and SMC):** There were 3 muon chamber systems in the DELPHI detector, namely, the Barrel, Forward and the Surround Muon Chambers (MUB, MUF, SMC). The Muon chambers were the outermost sub-detectors in DELPHI, due to the fact that muons are one of the few particles that cross all the calorimeters without being stopped. The detection principle of these chambers is to associate the hits in them with extrapolated tracks in the previous sub-detectors. The angular coverage for the Barrel, Forward and Surround Muon Chambers was respectively  $52^\circ \leq \theta \leq 128^\circ$ ,  $9^\circ \leq \theta \leq 43^\circ$  and  $42^\circ \leq \theta \leq 53^\circ$ .

### 3.2.2 Calorimetry

A calorimeter measures the energy of a particle by absorbing it inside the detector. In DELPHI the energy of electrons and photons was measured using the electromagnetic calorimeters and the neutral and charged hadron energy using the hadronic calorimeters. The energy resolution for the electromagnetic and hadronic calorimeters is given in table 3.2. A brief description of the calorimeters follows now.

- **High density Projection Chamber (HPC)** The HPC was the last detector before the super-conducting coil, seen from the interaction point. It was a sampling calorimeter and its inner and outer radii were 208 cm and 260 cm, the polar angle acceptance was of  $43^\circ \leq \theta \leq 137^\circ$ . The detector consisted of 144 modules which were arranged in 6 rings. Each module is a small TPC containing lead layers, which served as converting material, inter-spersed with gas.
- **Forward ElectroMagnetic Calorimeter (FEMC)** The FEMC was located in the end-caps and consisted of 4532 lead glass blocks per side. The blocks were tilted about  $1^\circ$  with respect to each other in order to prevent particles from going in the dead regions of the detector. The polar angle acceptance was of  $8^\circ \leq \theta \leq 35^\circ$  and  $155^\circ \leq \theta \leq 172^\circ$ .

- **Small angle Tile Calorimeter (STIC)** The STIC was a sampling calorimeter made of lead and scintillator. It was designed to measure the energy of particles that were produced close to the beam pipe. It was placed on both sides of the interaction region, 2.2 m away from the centre and the polar angle acceptance lied between 29 mrad and 185 mrad. The STIC was used to measure the integrated luminosity from Bhabha events.
- **HAdron Calorimeter (HAC)** The Hadron Calorimeter was placed in the return yoke of the solenoid and covered most of the polar angle (between  $11^\circ$  and  $169^\circ$ ). It consisted of iron plates, 20 in the barrel and 19 in the end-caps, 5 cm thick interspersed by limited streamer mode wire chambers.

### 3.2.3 Other sub-detectors

The description of the sub-detectors that were not used in this analysis can be found in [40] and [41]. One of them for instance is the Ring Imaging Cherenkov Detector, used for particle identification and unique among LEP experiments.

## 3.3 The trigger and the offline processing

### 3.3.1 The trigger

The trigger in DELPHI was a four level system. The Beam Cross Over (BCO) rate was around 45,000 Hz and it was reduced to a few Hertz after the trigger. The level 1 and 2 were hardware triggers and were synchronous with the BCO, which occurred every  $22\mu\text{s}$ . The level 1 decision was taken  $3.5\mu\text{s}$  after BCO and it was based on raw detector information. The trigger rate was about 700 Hz. The level 2 trigger was done  $39\mu\text{s}$  after BCO and it also used raw detector info, the rate was reduced to about 10 Hz. The level 3 and 4 were software triggers and were asynchronous with the BCO. The level 3 trigger decision was similar to the level 2, but included more detailed detector information and the trigger rate was half of the level 2 one. Finally, the level 4 was an algorithm based on DELANA, the DELPHI reconstruction program, and rejected events without good tracks or not enough energy deposits, in this case the trigger rate was halved again.

### 3.3.2 The offline processing

The DELANA program processes the data coming from the various sub-detectors. The data calibrations, pattern recognition, track fitting and basic event classification are performed at this stage. The DELANA output is the Data Summary Tape (DST), which provides data

Year	centre-of-mass energy (GeV)	Luminosity ( $\text{pb}^{-1}$ )
1997	182.65	51.8
1998	188.63	152.5
1999	191.58	24.4
	195.51	74.6
	199.51	81.6
	201.64	40.2
2000	205.86	215.9

Table 3.3: Integrated luminosities collected by the DELPHI detector at various centre-of-mass energies.

that can be used for physics analyses. The analysis presented here relies upon a few DELPHI packages, namely, PHDST [42], SKELANA [43] and WWANA [44]. The first reads the information from the DST, the second makes this information available in a convenient format for doing the analysis and the latter is a package for analysis of W pairs which will be discussed in more detail further in this thesis. The detector simulation is performed by DELSIM. The particles generated by a Monte Carlo generator are passed to DELSIM, which simulates the interactions of these particles with the materials of all the sub-detectors they cross. The output goes then through the standard DELANA program.

### 3.4 Luminosity measurement and data-taking in 2000

The integrated luminosity over a data-taking period is defined as:

$$\mathcal{L} = \frac{N_{proc}}{\sigma_{proc}} \quad (3.3)$$

where  $N_{proc}$  is the number of events produced by that specific process and  $\sigma_{proc}$  the cross-section of that process. The most precise way to estimate the integrated luminosity is to choose a process with a high and well-known cross-section and with a clear experimental signature and measure  $N_{proc}$  and  $\sigma_{proc}$  for this particular process. At LEP this process was small angle Bhabha scattering. The integrated luminosities collected by the DELPHI detector in the different years of data taking are given in table 3.3.

2000 was the last year of run for the LEP experiments. In September one sector out of 12 of the DELPHI TPC stopped working. Until the end of the run the DELPHI detector was operated without this part of the main tracking device. In the table 3.4 one can see which fraction of the total luminosity was collected during this period, as well as in the rest of the time. Due to the redundancy in the DELPHI tracking system, tracks which traversed

	Luminosity( $pb^{-1}$ ) at 2000
TPC healthy	158.5
1 sector dead	57.4
total	215.9

Table 3.4: Collected luminosity in year 2000

this sector could still be reconstructed by the other tracking detectors. A different tracking algorithm was developed for this sector. This algorithm used also the reconstructed space points by the barrel RICH detector. Monte Carlo samples were produced with the same sector of the TPC switched off to be used when analysing the data without this sector of the TPC.

# Chapter 4

## Event selection

This chapter describes the selection of WW events which decay semi-leptonically. These events correspond to 43.9% of the WW decays. The largest background contribution comes from  $Z \rightarrow q\bar{q}(\gamma)$ . Other sources of background included are 4-fermion neutral current processes and two-photon collisions. The event selection described in this chapter is part of the WWANA package.

### 4.1 Track selection

The standard DELPHI track selection is applied. A track is classified as a charged track if it satisfies the cuts shown in table 4.1. Tracks that fail the charged track selection are still considered for the neutral track selection. For a track to be identified as a neutral track the energy deposition in the calorimeter has to be above a certain threshold and there should be no charged track pointing to it. The required energy depositions can be seen in table 4.2. For HCAL energy deposits an algorithm for noise rejection was applied. This algorithm was based on the energy of the shower, its number of hits and its longitudinal position. Besides the energy requirements the polar angle of the neutral cluster should be larger than  $3^\circ$ . This last cut aims at the rejection of beam related background. More details are available in reference [43].

Track momentum	$100 \text{ MeV} <  p  < 1.5 E_{beam}$
Relative momentum error	$< 1$
Impact parameter in $R\Phi$	$< 4 \text{ cm}$
Impact parameter in $z$	$< 4 \text{ cm} / \sin \theta$

Table 4.1: *Cuts required to select charged tracks.*

Calorimeter	Energy cut
HPC	$E > 0.3 \text{ GeV}$
FEMC	$E > 0.4 \text{ GeV}$
STIC	$E > 0.4 \text{ GeV}$

Table 4.2: Energy deposition cuts for the different calorimeters required for neutral track selection. The HPC is the electromagnetic calorimeter in the barrel, the FEMC is the equivalent one in the forward region and the STIC is the small angle calorimeter.

## 4.2 Hadronic pre-selection and lepton identification

The first step in selecting WW semi-leptonic events is to apply a hadronic pre-selection. The one used in this thesis is the standard DELPHI hadronic pre-selection. The events were required to have at least six charged particles and a total visible energy greater than 10% of the centre-of-mass energy. The following cut was applied to the energy deposited in the electromagnetic calorimeters in order to reject Bhabha events:

$$\sqrt{E_{for}^2 + E_{back}^2} < 0.9 \cdot E_{beam} \quad (4.1)$$

where  $E_{for}$  and  $E_{back}$  are respectively the energies recorded in the forward and backward sections of the FEMC electromagnetic calorimeter. After the hadronic pre-selection a search for leptons was made, the lepton identification procedure is described in the following sections.

### 4.2.1 Electron identification

The REMCLU package [45] was used for the electron identification. REMCLU is a package for electromagnetic cluster reconstruction designed specifically for LEP2. It treats electrons identified in the barrel region differently from the ones in the forward region.

In the barrel region tracks with a momentum less than 30 GeV are treated by the ELEPHANT [46] package. ELEPHANT is a package developed during the LEP1 phase which uses the  $dE/dx$  information measured in the TPC, the shower profile and the ratio  $E/p$  to identify the electrons. The criteria were developed to distinguish electrons from pions and are suitable for low energy electrons. The selected tracks can be tagged as ‘loose’, ‘standard’ or ‘tight’. For tracks with momentum greater than 30 GeV the REMCLU package is used. In this case the energy of radiated photons around the track is added to the energy of the track. The acceptance for the assignment is of  $\pm 2^\circ$  in the  $\theta$  direction and in the  $\phi$  direction it is asymmetric to account for the bending of the track in the magnetic field. If the energy of this cluster measured by the HPC is greater than 10 GeV and the ratio  $E/p$  is greater than 0.5 this

track is tagged as an electron. If the energy deposited in the hadron calorimeter in a  $5^\circ$  cone around the track direction exceeds 10% of the electromagnetic energy, the electron is tagged as ‘loose’, otherwise the electron is tagged as ‘tight’.

In the forward region the reconstruction efficiency is degraded due to the presence of material and the lower number of tracking layers. Electrons are identified by combining the information from the energy deposits in the FEMC crystals and matching this to track information. The procedure starts with the re-clustering of showers measured by the FEMC, which is done in order to recover information lost due to the early showering that occurs in the material in front of the FEMC. After that the information obtained is matched to track information. The direction of the cluster is replaced by the direction of the measured tracks associated to it.

### 4.2.2 Muon identification

The identification begins by checking for hits in the muon chambers. The package MUFLAG [47] is used to match these hits to tracks. The program also checks for particles that deposited energy in the hadron calorimeter (HCAL) which are consistent with minimum ionisation signature. The muon chambers are shielded by the iron in the hadronic calorimeter which accounts for a very clean environment. However some residual activity caused by the so-called punch-through pions from HCAL showers is still observed. A muon identified by the package can be flagged as ‘tight’, ‘standard’, ‘loose’ or ‘very loose’ depending on the number of hits reconstructed and the quality of the fit. This analysis used ‘very loose’ tagged muons.

## 4.3 Tau identification

Of the 3 charged leptons the tau is the most complex to identify, because of its various decay possibilities. The tau lepton can decay into one or more charged particles. About 85% of the decays are the so-called one-prong decays. In one prong decays the tau decays into a single charged particle and one or more neutral ones. The majority of the remaining taus decay into three prongs. The identification routine looks for a good isolated track. If one is found the event is identified as a 1-prong tau. If not, all tracks in the event are clustered into jets. The clustering algorithm LUCCLUS [17] was used with a  $d_{join}$  value of  $6.5 \text{ GeV}^1$ . After clustering the jets were trimmed. The trimming consisted of removing particles which were at an angle greater than  $20^\circ$  from the highest energetic particle in the jet. To be considered as a tau jet the total number of particles in the jet should not exceed 10 and the number of charged particles has to be smaller than 6. The tau candidate was then chosen by picking the jet with the smallest momentum-weighted angular spread. The momentum-weighted angular

<sup>1</sup>For the definition of  $d_{join}$  and more information on jet clustering read section 5.2

	$e$	$\mu$	narrow-jet $\tau$	one-prong $\tau$
Transverse energy(GeV)	$> 45$	$> 45$	$> 40$	$> 40$
Missing momentum(GeV)	$> 10$	$> 10$	$10 - 80$	$10 - 80$
$E_{vis}/E_{CM}(\%)$	$40 - 110$	$40 - 110$	$35 - 100$	$30 - 90$
Lepton energy(GeV)	$> 15$	$> 15$		

Table 4.3: Pre-selection cuts for each of the three semi-leptonic final states, namely,  $q\bar{q}e\nu_e$ ,  $q\bar{q}\mu\nu_\mu$  and  $q\bar{q}\tau\nu_\tau$ . The tau final state is split in narrow-jet tau and one-prong tau. The transverse energy of the event is defined as the sum of the absolute value of the momentum of all tracks in the x-y plane.  $E_{vis}$  is the total visible energy and  $E_{CM}$  the centre-of-mass energy of the event.

spread of a jet is defined as  $\sum_i (p_i \times \theta_i) / \sum_i p_i$ , where  $\theta_i$  is the angle made by the momentum  $p_i$  of the  $i^{th}$  particle in the jet with the total jet momentum. Hereafter the one-prong tau decays will be referred to as one-prong taus and the three-prong decay as narrow-jet taus.

## 4.4 WW pre-selection

A semi-leptonic event is characterised by an isolated lepton (or a low multiplicity jet, in the case of narrow-jet taus), high missing energy and two or more hadronic jets. Figure 4.1 shows an event display of a semi-leptonic  $q\bar{q}\mu\nu_\mu$  event.

A series of cuts were applied to select these events. They can be seen in table 4.3. The cut on the transverse energy aims to reject the two-photon events. The cut on the missing momentum accounts for the presence of neutrino(s) in the W decays. Obviously a cut on the visible energy itself is also required. The lower cut on  $E_{vis}$  rejects high-energy ISR events and two-photons. The higher one excludes events without missing energy. Finally a cut on the lepton energy was applied. Both muons and electrons were required to have an energy greater than 15 GeV which aims to reject leptons that are decay products of heavy quarks.

An event could be pre-selected more than once, but selected only once. Therefore all four configurations ( $q\bar{q}e\nu_e$ ,  $q\bar{q}\mu\nu_\mu$ ,  $q\bar{q}\tau\nu_\tau$  and  $q\bar{q}\tau_{1p}\nu_\tau$ ) were saved and a final decision was only taken at full selection level.

## 4.5 Discriminant analysis

The selection used in this thesis was developed for the determination of the WW cross-section at DELPHI [48]; a detailed description of it can be found in [49]. A few modifications were made for this analysis, but the majority of it remained the same. This selection

 <b>DELPHI</b> Run: 103302    Evt: 4779 Beam: 98.1 GeV    Proc: 28-Jun-1999 DAS: 28-Jun-1999    Scan: 2-Jul-1999 04:14:09    Tan+DST		TD	TE	TS	TK	TV	ST	PA			
	Act	( 0	83	0	27	0	0	0			
		( 0	X259	X	0	X	27	X	0	X	0
	Deact	( 0	0	0	0	0	0	0	0		
	( 0	X	0	X	0	X	1	X	0	X	0

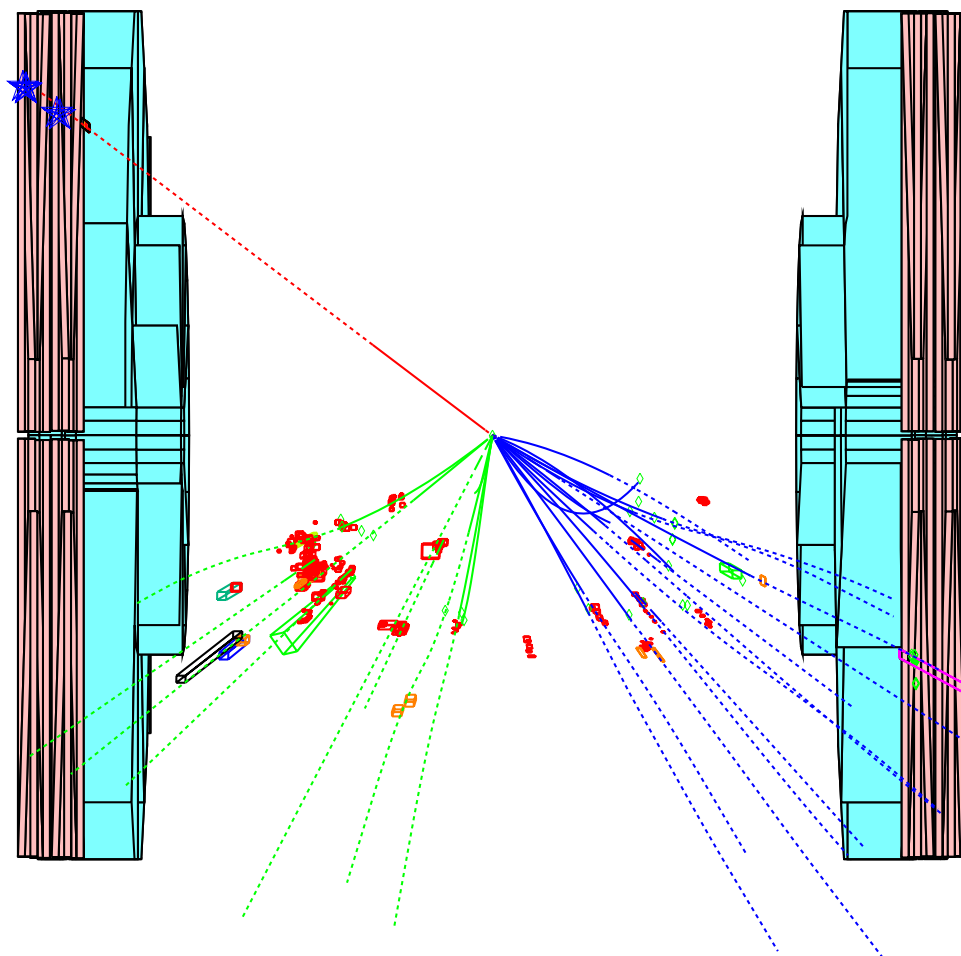


Figure 4.1: Event display in the  $R$ - $z$  projection of a  $W^+W^- \rightarrow q\bar{q}\mu\nu_\mu$  event at 196 GeV centre-of-mass energy. The isolated track represents the muon and the two clusters of tracks represent the two hadronic jets. Only the forward hadron calorimeters and the muon chambers are shown.

technique is called Iterative Discriminant Analysis (IDA). In a nutshell what it does is to construct a discriminant variable from a set of observables and this variable is later used to distinguish between signal and background.

## 4.5.1 The method

### Linear Discriminant Analysis

This section describes the simple case of the Linear Discriminant Analysis (LDA), this will later be generalised to the Polynomial Discriminant Analysis (PDA) which is the one used in this thesis. Consider a N-dimensional space where N is the number of observables. An event can be defined by a vector  $\vec{x}$  of dimension N. A population of events is described by the Probability Density Function (PDF)  $P(\vec{x})$ . There are two populations 'signal' and 'background'. Each can be described as a cluster of points in this N-dimensional space. The aim is to be able to distinguish them from each other. Their PDFs are respectively  $P_S(\vec{x})$  and  $P_B(\vec{x})$ . The goal is to find the optimal separation between the two populations. According to the Neyman-Pearson lemma [50] the optimal separation is the one which maximises efficiency times purity. This is achieved by having a N-dimensional boundary with a constant likelihood ratio:

$$\frac{P_S(\vec{x})}{P_B(\vec{x})} = \text{const.} \quad (4.2)$$

Assuming the PDFs are Gaussian (which can be generalised) with means  $\vec{x}^0$ , they can be written as

$$P(\vec{x}) \propto \exp\left[-\frac{1}{2}(\vec{x} - \vec{x}^0)^T V^{-1}(\vec{x} - \vec{x}^0)\right] \quad (4.3)$$

where  $V$  is the error matrix of the distribution. By substituting equation 4.3 into 4.2 and then taking the natural logarithm of this expression one gets

$$-(\vec{x} - \vec{x}_S^0)^T V_S^{-1}(\vec{x} - \vec{x}_S^0) + (\vec{x} - \vec{x}_B^0)^T V_B^{-1}(\vec{x} - \vec{x}_B^0) = C \quad (4.4)$$

where  $C$  is a constant and the means of the populations S and B,  $\vec{x}_S^0$  and  $\vec{x}_B^0$  and their error matrices,  $V_S$  and  $V_B$ , have been stated explicitly. Assuming that the error matrices are the same for signal and background, it can be shown [51] that the boundary can be written as

$$\vec{x}^T V^{-1}(\vec{x}_S^0 - \vec{x}_B^0) = C = \vec{x} \cdot \vec{a} \quad (4.5)$$

where  $\vec{a}$  is given by  $V^{-1}(\vec{x}_S^0 - \vec{x}_B^0)$ . Equation 4.5 defines a N-dimensional plane which has the power to discriminate between the two populations  $S$  and  $B$ . This discrimination is optimal if the assumptions made, namely the two PDFs are Gaussian and identical error matrices, hold. In case the error matrices are not identical a commonly used approach is to use the average of the two matrices. This is sometimes referred to in the literature as the Fischer discriminant.

## Polynomial Discriminant Analysis

This section discusses the more general case where the boundary which separates the two populations is no longer a plane, but a surface. It can be seen that if one substitutes equation 4.3 into 4.2 and then take the natural logarithm of it, as it was done before, but not assume equal error matrices, the optimal boundary is given by a quadratic surface.

The goal is to generalise the LDA to higher orders. In order to do that a quadratic surface in which the linear part has the same structure as the LDA will be defined

$$\vec{x}^T (\vec{a} + B\vec{x}) = C_2 \quad (4.6)$$

where  $B$  is a  $N \times N$  matrix containing coefficients of the  $x_i x_j$  and  $x_i^2$  terms in the surface. Another possibility is to express equation 4.6 as

$$\vec{b} \cdot \vec{y} = C_2 \quad (4.7)$$

in such a way that  $\vec{b}$  contains both the linear terms  $x_i$  and the quadratic terms  $x_i x_j$  and  $x_i^2$  of the new vector  $\vec{y}$ . Now equation 4.7 has the same structure as equation 4.5, therefore linear discriminant analysis can be performed in the observable space defined by  $\vec{y}$ . Equation 4.7 can be extended to higher orders the same way equation 4.5 was extended to 4.7. When doing this a new error matrix needs to be defined. It can be shown [49] that the optimal dividing surface between two Gaussian populations is in general a quadratic function of the observables. The derivation of this quadratic function can be found in reference [49].

## Reality check

As stated before, the methods described above are accurate if the assumptions made hold. One of the assumptions that was made was that the populations of signal and background were gaussianly distributed. In reality this does not happen. The distributions of events in the observable space is not Gaussian. In reference [49] one can find the description of a study performed with simulated events where  $WW \rightarrow q\bar{q}e\nu_e$  events were used as signal and  $Z \rightarrow q\bar{q}(\gamma)$  as background. The electron energy and the visible energy in the event were used to build a discriminant. The distribution of events in the electron energy - visible energy space was clearly non-Gaussian, as shown in the left plot of figure 4.2. It turns out one can define a transformation for each observable which will make the distribution of events in this space Gaussian. Therefore equation 4.3 still holds. Figure 4.2 shows the distribution of events in the electron energy - visible energy space before and after the Gaussian transformation. All the observables used in the event selection described in this thesis were transformed in order to be gaussianly distributed.

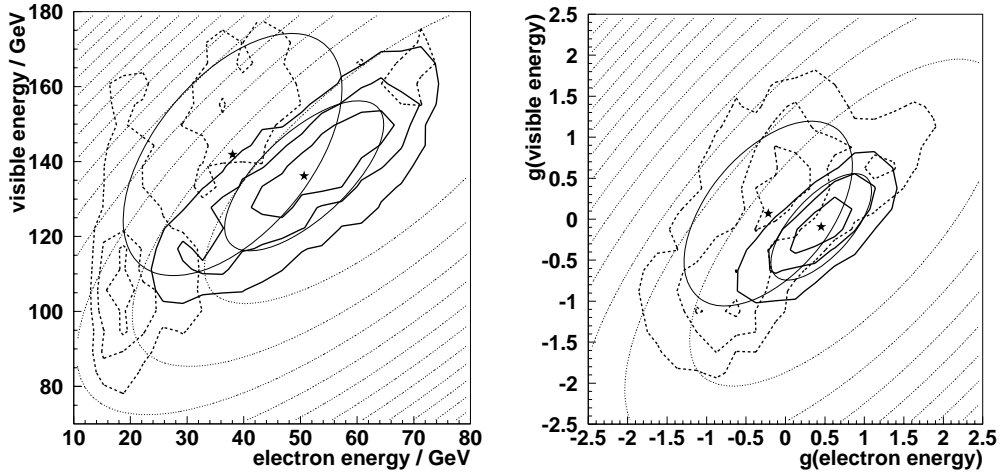


Figure 4.2: Figures taken from reference [49]. Distribution of events in the electron energy - visible energy space. The thick solid contours represent the signal and the thick dotted contours the background. The stars represent the mean of the distributions and ellipses around them represent their dispersion. The dotted curves show the discriminating surfaces found by the quadratic discriminant analysis. The left plot shows the observables before the Gaussian transformation and the right one after it.

## 4.6 Application to the selection of semi-leptonic events

The quadratic discriminant analysis was applied to select WW events decaying semi-leptonically. The selection was performed in each of the following channels: electron, muon, narrow-jet tau and one-prong tau. For each of these channels a discriminant variable was built. The discriminant variable was constructed using a number of observables, like visible energy, lepton momentum, etc. They are shown in table 4.4 and in figures 4.3, 4.5, 4.7, 4.8 and 4.10.

The discriminant was built using the events which passed the pre-selection described in section 4.4. For each of the observables used a temporary discriminant variable was built. The one giving the best performance was chosen as the first observable to be used in order to construct the final discriminant variable. After that a new discriminant was built using the first observable chosen and one of the remaining observables. This was done for each of the remaining observables, again the combination giving the best performance was chosen. This process only stopped when adding more observables to the discriminant no longer improved the discriminating power. The discriminant variable found by this procedure was the final discriminant variable used in this selection.

The distinction between signal and background is done by cuts applied on the discriminant variable in an iterative procedure. The events selected as signal after the cut is applied on the discriminant for the first time are used to train a second discriminant. The second

channel	$q\bar{q}e\nu_e$	$q\bar{q}\mu\nu_\mu$
variables	lepton energy lepton isolation angle missing momentum W mass $\sqrt{s'}$ $\cos \theta_{P_{miss}}$ Visible energy Total multiplicity Transverse energy	lepton momentum lepton isolation angle missing momentum W mass $\sqrt{s'}$ $\cos \theta_{P_{miss}}$ Visible energy Total multiplicity lepton - $P_{miss}$ angle
channel	$q\bar{q}\tau\nu_\tau$	$q\bar{q}\tau_{1p}\nu_\tau$
variables	charged multiplicity lepton isolation angle missing momentum W mass $\sqrt{s'}$ $\cos \theta_{P_{miss}}$ Visible energy Total multiplicity lepton - $P_{miss}$ angle angular spread aplanarity	lepton-jet angle lepton isolation angle  W mass $\sqrt{s'}$ $\cos \theta_{P_{miss}}$ Visible energy

Table 4.4: Observables used in the IDA selection to construct the discriminant variable for each channel. The  $q\bar{q}\tau\nu_\tau$  channel is the channel with a narrow-jet tau in the final state and the  $q\bar{q}\tau_{1p}\nu_\tau$  channel is the one with a one-prong tau in the final state. The W mass is the constrained fit mass (see section 5.1),  $\sqrt{s'}$  is the effective centre-of-mass energy (see reference [52]),  $\cos \theta_{P_{miss}}$  is the cosine of the polar angle of the missing momentum, the lepton-jet angle is the angle between the lepton and the nearest jet, the lepton -  $P_{miss}$  angle is the angle between the lepton and the missing momentum vector and the angular spread is the momentum-weighted angular spread of the narrow-jet tau defined in section 4.3.

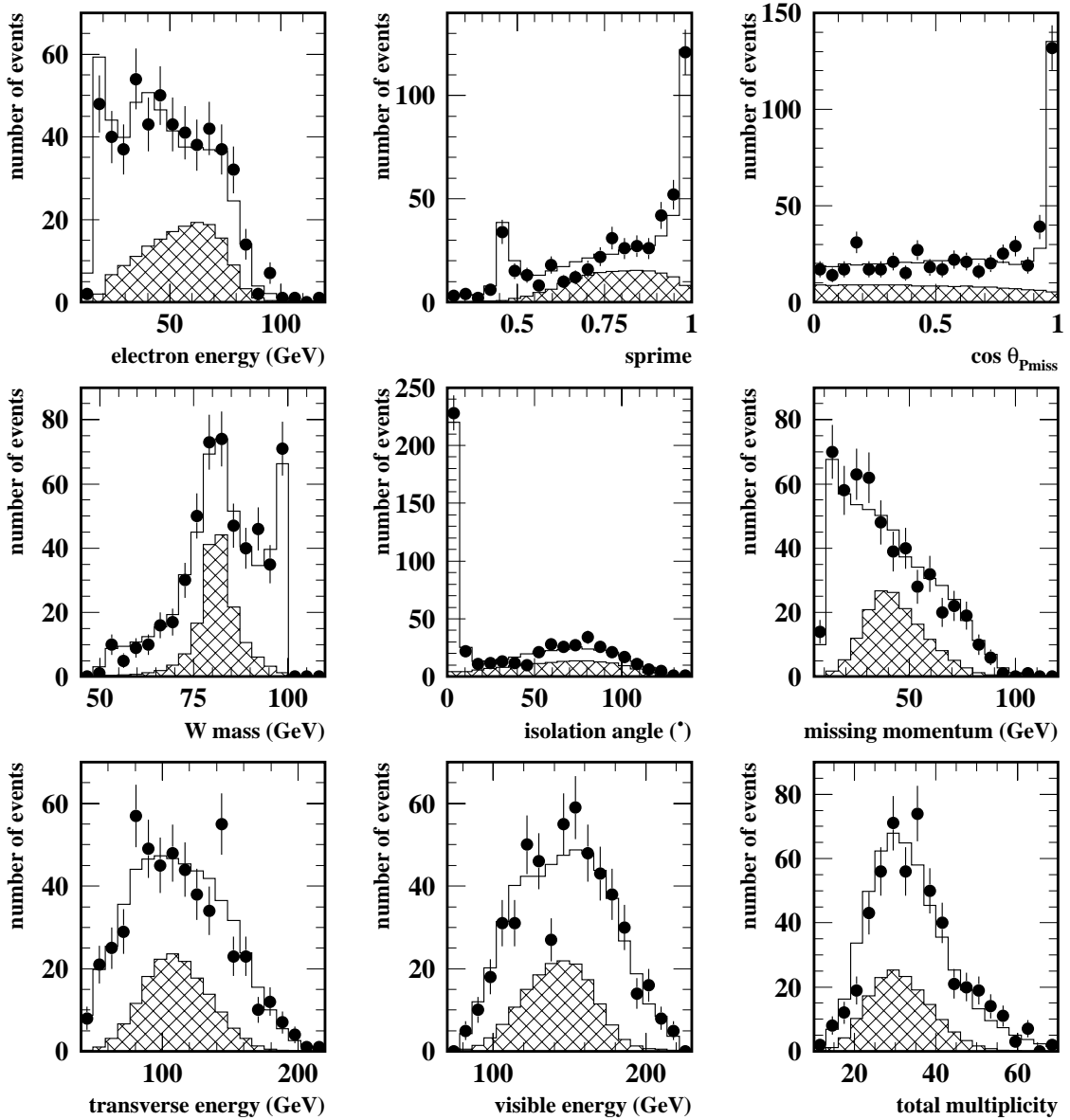


Figure 4.3: *Data-Monte Carlo agreement plots for the observables used to construct the discriminant variables for electrons at 200 GeV. The dots represent the data, the hatched histograms represent the signal events and the white histograms account for signal plus all background processes combined. These plots were made with events which passed the pre-selection. This legend is valid for all subsequent plots in this chapter.*

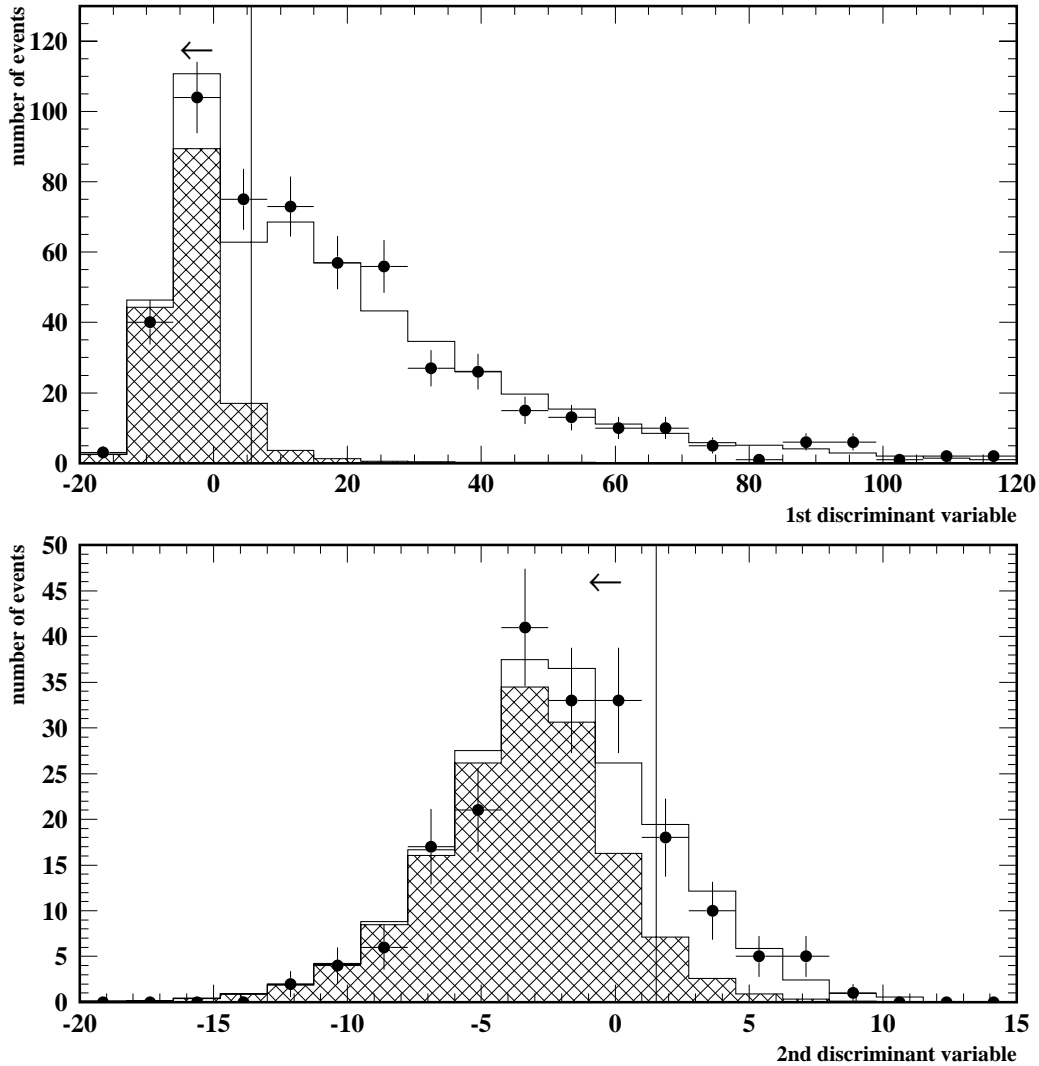


Figure 4.4: *First and second discriminant variables for electrons at 200 GeV. The vertical line represents the cut in the distribution in order to distinguish signal events from background ones. The arrow indicates that the events on that side of the line are selected events. The events which pass the cut on the first discriminant variable are used as input for the second discriminant variable. The events which pass the cut on the second discriminant variable are selected.*

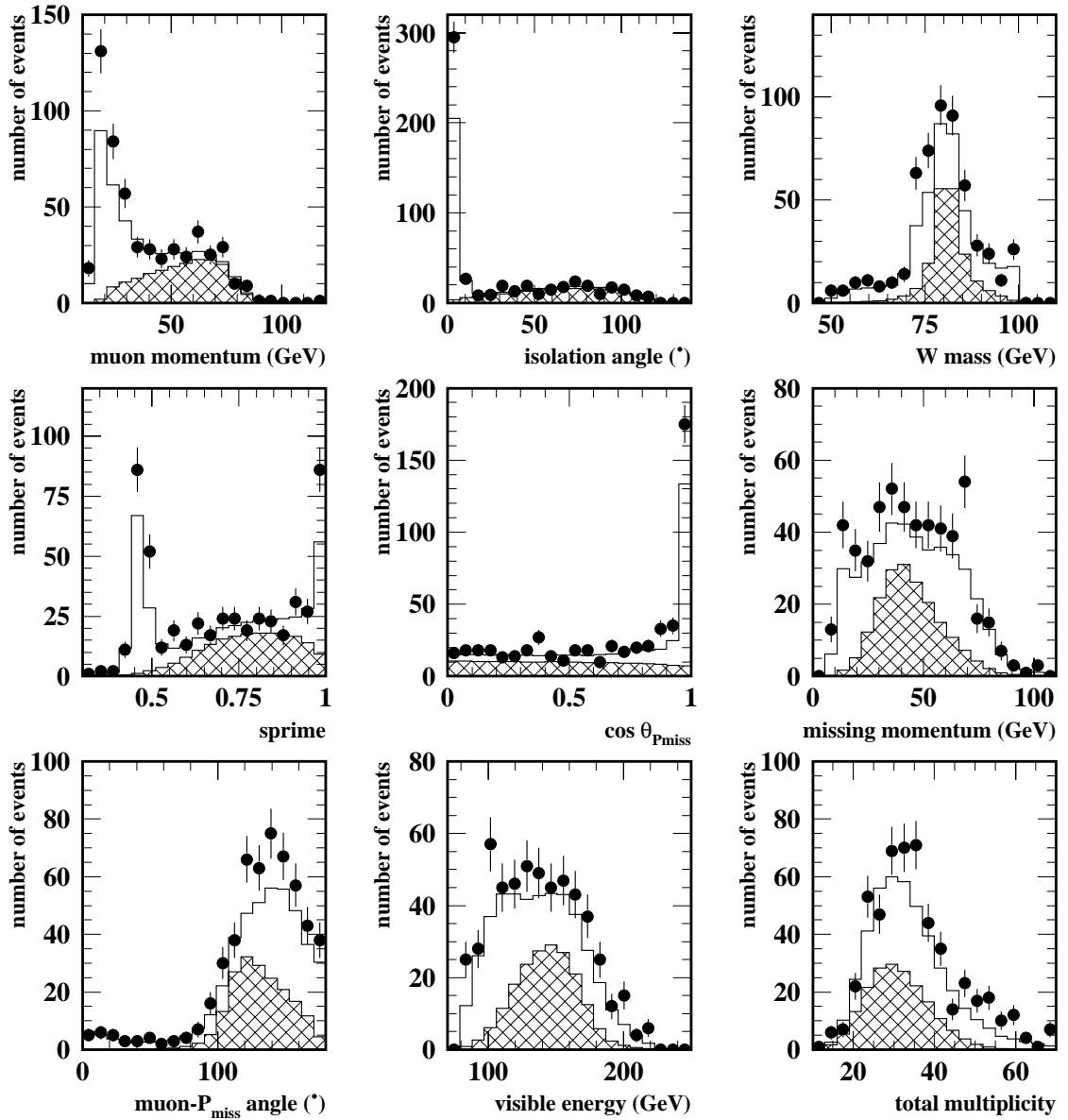


Figure 4.5: Observables used to construct the discriminant variables for muons at 200 GeV.

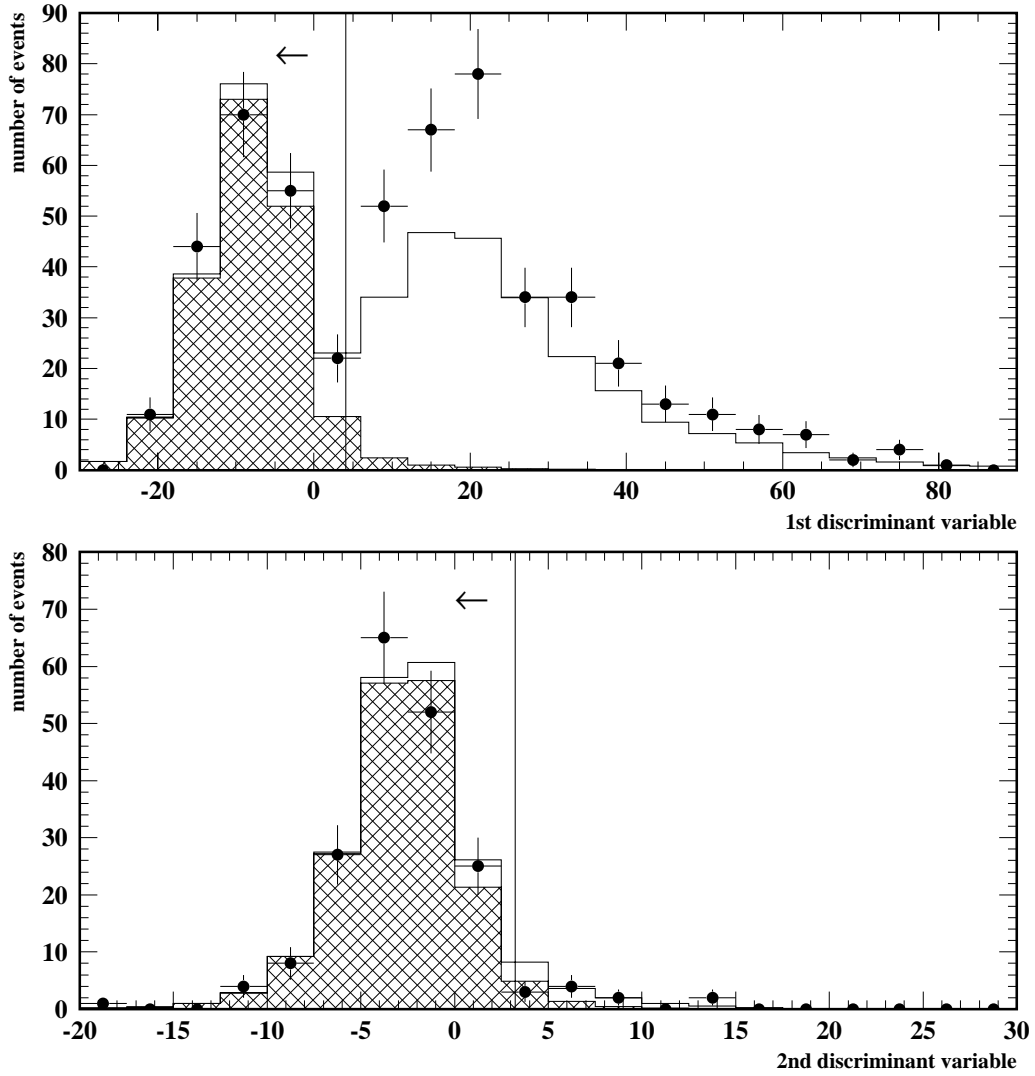


Figure 4.6: First and second discriminant variables for muons at 200 GeV.

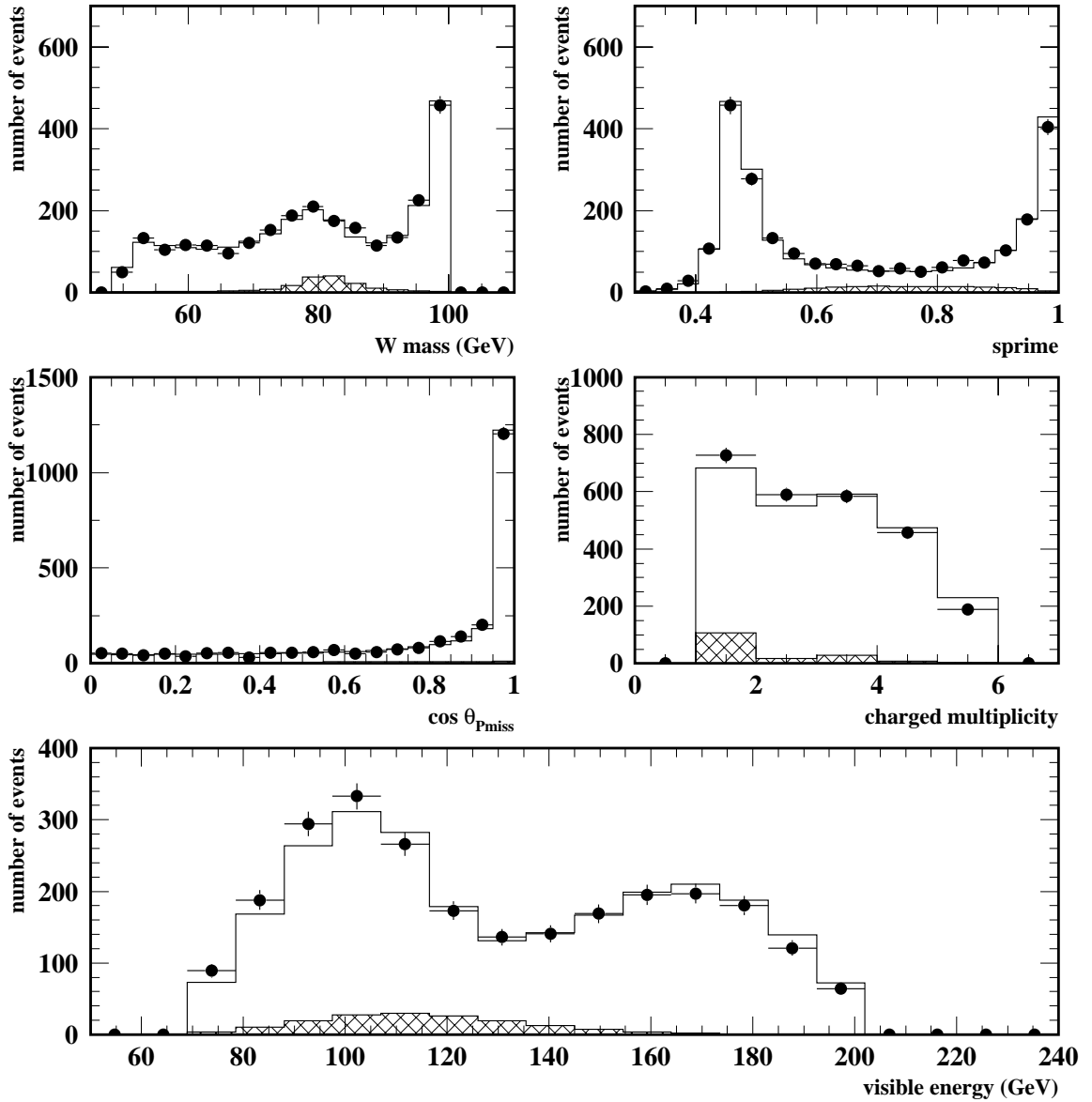


Figure 4.7: *Observables used to construct the discriminant variables for narrow-jet taus at 200 GeV.*

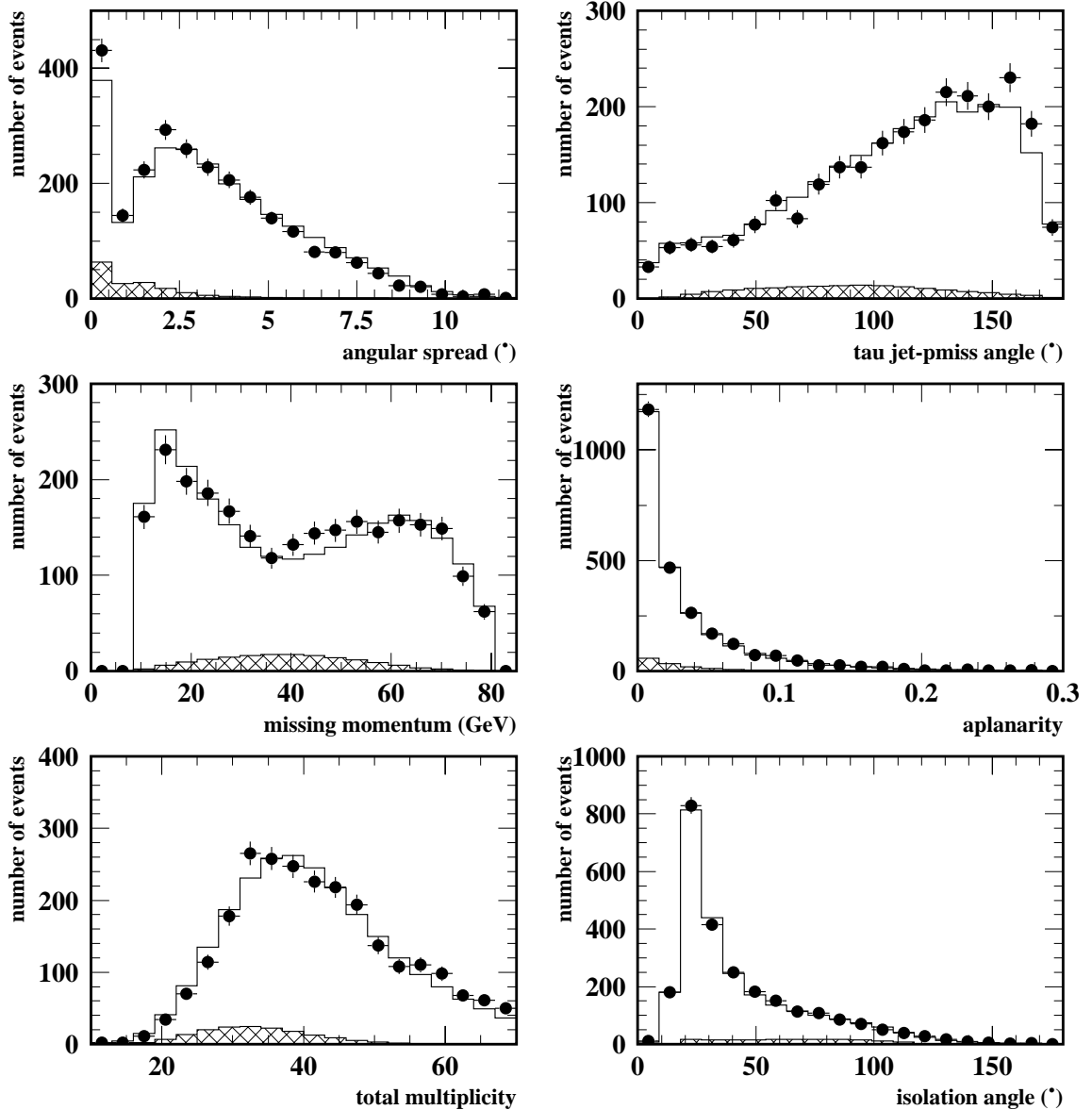


Figure 4.8: *Observables used to construct the discriminant variables for narrow-jet taus at 200 GeV.*

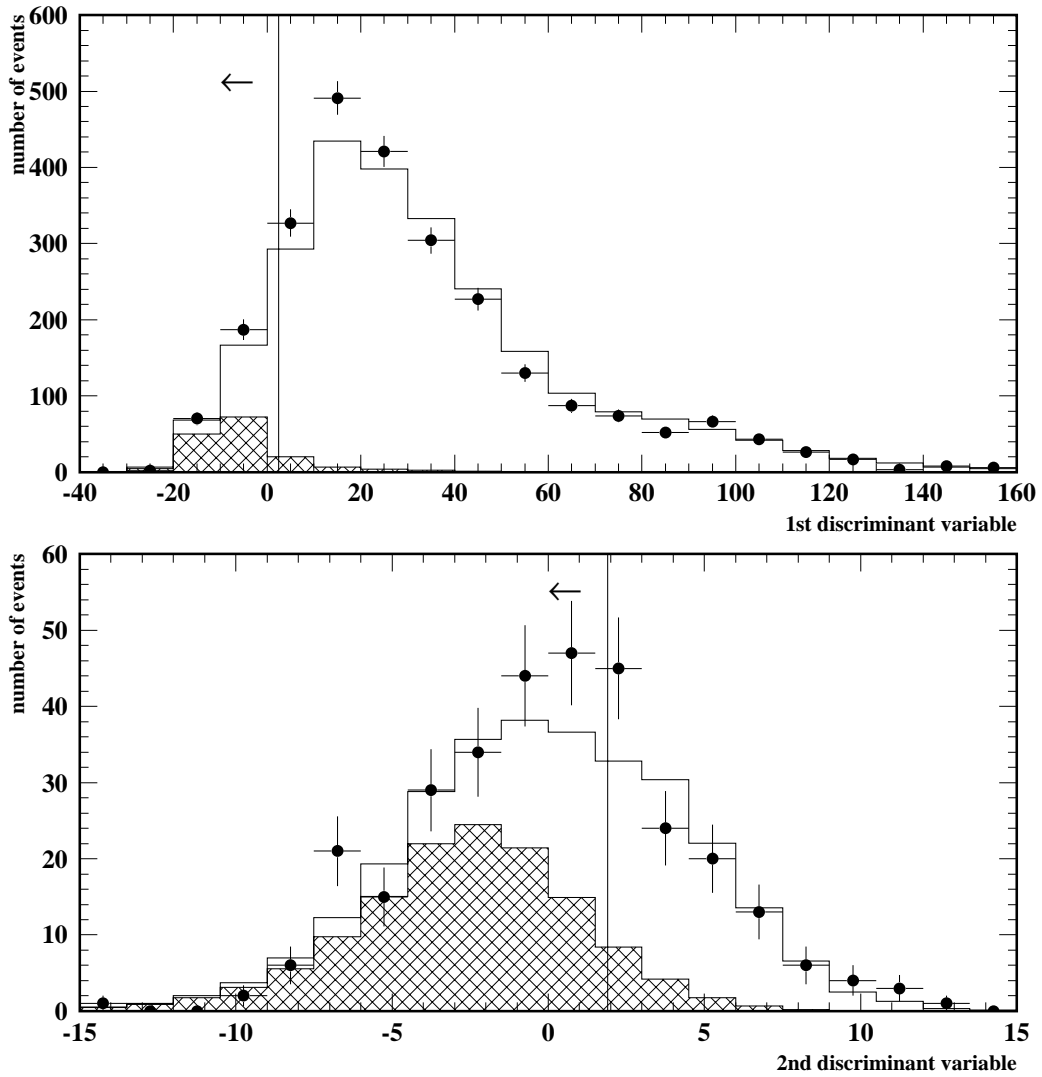


Figure 4.9: First and second discriminant variables for narrow-jet taus at 200 GeV.

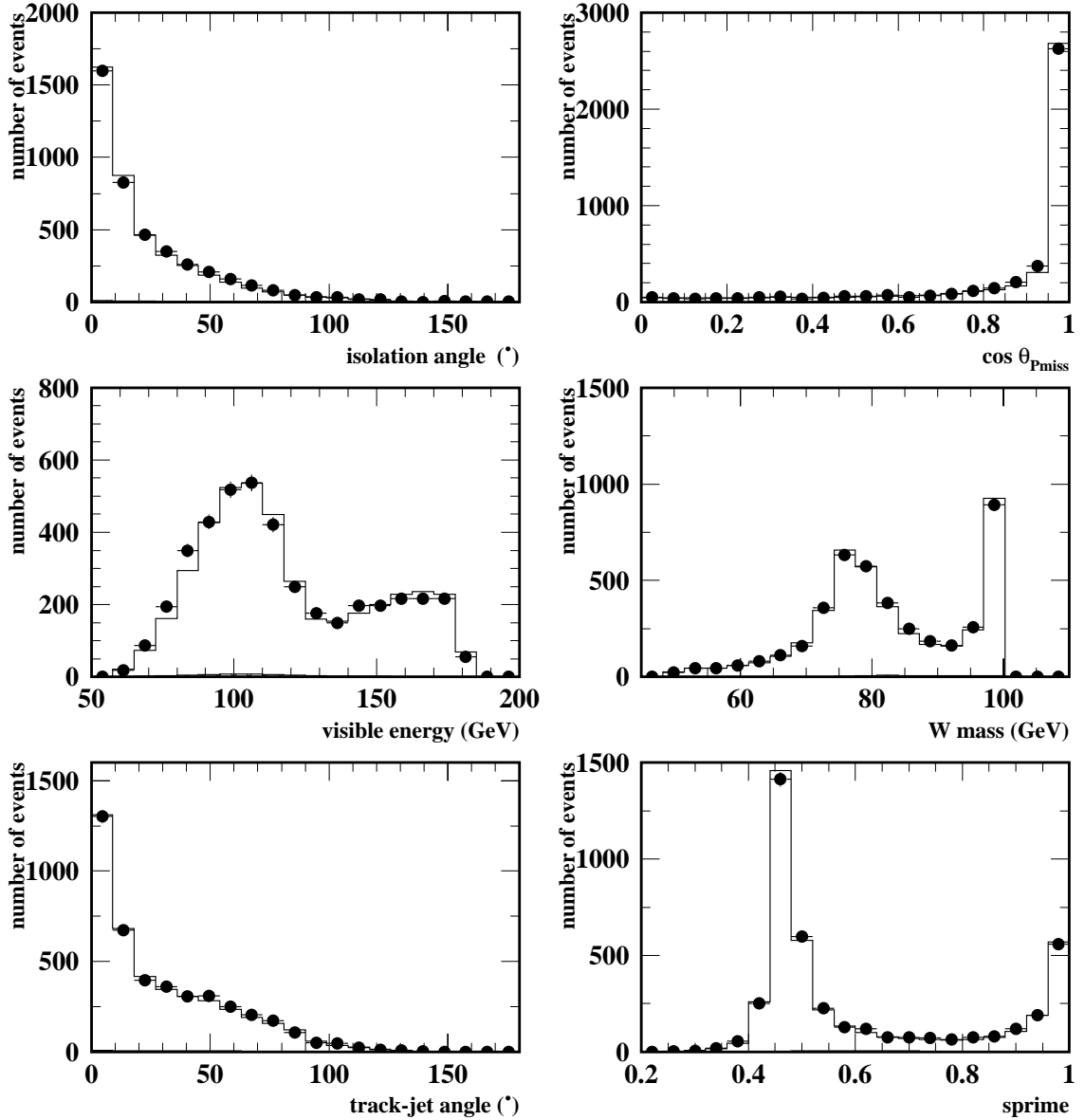


Figure 4.10: *Observables used to construct the discriminant variables for one-prong taus at 200 GeV.*

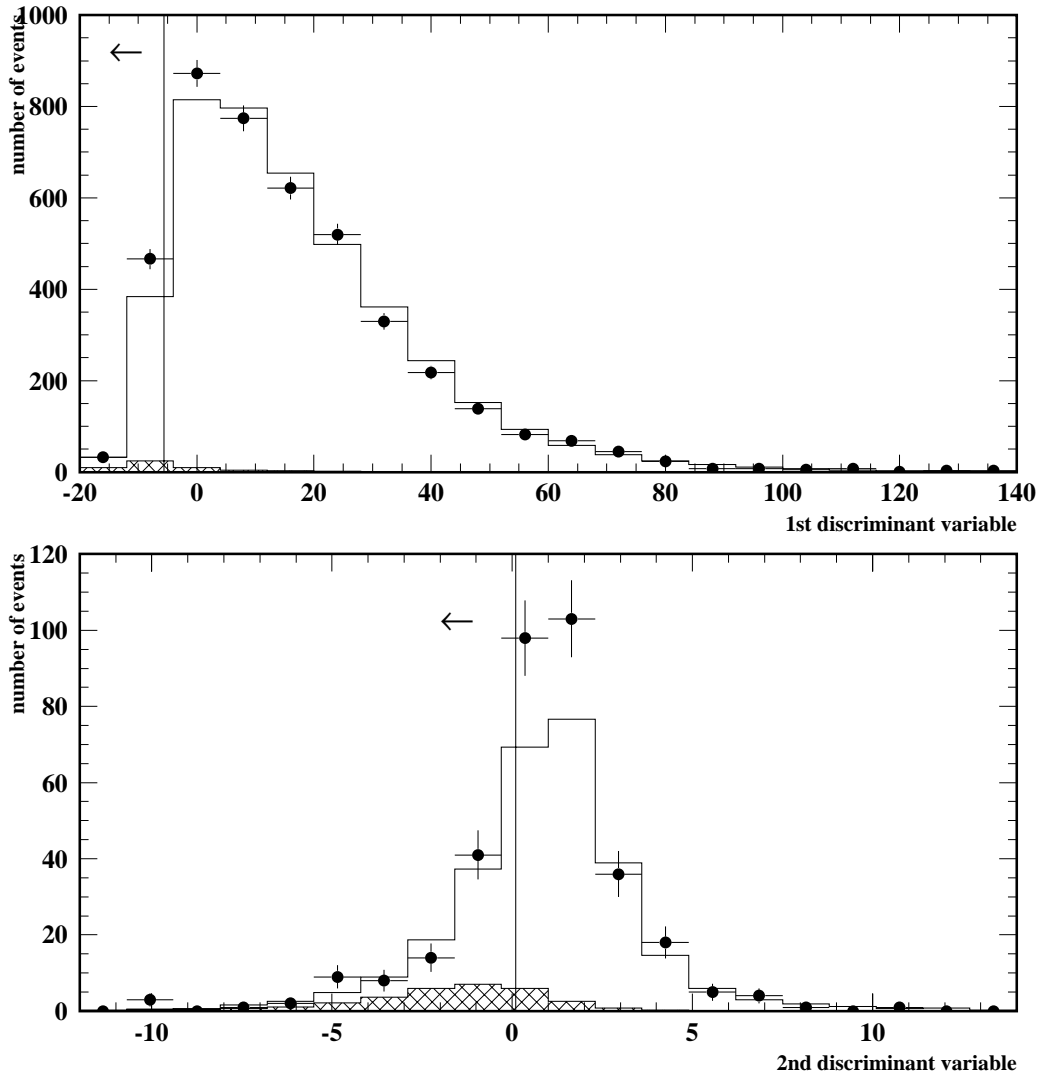


Figure 4.11: *First and second discriminant variables for one-prong taus at 200 GeV.*

discriminant is built in an identical way to the first, the only difference is the events used as input. A cut on the second discriminant is applied and if the event is in the signal region this is a selected event. The cut chosen is the one that maximises efficiency times purity. There are trainings available for three energy points, hence for each of these trainings different discriminant variables are built and an optimal cut for each of these variables is chosen. Figures 4.4, 4.6, 4.9 and 4.11 show the first and second discriminant variables for each of the four selection channels at 200 GeV centre-of-mass energy. The corresponding plots for 189 GeV and 206 GeV are shown in appendix A.

The selection was performed sequentially and in the following order: electron, muon, narrow-jet tau and one-prong tau. An event can be pre-selected several times, however it can only be selected once.

Due to the nature of this analysis (which is discussed in chapter 5) it could be interesting to use a looser selection instead of the one that maximises efficiency times purity. The selection performance for a higher cut on the discriminant variable has been studied. The results showed that the gains in the statistical errors were not significant and the purity became lower in all channels. Hence we kept the cut values that maximise efficiency times purity.

## 4.7 Selection performance

The selection efficiency for the different channels and the cross-section value of the different backgrounds retained by the selection can be seen in table 4.5. These efficiencies are calculated using all tree-level four-fermion charged current Feynman diagrams. If one would quote the efficiencies calculated using only the CC03 diagrams, the only channel which would be significantly affected would be the  $q\bar{q}e\nu_e$  one. In this channel the background due to single W production plays an important role.

The efficiency of the one-prong selection is very low. In addition one can see in figure 4.11 that many of the selected events in this channel are background events. However since the purity of each event is used as a weight in the mass extraction (for more details see chapter 5) these events can still be used in the analysis.

In figure 4.5 one can see that the data-Monte Carlo agreement in the  $q\bar{q}\mu\nu_\mu$  is not optimal for some of the variables shown. The underestimation of background events is the cause of the disagreement. The events underestimated in the simulation are the so-called punch-through-pions. These events sit mainly in the background region, as can be seen in figure 4.6, therefore no further investigation was performed.

The number of selected events, the number of expected background events and their corresponding purities in each channel can be seen in table 4.6. The purity shown in this table is calculated using the number of selected WW events, irrespective of the decay modes of the two W's involved. This means that a WW event that in fact decayed to a  $q\bar{q}e\nu_e$  final state but was selected as a  $q\bar{q}\tau\nu_\tau$  event is considered a signal event, as it is still sensitive to

M.C. truth	selection channel			
	$q\bar{q}e\nu_e$	$q\bar{q}\mu\nu_\mu$	$q\bar{q}\tau\nu_\tau$	$q\bar{q}\tau_{1p}\nu_\tau$
	efficiencies (%)			
$q\bar{q}e\nu_e$	$55.64 \pm 0.11$	$0.22 \pm 0.01$	$9.64 \pm 0.07$	$4.71 \pm 0.05$
$q\bar{q}\mu\nu_\mu$	$0.10 \pm 0.01$	$85.18 \pm 0.09$	$4.24 \pm 0.05$	$1.64 \pm 0.03$
$q\bar{q}\tau\nu_\tau$	$3.13 \pm 0.04$	$2.53 \pm 0.04$	$58.22 \pm 0.13$	$11.17 \pm 0.08$
$q\bar{q}q\bar{q}$	$0.027 \pm 0.003$	$0.027 \pm 0.002$	$1.17 \pm 0.01$	$0.40 \pm 0.01$
$l\nu_l l\nu_l$	$0.08 \pm 0.03$	$0.08 \pm 0.02$	$0.08 \pm 0.08$	$0.07 \pm 0.04$
	backgrounds (fb)			
$q\bar{q}(\gamma)$	$82.6 \pm 4.2$	$18.7 \pm 2.1$	$207.0 \pm 6.7$	$486.4 \pm 10.3$
<i>other</i> – 4f	$75.5 \pm 2.1$	$26.5 \pm 0.7$	$126.0 \pm 3.4$	$105.8 \pm 2.9$
$\gamma\gamma$	$28.0 \pm 28.0$	0	0	$27.7 \pm 16.0$

Table 4.5: Selection efficiencies at 200 GeV. The table is arranged as columns of tagging channel and rows of event truth category. The tau channel is split in two for the selection channel columns, but is shown as one for the truth row. The ‘other-4f’ row accounts for the background from 4-fermion neutral current processes.

the W mass.

	selection channel			
	$q\bar{q}e\nu_e$	$q\bar{q}\mu\nu_\mu$	$q\bar{q}\tau\nu_\tau$	$q\bar{q}\tau_{1p}\nu_\tau$
183 GeV				
number of selected events	93	118	129	93
number of expected bg events	6.4	3.1	21.1	59.1
purity	92.5%	97.4%	82.8%	32.2%
189 GeV				
number of selected events	269	339	352	204
number of expected bg events	25.2	11.2	59.1	124.8
purity	91.0%	97.2%	84.0%	36.6%
192 GeV				
number of selected events	42	53	58	54
number of expected bg events	3.7	1.1	10.1	25.4
purity	91.8%	98.2%	84.1%	38.7%
196 GeV				
number of selected events	152	166	170	124
number of expected bg events	11.6	3.5	28.1	59.5
purity	91.7%	98.2%	85.5%	43.4%
200 GeV				
number of selected events	163	185	213	107
number of expected bg events	13.6	4.3	28.3	49.6
purity	91.8%	97.7%	85.3%	46.1%
202 GeV				
number of selected events	93	88	87	39
number of expected bg events	6.4	1.9	13.1	20.2
purity	91.4%	98.2%	87.1%	49.9%
206 GeV				
number of selected events	363	434	469	232
number of expected bg events	41.2	11.7	76.5	117.0
purity	89.8%	97.9%	86.2%	48.2%

Table 4.6: Number of selected events, number of expected background events their corresponding purities per channel at all centre-of-mass energies.



# Chapter 5

## W mass analysis

The aim of this chapter is to describe all the tools needed in this analysis in order to extract the W mass with the exception of the event selection which was already discussed in the previous chapter. The first section describes the constrained fit which is a procedure used to improve the measurement of the invariant mass. The implementation described here is the standard implementation used in the DELPHI collaboration. In section 5.2 the jet clustering algorithms used in this analysis are briefly discussed. After that comes a comprehensive description of the Ideogram method [53] which was the method used to measure the W mass. In section 5.7 the impact of the event selection in the W mass measurement is discussed. At last section 5.8 presents the results for the W mass for all centre-of-mass energies analysed.

### 5.1 The constrained fit

In an  $e^+e^-$  collider the centre-of-mass energy is known to a great precision. One can use the fact that energy and momentum are conserved to constrain the event. The four constraints are shown below:

$$\sum_{i=1}^n E_i = \sqrt{s} \quad (5.1)$$

$$\sum_{i=1}^n \vec{p}_i = 0 \quad (5.2)$$

where  $E_i$  and  $\vec{p}_i$  are the energy and momentum of the reconstructed objects in the event,  $i$  is the number of reconstructed objects and  $\sqrt{s}$  is the centre-of-mass energy. The objects are, for example in the case of a WW semi-leptonic event, the jets, the lepton and the neutrino. The constrained fit is a powerful tool which can be used in the measurement of the W mass. The measured energy and momentum of the objects and the errors on these measurements are supplied as input to the fit. The output of the fit is then the fitted energy and momenta of the objects. The constrained fit discussed above is referred hereafter as a 4C fit because

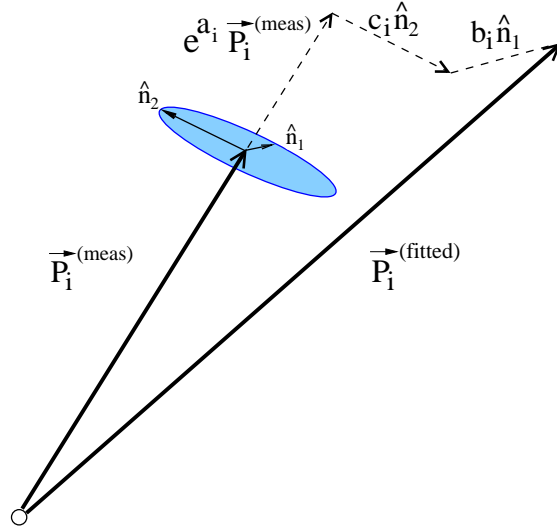


Figure 5.1: Schematic view of the momentum parameterisation used in the constrained fit.  $\vec{p}_i^{meas}$  is the measured momentum which is given as input to the constrained fit and  $\vec{p}_i^{fitted}$  is the fitted momentum which is an output of the constrained fit. For more details see text.

it has four constraints. The package used to perform the constrained fit is PUFITC+ [53]. Lagrange multipliers are used to satisfy the imposed constraints while minimising a  $\chi^2$ . The  $\chi^2$  is defined as:

$$\chi^2 = \sum_{i=1}^{n_y} \frac{(y_i^{fit} - y_i^{meas})^2}{\sigma_{y_i}^2} \quad (5.3)$$

where  $y_i$  are the fitting parameters and  $n_y$  is the number of parameters. The estimated error,  $\sigma_{y_i}$ , has to be given by the user.

### 5.1.1 Jet and lepton parameterisation

Each element, jet or lepton, is described by three parameters. Muons are defined by their measured momentum and track angles. The errors on these parameters come directly from the track fit. Electrons are described by their measured energy and their detected angular position in the electromagnetic calorimeters. The energy uncertainties are obtained from parameterisations of the electromagnetic calorimeter responses. The angular uncertainties were determined from the track fit.

The uncertainty on the measured momenta of the tau and the jets is known to be large. Hence a fit parameterisation is needed to ensure that energies can not become negative. A schematic drawing of the momentum parameterisation can be seen in figure 5.1. The fitted

momentum is parameterised as follows:

$$\vec{p}_i^{fit} = e^{a_i} \vec{p}_i^{meas} + b_i \hat{n}_1 + c_i \hat{n}_2 \quad (5.4)$$

where  $\vec{p}_i^{meas}$  is the measured momentum.  $\hat{n}_1$  and  $\hat{n}_2$  are the unit vectors in the orthogonal plane to the measured momentum direction. The  $e^{a_i}$  factor in equation (5.4) is present to make the error distribution look more Gaussian. This is done because the fitting method assumes that the errors are gaussianly distributed. The measured energies  $E_i^{meas}$  are rescaled with the same factor. The  $\chi^2$  in this case is given by:

$$\chi_i^2 = \frac{(a_i - a_0)^2}{\sigma_{a_i}^2} + \frac{b_i^2}{\sigma_{b_i}^2} + \frac{c_i^2}{\sigma_{c_i}^2} \quad (5.5)$$

where  $a_i$ ,  $b_i$  and  $c_i$  are the parameters to be fitted. The parameter  $a_0$  represents the expected energy loss (around 15% for jets). When the track polar angles are small the resolution on them deteriorates, and due to the acceptance of the DELPHI detector, particles escape detection. Due to that resolution on the jet energy and the jet energy loss parameter are polar angle dependent. In addition the undetected low polar angle tracks introduce a bias on the jet direction shifting them away from the beam axis. The expected errors  $\sigma_{a_i}$ ,  $\sigma_{b_i}$  and  $\sigma_{c_i}$  as well as the parameter  $a_0$  were determined using 2-jet events at the Z peak from calibration runs [53]. The resulting parameterisation for jets is:

$$\begin{aligned} a_0 &= 0.15 + 0.40 \cdot \cos^4 \theta_i \\ \sigma_{a_i} &= 0.15 + 0.40 \cdot \cos^4 \theta_i \\ \sigma_{b_i} &= \sigma_{c_i} = (1.0 + 0.6 \cdot \cos^4 \theta_i) \cdot 1.62 \end{aligned} \quad (5.6)$$

where  $\theta_i$  is the polar angle of the jet. In the case of taus a first fit is performed with large errors:

$$\begin{aligned} a_0 &= 1.0 \\ \sigma_{a_i} &= 10. \\ \sigma_{b_i} &= \sigma_{c_i} = 0.5. \end{aligned} \quad (5.7)$$

This fit determines the missing mass which depends on the number of neutrinos in the final state. The missing mass is then used to estimate the transverse errors on the tau for a second fit [53], which are:

$$\sigma_{b_i}^2 = \sigma_{c_i}^2 = \frac{E_m(E_{fit} - E_m)m_\tau^2 - E_{fit}(E_{fit} - E_m)m_m^2 - 1/2(m_\tau^2 - m_m^2)^2}{2(GeV)^2 p_m^2} \quad (5.8)$$

where  $m_\tau$  is the tau mass (1.784 GeV),  $m_m$  is the measured missing mass and the other subscripts  $m$  and  $fit$  stand for measured and fitted respectively. As can be seen from the formula a large deviation between either the fitted energy and the measured energy, or the measured mass and the actual tau mass, will lead to a large error estimate, as one would expect.

### 5.1.2 Jet breadth

A more accurate description of the jet transverse errors has to take into account their dependence on the jet breadth. The jet breadth was calculated by projecting the momenta of all particles in the jet on to the plane perpendicular to the jet axis. From those projections a two dimensional momentum tensor  $\mathcal{T}_{\beta\gamma}$  was created:

$$\mathcal{T}_{\beta\gamma} = \sum_i p_{\beta}^i p_{\gamma}^i, \quad (5.9)$$

where  $p_{\beta}^i$  and  $p_{\gamma}^i$  are the two components of the projection of the momentum of particle  $i$  in the transverse plane. The normalised eigenvectors of the tensor,  $\vec{p}_i^b$  and  $\vec{p}_i^c$ , represent the directions where the jet was broadest and slimmest. Their corresponding eigenvalues are  $B_b$  and  $B_c$ . A first fit using the parameterisation given by equation (5.6) was performed. The jet energies obtained from this fit were compared to the measured energies. The difference between the two gave an estimate of the missing energy in the jet, this variable is referred to as  $E_{i,miss}$ . This quantity was used for an improved parameterisation of the jet transverse errors in all subsequent fits. The improved jet transverse errors became:

$$\begin{aligned} a_0 &= 0.15 + 0.40 \cdot \cos^4\theta_i \\ \sigma_{a_i} &= 0.15 + 0.40 \cdot \cos^4\theta_i \\ \sigma_{b_i}^2 &= 0.2 + 1.0(\text{GeV})^{-2} \cdot B_b \frac{\sqrt{1(\text{GeV}) \cdot E_i^m + E_{i,miss}^2}}{E_i^m} \\ \sigma_{c_i}^2 &= 0.2 + 1.0(\text{GeV})^{-2} \cdot B_c \frac{\sqrt{1(\text{GeV}) \cdot E_i^m + E_{i,miss}^2}}{E_i^m}. \end{aligned} \quad (5.10)$$

## 5.2 Jet clustering

The clustering of particles into jets is performed by a jet clustering algorithm. There are several jet clustering algorithms available and most of them function in a similar way. An essential element in the clustering is the measurement of the distance between two particles. This distance is used to decide which particles should be combined. A cut value for this distance is also important, this value, referred to hereafter as  $y_{cut}$ , determines the maximum distance for which two particles can be combined. The clustering process is an iterative procedure. It begins by calculating the distance between particle  $i$  and particle  $j$  for every pair of particles. Then based on these distances it starts to combine particles. This procedure is repeated until the distance between any pair of particles is larger than  $y_{cut}$ . These clusters of particles are called jets.

The jet clustering algorithm used in this analysis to cluster the hadronic part of the event is DURHAM [54]. In the DURHAM algorithm the distance between particle  $i$  and particle

$j$  is defined as

$$y_{ij} = \frac{2(1 - \cos \theta_{ij}) \min(E_i^2, E_j^2)}{E_{vis}^2}, \quad (5.11)$$

where  $\theta_{ij}$  is the angle between the two particles,  $E_i$  and  $E_j$  are their energies and  $E_{vis}$  is the total visible energy in the event. After an isolated lepton or a low multiplicity jet (in the case of the tau) was found the remaining particles in the event were forced into 2 and 3-jet configurations. The 3-jet events are the events with hard gluon radiation. Both configurations were saved. The event was treated to be a 3-jet event if the distance  $y_{ij}$  for going from a 3-jet configuration to a 2-jet configuration was larger than the cut value of 0.001.

LUCCLUS [55] was used to identify the narrow taus, as described in section 4.3. The distance between two particles in this case is defined as:

$$d_{ij} = \frac{|\vec{p}_i \times \vec{p}_j|}{|\vec{p}_i + \vec{p}_j|} \quad (5.12)$$

The clustering ends when the distance  $d_{ij}$  between any two clusters is larger than the cutoff  $d_{join}$ , which in the case of this analysis was 6.5 GeV.

## 5.3 The Ideogram method

The aim of the Ideogram method is to extract maximal statistical information from every event which is used to determine the W mass. This is achieved by constructing an event-by-event likelihood curve. The advantage of using this method is that one can take into account all information that is considered to be significant in the likelihood curve. The following sections will describe all the steps needed in order to build the event-by-event likelihood.

The ideogram method is based on Bayesian inference. The Bayes theorem can be written as:

$$p(m_W | event, I) = \frac{p(event | m_W, I) \cdot p(m_W | I)}{p(event | I)} \quad (5.13)$$

where  $m_W$  is the quantity one wants to measure,  $I$  represents all underlying assumptions and  $event$  stands for the observed data. The left side of equation (5.13) shows the probability of measuring  $m_W$  in the data set  $event$  given the assumptions  $I$ . The right side of equation (5.13) says that this probability can be written as the product of the likelihood function  $p(event | m_W, I)$  and the ‘Bayesian prior’  $p(m_W | I)$ , divided by a normalisation factor  $p(event | I)$ . In other words it represents the product of the probability to observe the event  $event$  given a certain  $m_W$  and  $I$  and the assumed probability to obtain a certain  $m_W$  given the assumptions  $I$ , normalised by the probability to obtain the event given the assumptions  $I$ . If one considers the prior to be flat and does not take into account the normalisation, like it is done in this thesis, the theorem is reduced to the maximum likelihood method:

$$p(m_W | event, I) \propto p(event | m_W, I) \quad (5.14)$$

### 5.3.1 First steps for building the event likelihood

This section describes how the event-by-event likelihood curve was built for this analysis. The first step is to separate the likelihood curve into two independent parts. One is related to the physics process and the other to the kinematics in the event. As it is known, the total likelihood curve will be to a good approximation the product of the two independent likelihood curves. The physics part takes into account the W bosons production process which is described by electroweak theory. This likelihood curve can be approximately written as

$$p(\vec{m}' | m_W, I) \approx BW(m_1 | m_W, \Gamma_W) \cdot BW(m_2 | m_W, \Gamma_W) \cdot \frac{1}{s} \sqrt{(s - m_1^2 - m_2^2)^2 - 4m_1^2 m_2^2} \quad (5.15)$$

which is the product of two running width Breit-Wigner functions (equation (2.15)) and a phase space function, where  $\vec{m}'$  represents the invariant masses  $m_1$  and  $m_2$  of the two objects in the event forming W boson candidates. The kinematic part of the likelihood is in fact the experimental resolution function and is independent of  $m_W$ . This part will contain all the approximations related to the fact that the measurement has a limited precision. This likelihood curve can be written as:

$$p(event | \vec{m}', I) = p_{6C}^{fit}(jets + lepton | \vec{m}', \sqrt{s}) \quad (5.16)$$

and will be referred to hereafter as ideogram. This equation represents the likelihood to observe the jets and the lepton seen in the event for a given pair of invariant masses when performing a 6-constrained fit. A 6C fit consists of the four constraints for energy and momentum conservation and two additional ones for the fact that the masses of the two W bosons are fixed to the values  $\vec{m}' = (m_1, m_2)$ . The steps needed to build an ideogram will be discussed in detail in section 5.3.3. The total likelihood curve will be

$$p(event | m_W, I) \approx \int \int p(event | \vec{m}', I) \cdot p(\vec{m}' | m_W, I) d\vec{m}' \quad (5.17)$$

which is the convolution of equations (5.15) and (5.16). This integral is evaluated in two dimensions and accounts for the fact that the two W bosons are not necessarily produced with the same invariant mass.

### 5.3.2 Event purity calculation

An event-by-event purity is also included in the ideogram analysis. The purpose here is to take into account the fact that one does not know for sure if the event in question is a true WW event or a background one. If one includes the event purity in the likelihood curve the latter will become:

$$p(event | m_W, I) \approx \int \int p(event | \vec{m}', I) \cdot \left[ \mathcal{P}_{event} \cdot S(\vec{m}' | m_W, I) + (1 - \mathcal{P}_{event}) \cdot B(\vec{m}' | I) \right] d\vec{m}' \quad (5.18)$$

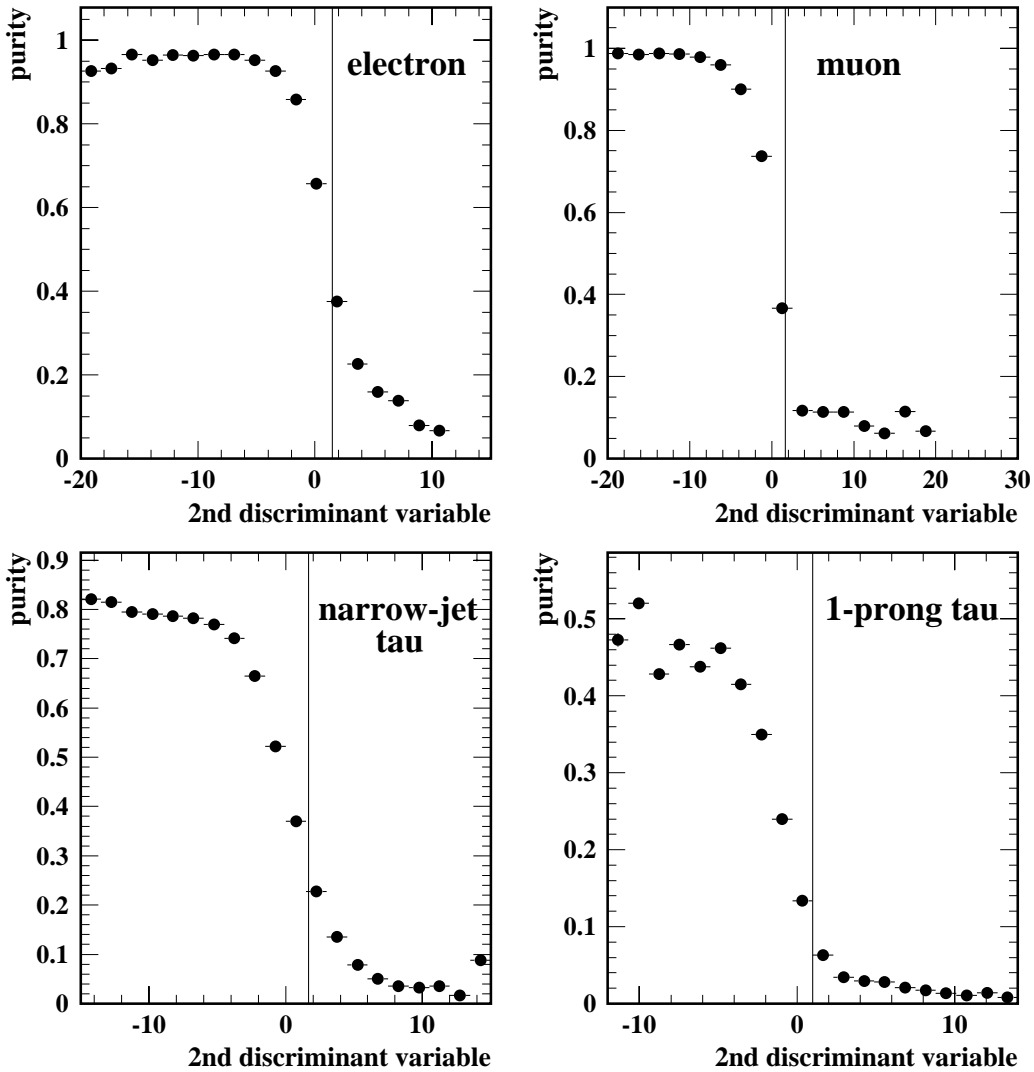


Figure 5.2: Event purity as a function of the second discriminant variable for each channel,  $q\bar{q}e\nu_e$ ,  $q\bar{q}\mu\nu_\mu$ ,  $q\bar{q}\tau\nu_\tau$  and  $q\bar{q}\tau_{1p}\nu_\tau$ , at 189 GeV. The vertical lines represent the cut on the discriminant variable in order to select events. Events to the left of the line are selected. The purity plots for 200 GeV and 206 GeV are shown in appendix A

where  $\mathcal{P}_{event}$  is the event purity and  $S(\vec{m}'|m_W, I)$  represents equation (5.15).  $B(\vec{m}'|I)$  represents the background shape which does not depend on  $m_W$  and is chosen to be flat in the 2-dimensional  $\vec{m}'$  - space.

In order to obtain an estimate of the event-by-event purity the second discriminant variable, described in chapter 4, is used. The second discriminant variable is by construction a good variable to be used in the purity estimation, because it is built in order to discriminate between signal and background. For simulated events the distribution of the second discriminant variable is stored for both signal and background. The purity of an event as a function of the second discriminant variable  $D$  is given by

$$\mathcal{P}_{event} = \frac{s(D)}{s(D) + b(D)} \quad (5.19)$$

where  $s(D)$  is the number of selected signal events and  $b(D)$  the number of selected background events. When the analysis is run for data events one checks the value of the second discriminant variable for the event in question and retrieves the corresponding purity for that particular value of the discriminant variable. This is done for each of the four selection channels  $q\bar{q}e\nu_e$ ,  $q\bar{q}\mu\nu_\mu$ ,  $q\bar{q}\tau\nu_\tau$  and  $q\bar{q}\tau_{1p}\nu_\tau$ . Figure 5.2 shows the purity as function of the second discriminant variable for each of these channels. The purity was estimated at three different centre-of-mass energies, 189 GeV, 200 GeV and 206 GeV. For the other centre-of-mass energies the purity estimate closest in energy was used.

### 5.3.3 Building a 2-dimensional ideogram

The ideogram for one event is given by equation (5.16). It can be interpreted as the goodness-of-fit probability given by the 6-constrained kinematic fit for a given pair of invariant masses  $\vec{m}'$  at a centre-of-mass energy  $\sqrt{s}$ .

In order to build the ideogram 6C fits were performed on a rectangular grid in the  $m_1 + m_2$  and  $m_1 - m_2$  direction on the plane  $m_1, m_2$ . The fits were performed only in predefined points of the grid, the values in between the points were obtained by interpolation. The algorithm used is as follows [53]. The starting point  $(m_1, m_2)$  is the one found by a 4C fit (equations 5.1 and 5.2), which means both masses are free. After that 6C fits are performed on the grid. Every next fitting point was arbitrarily chosen from neighbouring points of the point with the lowest  $\chi_{6C}^2$  which had already been fitted and still had at least one neighbour which was not yet fitted. The starting value for the new fit was the value found by the fit of the neighbouring point which had the lowest  $\chi^2$ . The resulting  $\Delta\chi_{6C}^2(m_1, m_2)$  distribution is interpreted as a probability density function

$$P_{hypothesis}^{q\bar{q}l\nu_i}(m_1, m_2) dm_1 dm_2 \propto \exp\left(-\frac{1}{2}\Delta\chi_{6C}^2(m_1, m_2)\right) dm_1 dm_2 \quad (5.20)$$

where the  $\chi_{6C}^2(m_1, m_2)$  was rescaled with a factor  $\text{NDF}/\chi_{4C}^2(m_1, m_2)$  in similar procedure to the one used by the Particle Data Group. The distribution is then normalised on the

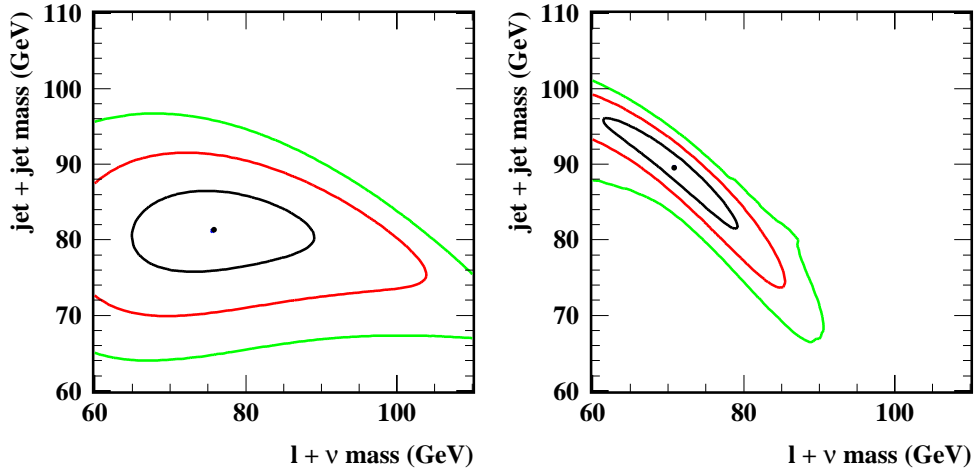


Figure 5.3: Examples of ideograms for two simulated WW events at 189 GeV. The first three sigma contours of the probability density are shown and the dot represents the point with the lowest  $\chi^2$ . The difference in shape between the ideograms is related to different configurations of the lepton and jets in the event. One can see in both cases the fact that the ideogram is broader in the (lepton + neutrino) direction, this is obviously due to the presence of the neutrino.

kinematical region so that

$$\int_{m_{min}}^{m_{max}} \int_{m_{min}}^{m_{max}} P_{hypothesis}^{q\bar{q}l\nu_i}(m_1, m_2) dm_1 dm_2 = 1 \quad (5.21)$$

where  $m_{min} = 60$  GeV and  $m_{max} = 110$  GeV. Figure 5.3 shows two ideograms for WW simulated events at 189 GeV.

### 5.3.4 Ambiguity in the tau channel

In a  $q\bar{q}\tau\nu_\tau$  event the amount of missing energy depends on the number of neutrinos in the final state which can add up to three depending on the tau decay products. One of the many challenges in this channel is to distinguish between  $q\bar{q}\tau\nu_\tau$  events and  $q\bar{q}e\nu_e$  or  $q\bar{q}\mu\nu_\mu$  events. Since the tau lepton can decay into an electron or muon (and two neutrinos) it becomes hard to identify whether the electron (or muon) is a direct decay product of the W or not. In the ideogram method both hypotheses are taken into account. In order to take this cross-talk into account the event is fitted in two different ways:

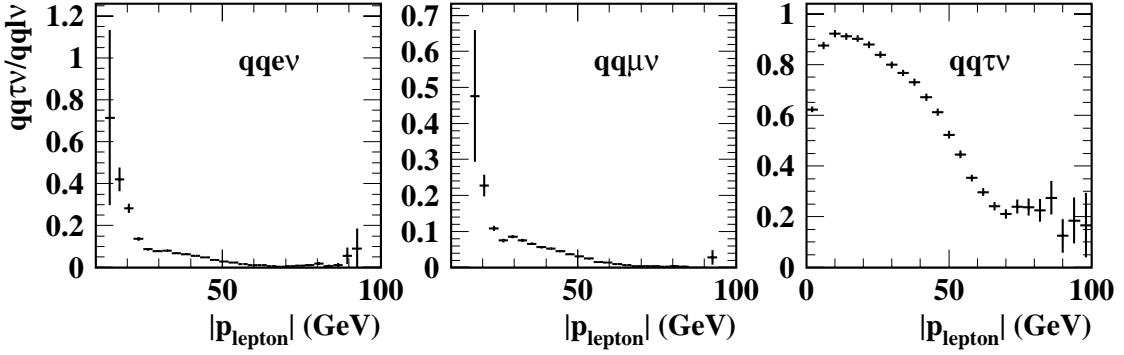


Figure 5.4: The plots show the fraction of  $q\bar{q}\tau\nu_\tau$  over  $q\bar{q}l\nu_l$  as a function of the absolute lepton momentum for each selection channel. The selection channels are indicated on the top right of the plots. These plots were made using simulated signal events at 189 GeV.

- The lepton was a tau. The constrained fit treats the lepton as a tau. In this case the number of unknowns increases due to the two additional neutrinos present.
- The lepton was an electron or a muon. In the  $q\bar{q}e\nu_e$  and  $q\bar{q}\mu\nu_\mu$  channels the constrained fit treats the lepton as an electron for the first and as a muon for the latter. In the  $q\bar{q}\tau\nu_\tau$  channel the alleged tau candidate is defined as an electron in the fit.

For each event a relative probability for each of the two hypothesis is estimated. This relative probability is estimated as a function of the lepton momentum and is obtained using Monte Carlo, see figure 5.4. An ideogram is built for each of the two hypothesis. By using the relative probability as a weight for the tau and non-tau ideograms, the combined ideogram probability becomes

$$p(event|\vec{m}', I)d\vec{m}' \propto P_{tot}^{q\bar{q}l\nu_l}(\vec{m}')d\vec{m}' \quad (5.22)$$

where

$$P_{tot}^{q\bar{q}l\nu_l}(\vec{m}')d\vec{m}' = \left( w_{\tau/non-\tau}^{\tau/non-\tau} P_{\tau}^{q\bar{q}l\nu_l}(\vec{m}') + w_{non-\tau}^{\tau/non-\tau} P_{non-\tau}^{q\bar{q}l\nu_l}(\vec{m}') \right) d\vec{m}'. \quad (5.23)$$

In the equation above  $w_{hypothesis}^{\tau/non-\tau}$  is the relative probability for the current hypothesis which in this case can be  $\tau$  or  $non-\tau$ . Therefore two ideograms are built per event.

## 5.4 Extracting the W mass

The previous section described every step of how the likelihood curve for one event was built. The total likelihood for one event can therefore be written as

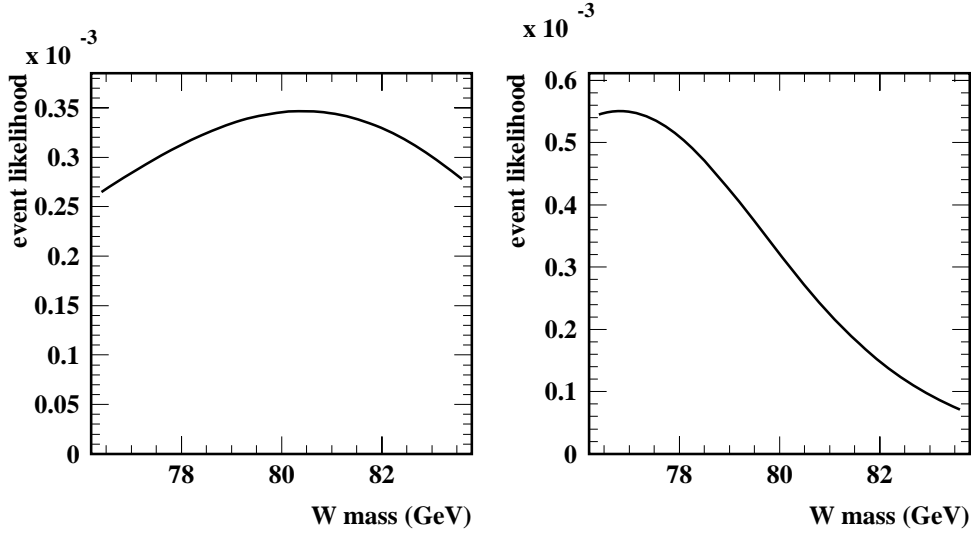


Figure 5.5: Event likelihood curves corresponding to the two ideograms shown in figures 5.3 at 189 GeV. The left likelihood curve is broader than the right one which is consequence of the shape of the ideograms.

$$p(event|m_W, I) = \mathcal{L}(m_W) \approx \int_{m_{min}}^{m_{max}} \int_{m_{min}}^{m_{max}} P_{tot}^{qq\bar{q}l\nu_l}(\vec{m}') \cdot \left[ \mathcal{P}_{event} \cdot S(\vec{m}'|m_W, I) + (1 - \mathcal{P}_{event}) \cdot B(\vec{m}'|I) \right] d\vec{m}' \quad (5.24)$$

This likelihood takes into account the physics process of the WW production, in the form of the two Breit-Wigners, and the experimental resolution function which is what we call an ideogram. The likelihood also includes an event-by-event purity and it takes into account the probability whether the lepton in the event was a decay product of the  $\tau$  or not. Figure 5.5 shows two examples of event likelihood curves. By taking the natural logarithm the event likelihood curves become:

$$L_{event}(m_W) = -2 \ln(\mathcal{L}(m_W)). \quad (5.25)$$

Therefore the overall likelihood curve will be the sum of the negative log likelihood curves

$$L_{overall}(m_W) = \sum_1^{n_{event}} L_{event}(m_W). \quad (5.26)$$

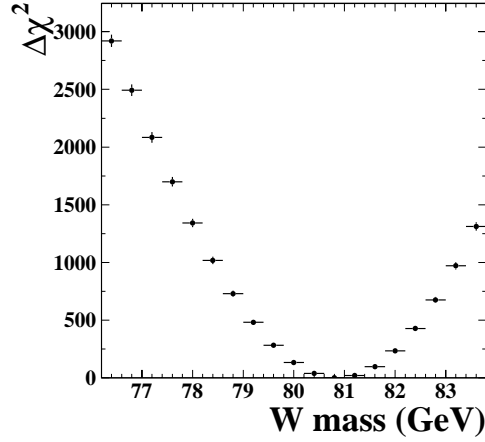


Figure 5.6: Overall likelihood curve for Monte Carlo signal events at 206 GeV. The sample used to make this plot contained around 3,300 events.

Figure 5.6 shows an overall likelihood curve. The W mass is determined by fitting a parabola through the three lowest points of the overall likelihood curve. The error on this mass is calculated using the second derivative at the minimum

$$\sigma_{m_W}^{fitted} = \sqrt{\frac{2}{\alpha}} \quad (5.27)$$

where  $\alpha$  is

$$\alpha = \left. \frac{\partial^2 L_{overall}(m_W)}{\partial m_W^2} \right|_{m_W = m_W^{fitted}} \quad (5.28)$$

The fitted value for  $m_W$  will be referred hereafter as  $m_W^{measured}$ .

## 5.5 Calibration curves

There are several possible sources of bias in the analysis just described here. For example, the analytical likelihood curves do not take into account Initial State Radiation, the jet errors parameterisation used is just an approximation, the event selection could also introduce a bias. Therefore a procedure to correct for biases independently of what the source is was applied. The procedure consists of checking how the bias in the measured W mass changes as a function of the generated W mass. In order to do that Monte Carlo is used. A total of 3 Monte Carlo samples with different values for the generated W mass were used and they were obtained by Monte Carlo re-weighting<sup>1</sup>. The reference sample had a generated

---

<sup>1</sup>Monte Carlo events are usually all generated with weight one. Monte Carlo re-weighting is a technique that by re-weighting every generated event with a certain weight one can change certain properties of the original

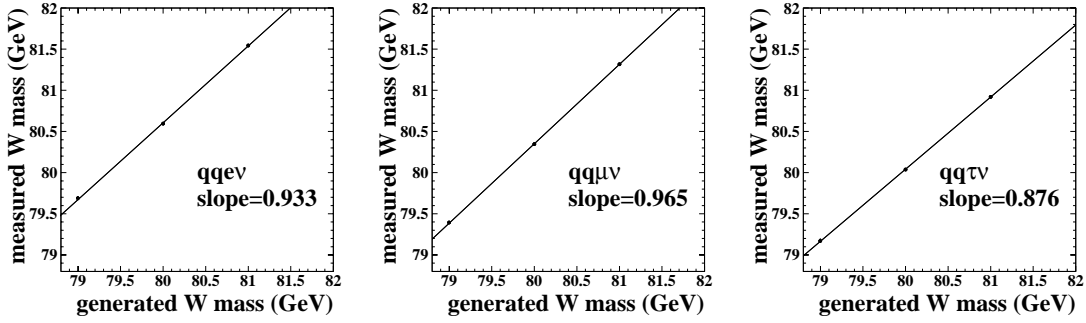


Figure 5.7: Calibration curves for the  $q\bar{q}e\nu_e$ ,  $q\bar{q}\mu\nu_\mu$  and  $q\bar{q}\tau\nu_\tau$  channels respectively at 196 GeV. The plot shows the measured  $W$  mass as a function of the generated  $W$  mass. A linear function was fitted to the plot, the slope found by the fit is indicated on the bottom right. The error bars on the three points are plotted, but are too small to be seen.

channel	Slope						
	183	189	192	196	200	202	206
$q\bar{q}e\nu_e$	0.937	0.909	0.902	0.933	0.906	0.953	0.927
$q\bar{q}\mu\nu_\mu$	0.953	0.976	0.946	0.965	0.963	1.003	0.980
$q\bar{q}\tau\nu_\tau$	0.778	0.796	0.840	0.876	0.879	0.921	0.893

Table 5.1: Slopes of the calibration curves for each of the 3 semi-leptonic decay channels with the nominal centre-of-mass energies (in GeV) of each data sample indicated. The statistical error on the slope is typically of the order of  $1.0 \times 10^{-3}$ .

$W$  mass of 80.4 GeV, the generated masses of the re-weighted samples were 79.0 GeV, 80.0 GeV and 81.0 GeV. The measurement of the  $W$  mass is performed for each of these 3 samples. Figure 5.7 shows the dependence of the measured  $W$  mass as a function of the generated  $W$  mass. The slope of this curve is a measurement of that dependence. Table 5.1 shows the slope found by fitting a linear function to the  $m_W^{\text{measured}}$  versus  $m_W^{\text{generated}}$  plot for each channel for all centre-of-mass energies analysed. A slope equal to one means the bias in the analysis does not depend on the  $W$  mass. The further away the slope is from one the bigger the bias. The bias in the measured  $W$  mass at a given point is defined as

$$\text{bias} = m_W^{\text{measured}} - m_W^{\text{generated}} \quad (5.29)$$

Monte Carlo sample, like for example the  $W$  mass. A study showing the consistency between the results found by using Monte Carlo re-weighting or independent Monte Carlo samples can be found in [53].

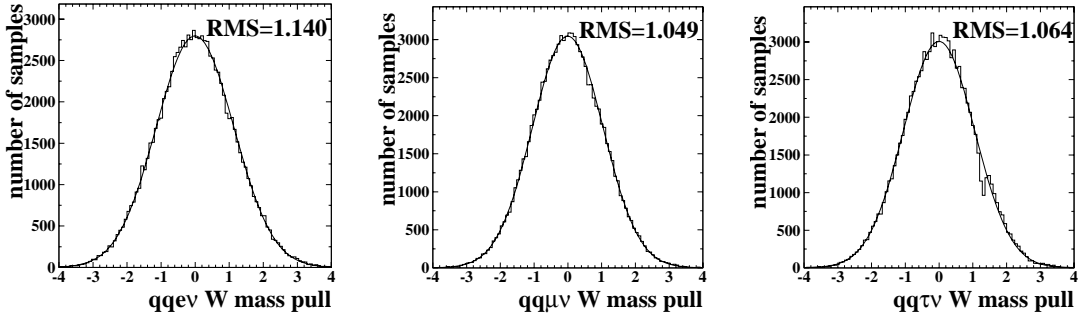


Figure 5.8:  $W$  mass pull distributions obtained at 206 GeV for the  $q\bar{q}e\nu_e$ ,  $q\bar{q}\mu\nu_\mu$  and  $q\bar{q}\tau\nu_\tau$  channels respectively. The RMS values of the distributions are indicated in the plot and were obtained by fitting a Gaussian to the distribution.

where  $m_W^{\text{generated}}$  is the generated  $W$  mass. The bias corrected  $W$  mass is then given by

$$m_W^{\text{corrected}} = m_W^{\text{generated}} + \frac{(m_W^{\text{measured}} - (m_W^{\text{generated}} + \text{bias}))}{\text{slope}} \quad (5.30)$$

where  $m_W^{\text{measured}}$  is the mass that comes out of finding the minimum of the log likelihood curve and  $m_W^{\text{generated}}$  is the  $W$  mass used to generate the  $WW$  events which in this case is 80.4 GeV. The bias is calculated using equation (5.29) for  $m_W^{\text{generated}} = 80.4$  GeV. The error on the  $W$  mass was also scaled with  $1/\text{slope}$ .

## 5.6 Pull distribution

Certain assumptions and approximations were made when building the event likelihood curves. One of them, for example was the simplified jet resolution parametrisation, which assumes the jet errors are gaussianly distributed. If these are not good approximations this can lead to an underestimated error on the  $W$  mass.

The pull distributions are a useful tool to correct for that. The pull distribution of the  $W$  mass is defined as the distribution of the quantity:

$$\text{pull} = \frac{m_W^{\text{measured}} - \langle m_W^{\text{measured}} \rangle}{\sigma^{\text{estimated}}} \quad (5.31)$$

where  $m_W^{\text{measured}}$  is the measured  $W$  mass for a sample of Monte Carlo events,  $\langle m_W^{\text{measured}} \rangle$  is the mean of the  $m_W^{\text{measured}}$  distribution and  $\sigma^{\text{estimated}}$  is the estimated error on the measurement of the  $W$  mass of that sample. In order to obtain the pull distribution many Monte Carlo samples with the same integrated luminosity as for the data were built. The samples

were built using signal and background events which were randomly chosen from the complete Monte Carlo sample according to a Poisson distribution. Due to limited Monte Carlo statistics events had to be used more than once. A total of 100,000 samples were built. The W mass and the error on it were measured in each of them. Figure 5.8 shows the pull distributions for all 3 channels at 206 GeV centre-of-mass energy and table 5.2 shows the RMS values of these distributions for all centre-of-mass energies. The RMS of these distributions is used as a scale factor to correct the mostly underestimated errors in the W mass measurement.

channel	W mass pull						
	183	189	192	196	200	202	206
$q\bar{q}e\nu_e$	1.055	1.069	1.100	1.097	1.108	1.137	1.140
$q\bar{q}\mu\nu_\mu$	1.016	1.015	0.973	1.020	1.032	1.043	1.049
$q\bar{q}\tau\nu_\tau$	0.979	0.965	0.984	1.017	1.041	1.022	1.064

Table 5.2: RMS of the W mass pull distributions for each of the 3 semi-leptonic decay channels with the nominal centre-of-mass energies (in GeV) of each data sample indicated. The error on the RMS is typically of the order of  $1.0 \times 10^{-3}$ .

## 5.7 Impact of the selection on the W mass measurement

The selection method was discussed in chapter 4. The impact of the chosen method on the W mass measurement should still be addressed. The Iterative Discriminant Analysis (IDA) method uses the event-by-event reconstructed W mass from a 5C-fit as one of the observables to construct the discriminant variable. A 5C-fit consists of four constraints for energy and momentum conservation and an equal mass constraint, *i.e.*, the fitted masses of the two W bosons have to be identical. In principle one could argue that this is simply incorrect, because it introduces a bias in the measurement. However this is exactly one of the advantages of using the ideogram method, the calibration curves correct for this as they correct for any other possible biases in the analysis. For completeness the bias caused by the selection method was extensively studied. In an attempt to mimic a selection which was not W mass dependent, the W mass used in the IDA selection was fixed to a certain value. This is not equivalent to not using the W mass to construct the discriminant variable, but it is a good approximation of what would happen in that case. When doing that it was observed that indeed the bias in the analysis decreases, on the other hand there was no significant gain nor loss in the expected error. The bias decreased the most in the tau channel. This was to be expected since in this channel the W mass was the variable with most discriminating power.

## 5.8 Results

The W mass results are presented in table 5.3. The results are given by channel and for each centre-of-mass energy. The table shows the W mass measured in that channel and its statistical uncertainty. The difference in the size of the statistical error from sample to sample is obviously a direct consequence of the luminosity of the samples. The systematic uncertainties are discussed in chapter 6. The consistency of the results will be discussed in chapter 7. As an illustration figure 5.9 shows the W mass spectrum for each of the three channels at two different centre-of-mass energies, 189 GeV, 200 GeV and for all energies combined.

Year	Energy (GeV)	Channel	W mass (GeV)
1997	183	$q\bar{q}e\nu_e$	$81.171 \pm 0.421$
		$q\bar{q}\mu\nu_\mu$	$80.723 \pm 0.314$
		$q\bar{q}\tau\nu_\tau$	$80.372 \pm 0.517$
1998	189	$q\bar{q}e\nu_e$	$79.864 \pm 0.296$
		$q\bar{q}\mu\nu_\mu$	$80.292 \pm 0.181$
		$q\bar{q}\tau\nu_\tau$	$80.265 \pm 0.299$
1999	192	$q\bar{q}e\nu_e$	$80.825 \pm 0.838$
		$q\bar{q}\mu\nu_\mu$	$80.282 \pm 0.464$
		$q\bar{q}\tau\nu_\tau$	$81.441 \pm 0.645$
	196	$q\bar{q}e\nu_e$	$80.076 \pm 0.422$
		$q\bar{q}\mu\nu_\mu$	$80.221 \pm 0.264$
		$q\bar{q}\tau\nu_\tau$	$80.713 \pm 0.388$
	200	$q\bar{q}e\nu_e$	$80.355 \pm 0.367$
		$q\bar{q}\mu\nu_\mu$	$80.266 \pm 0.270$
		$q\bar{q}\tau\nu_\tau$	$81.366 \pm 0.443$
202	$q\bar{q}e\nu_e$	$80.703 \pm 0.534$	
	$q\bar{q}\mu\nu_\mu$	$80.153 \pm 0.352$	
	$q\bar{q}\tau\nu_\tau$	$80.531 \pm 0.547$	
2000	206	$q\bar{q}e\nu_e$	$80.815 \pm 0.301$
		$q\bar{q}\mu\nu_\mu$	$80.542 \pm 0.193$
		$q\bar{q}\tau\nu_\tau$	$80.658 \pm 0.271$

Table 5.3: Measured W mass (in GeV) for each of the 3 semi-leptonic decay channels with the nominal centre-of-mass energies (in GeV) of each data sample indicated.

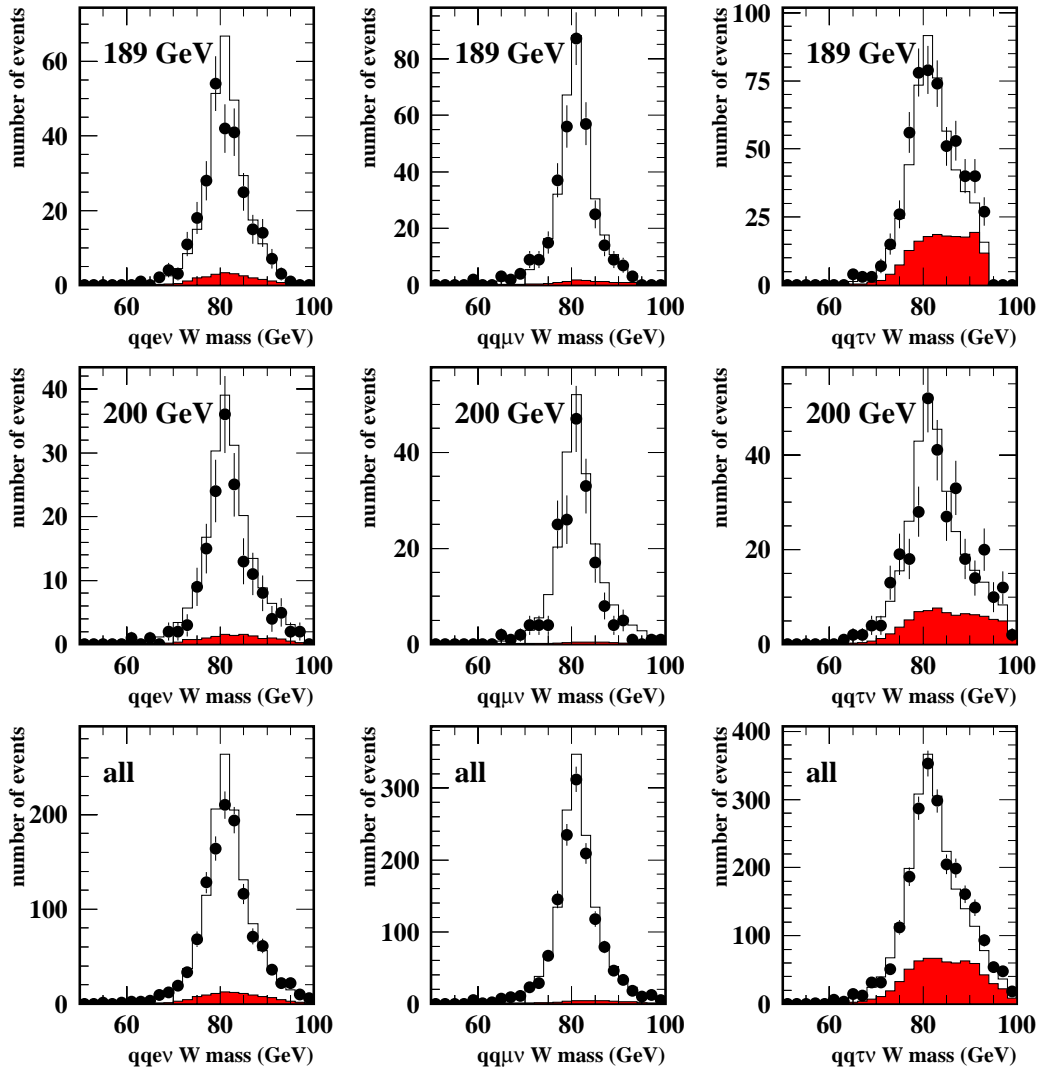


Figure 5.9:  $W$  mass spectrum at different centre-of-mass energies. The centre-of-mass energy is indicated on the top left of each plot. The plots in the bottom row are for all centre-of-mass energies combined. The mass shown is the 5C-fit mass and it is plotted separately for each of the three channels. The dots represent the data, the white histogram represents signal plus all background processes combined and the grey histograms the background only. The generated  $W$  mass used in the Monte Carlo was 80.40 GeV



# Chapter 6

## Systematic Uncertainties

This chapter discusses the possible sources of systematic uncertainties in the measurement of the W mass. Furthermore it describes how these uncertainties were estimated. The assumption made throughout this thesis that the Monte Carlo describes the data was thoroughly checked and is discussed here. The majority of the effects discussed in this chapter were studied using Z peak data taken during calibration runs and their corresponding Monte Carlo samples. The main reason for this is the limited amount of data available at LEP-2.

The outline of this chapter is as follows. Section 6.1 describes the uncertainties due to detector effects. Section 6.2 describes the Mixed Lorentz Boosted Zs method which was used to assess the systematic uncertainty due to fragmentation. Section 6.3 and 6.4 describe the theoretical uncertainties and section 6.5 describes briefly the work done by the LEP energy working group in order to determine the uncertainty on the beam energy.

### 6.1 Detector effects

The discrepancies between data and Monte Carlo due to detector effects can introduce a bias in the W mass measurement. Thus these discrepancies have been extensively studied by the W physics group in DELPHI. These studies were performed using Z peak data taken during calibration runs. The procedure for many of them was the same, data and Monte Carlo at the Z peak were compared. If discrepancies were found the Monte Carlo (or in some cases the data) was corrected in order to describe the data (or the Monte Carlo). These corrections were determined separately for the different years of data taking. They were then implemented in the WWANA package and were therefore available to the whole W physics group. These corrections are referred to hereafter as standard WWANA corrections. The systematic errors due to these corrections were also determined separately for the four years of data taking analysed here. For data at different centre-of-mass energies collected in the same year the systematic errors were assumed to be identical, given the fact that the detector did not change within one year. In addition the corrections used are also determined per year.

The systematic errors due to detector effects were all determined as follows. The standard WWANA corrections for the effect in question were applied to data or Monte Carlo at the Z peak depending on the nature of the corrections. Data and Monte Carlo were then compared. The remaining discrepancies between data and Monte Carlo were determined. The corrections to account for these remaining discrepancies were then applied to the Monte Carlo used for the W mass analysis<sup>1</sup>. In case the remaining discrepancies were not statistically significant the error on them was used. The W mass was determined using the data combined with this modified Monte Carlo. This result was then compared to the result obtained using the standard Monte Carlo (presented in table 5.3). The difference between the two masses is quoted as the systematic uncertainty due to the effect in question.

### 6.1.1 Muon inverse momentum scale

Detector alignment and reconstruction distortions can be a source of systematic uncertainties for the momentum scale of muons. An opposite bias on the measured track curvature for positive and negative muons can arise from this. A charge dependent momentum shift is applied to the muons in the data to correct for this difference. The study to determine the magnitude of the shift was performed with Z data taken during calibration runs. The shifts were determined by comparing the mean of the inverse momentum distribution for data and Monte Carlo in 6 bins of the track polar angle. These corrections were determined for each year of data taking and are standard corrections for WWANA. For a complete description of this work see reference [56].

Effect	$m_W$ systematic errors in the muon channel (MeV)			
	183	189	200	206
$1/p$ scale	19	20	25	28
$\mu^+ \mu^- 1/p$ difference	0	0	0	1
$1/p$ resolution	5	3	1	5

Table 6.1: Systematic uncertainties for the  $q\bar{q}\mu\nu_\mu$  channel. The results are all in MeV and are presented at four centre-of-mass energies.

The work done for this thesis consisted of applying the above corrections to Z data and checking for remaining discrepancies between data and Monte Carlo. A simple selection in order to select  $Z \rightarrow \mu^+\mu^-$  collected during the calibration run of 1999 was applied. The events were required to have two charged particles and that both these particles were identified as a muon. In addition the following cuts were applied:

<sup>1</sup>As described in chapter 5 the Monte Carlo is used in the W mass analysis to calibrate the data.

- The two leading tracks should have a momentum above 5 GeV;
- The polar angle of the muon tracks should be above  $10^\circ$ ;
- The maximum acollinearity was  $10^\circ$ ;
- $\sqrt{P_1^2 + P_2^2} > 40$  GeV, where  $P_1$  and  $P_2$  are the momenta of the two muons.

Once the events were selected. The reconstructed momentum of all selected di-muon events were scaled by the ratio of the centre-of-mass energy for the event to the centre-of-mass energy of generated events in the Monte Carlo. Having done that inverse momentum distributions for data and for Monte Carlo were then fitted with a double Gaussian. The relative difference between the fitted mean for Monte Carlo and data was determined. This difference amounted to  $-0.29\%$  as can be seen in figure 6.1. A scale factor of that magnitude was applied to the 4-momenta of muons in the Monte Carlo used for the W mass analysis in order to determine the impact of these corrections in the W mass. The systematic uncertainties for 183 GeV, 189 GeV, 200 GeV and 206 GeV are presented in table 6.1.

### 6.1.2 Difference between $\mu^+$ and $\mu^-$ inverse momentum

Besides the fact that discrepancies in the all-muons momentum scale can be a source of bias in the W mass measurement, the difference between the  $\mu^+$  and the  $\mu^-$  inverse momenta distributions could also lead to a bias. In order to study this effect shifts of opposite sign were applied to the momentum of the  $\mu^+$  and of the  $\mu^-$  in the Monte Carlo used for the W mass analysis. This shift was determined using the same muon pairs selected by the selection described in 6.1.1. The same corrections mentioned above were applied to the data. In the Z Monte Carlo the means of the inverse momentum distributions for  $\mu^+$  and  $\mu^-$  were in agreement with each other, however this was not observed for the data. The goal was to apply a shift to the Monte Carlo events which would make it describe the behaviour seen in the data. The shift applied was half of the difference between the means of the  $\mu^+$  and  $\mu^-$  inverse momentum distributions in Z data, as seen in equation (6.1)

$$\Delta = \pm \frac{1}{2} \left( \left\langle \frac{1}{p_{\mu^+}} \right\rangle - \left\langle \frac{1}{p_{\mu^-}} \right\rangle \right) \quad (6.1)$$

where the positive sign shift was applied to  $\mu^-$  and negative sign to  $\mu^+$ . The magnitude of the shift was  $0.14\%$ . One could argue that the shift applied should depend on the polar angle of the muon. In reference [56] where the corrections applied in this analysis were determined, the muon samples were divided into six polar angle ranges, as mentioned above. However when the same was done to the remaining differences between the inverse momentum for  $\mu^+$  and  $\mu^-$  in the data, the polar angle dependence was not statistically significant.

The systematic uncertainties due to the difference between  $\mu^+$  and  $\mu^-$  inverse momentum are shown in table 6.1. These numbers were expected to be very close to zero due to the nature of the shift applied.

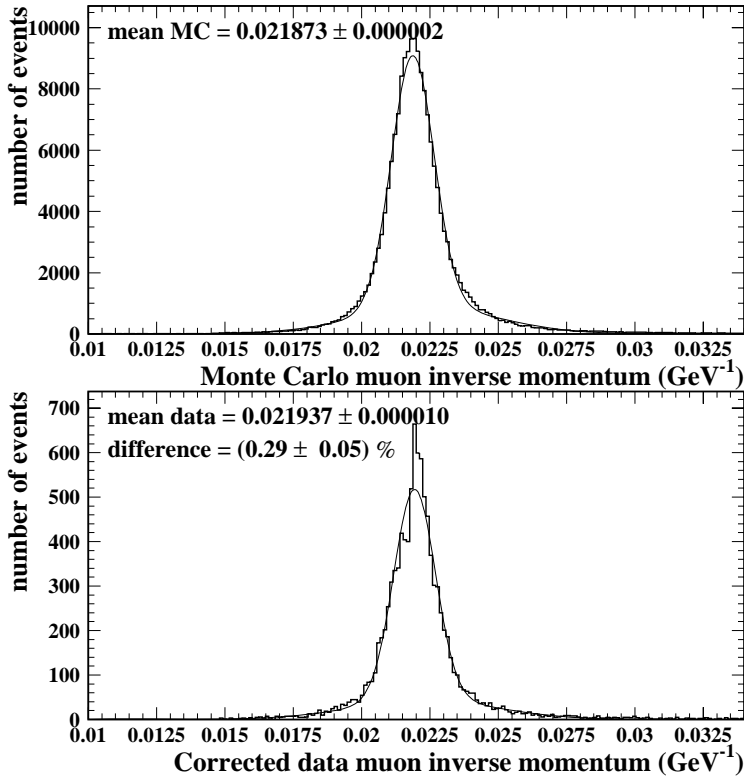


Figure 6.1: *Di-muon events collected during a calibration run in 1999. The upper plot shows the inverse momentum distribution for Monte Carlo and the bottom plot shows the same distribution for data with corrections applied to the muon inverse momentum. A double Gaussian was fitted to both distributions. The fitted mean of the distributions is indicated on top left of each plot. The relative difference between the means is indicated on the top left of the bottom plot.*

### 6.1.3 Muon inverse momentum resolution

The inverse momentum resolution in the Monte Carlo was found to be around 4.5% better than that in the data. Once again standard WWANA corrections were used to correct for the discrepancy between data and Monte Carlo. The Monte Carlo events were smeared with a double Gaussian. The smearing was determined separately for four regions of the polar angle of the muons. In order to study the impact of these corrections on the W mass the original smearing was increased by 50% and it was then applied to simulated events. The resulting shifts in the W mass are considered as systematic error and are shown in table 6.1.

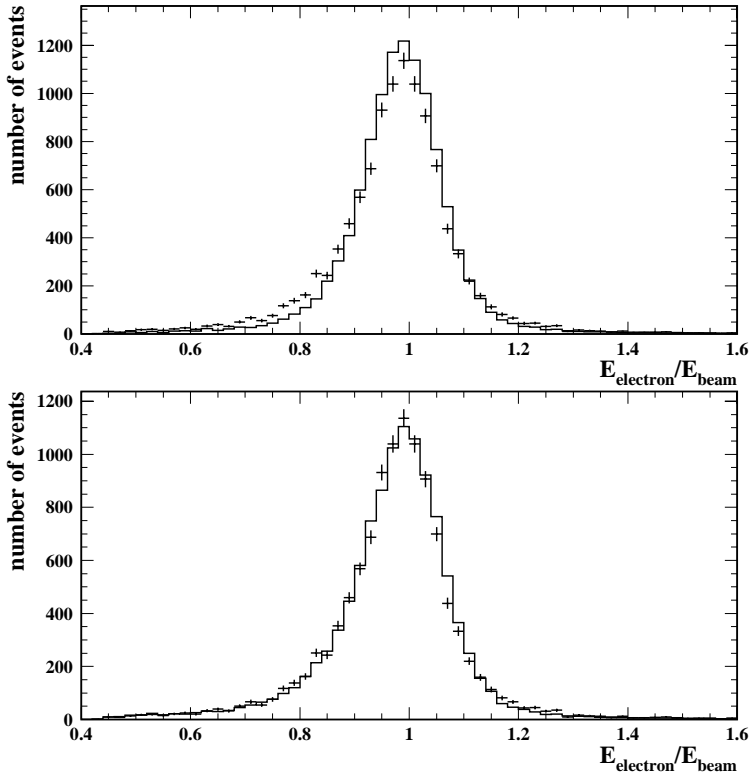


Figure 6.2: *Bhabha events collected during a calibration run in 1999. The upper plot shows the data-Monte Carlo agreement without corrections applied and the bottom plot with corrections to the electron energy in the Monte Carlo. The points correspond to the data and the histogram to the Monte Carlo.*

### 6.1.4 Electron energy scale

The contribution to the systematic error on the W mass due to the reconstruction of electrons is discussed in this section and the two following ones. This was studied using Bhabha events at the Z peak and at high energies. Bhabha events collected at the Z peak are used to determine the energy scale for electrons. Standard WWANA corrections are applied to account for the discrepancies found between the reconstructed energy for data and Monte Carlo. The ratio of the electron energy and the beam energy,  $E_{electron}/E_{beam}$ , is used to study this. The discrepancies are attributed to the fact that in the region in front of the electromagnetic calorimeter in the end-caps the amount of material is under-estimated in the Monte Carlo. The correction, which is applied to Monte Carlo, consisted of introducing the effect of extra bremsstrahlung emission corresponding to an additional 3% of a radiation length [22]. These corrections were determined separately for each year and the sample was

divided in four regions of the polar angle. The impact of the corrections can be seen in figure 6.2.

In order to search for remaining discrepancies between data and Monte Carlo a simple event selection to select electron pairs was applied. Two electrons had to be identified by the REMCLU package and the following cuts were imposed on these two electrons:

- A maximum acollinearity of  $10^\circ$ ;
- The number of charged tracks in the event had to be less than 5 for events in the barrel;
- At least one of the two clusters should have an energy of 20 GeV or higher.

Effect	$m_W$ systematic errors in electron channel (MeV)			
	183	189	200	206
energy scale	4	8	9	11
energy resolution	0	0	1	0
energy linearity	9	12	20	14

Table 6.2: Systematic uncertainties for the  $q\bar{q}e\nu_e$  channel. The results are all in MeV and are presented at four centre-of-mass energies.

After applying the standard WWANA corrections to the selected  $e^+e^-$  events in the Monte Carlo the mean of the  $E_{electron}/E_{beam}$  distribution was compared with the one for the data events. The difference between the mean of the two distributions was not statistically significant as can be seen in figure 6.3. Therefore the error on this difference was used to (conservatively) estimate the uncertainty on the W mass due to the corrections applied to the electron energy. A scale factor of  $-0.13\%$  was then applied to the electron energy and momentum of all Monte Carlo events used for the W mass analysis. The systematic uncertainty obtained by applying this correction is presented in table 6.2.

### 6.1.5 Electron energy resolution

The resolution of the electron energy in the Monte Carlo was found to be around 2% better than in the data. The standard WWANA correction was applied to simulated events and it consisted of smearing the electron energy with a Gaussian. The smearing factors were determined separately for four polar angle regions and again for each year of data taking. In order to estimate the systematic error due to this correction an extra smearing of 1% was applied to the electron energy in the Monte Carlo. The systematic error due this is shown in table 6.2.

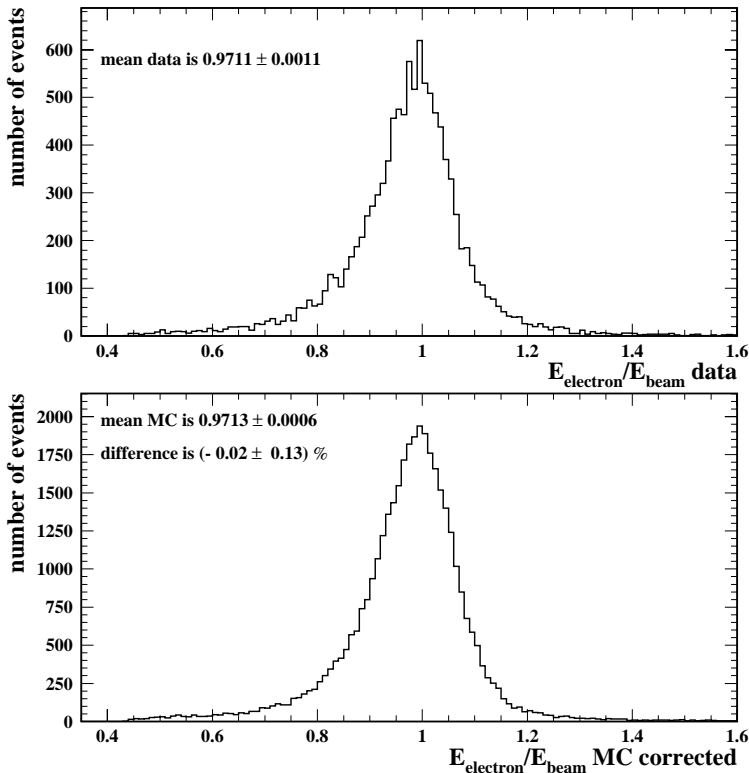


Figure 6.3: *Bhabha events collected during a calibration run in 1999. The upper plot shows the ratio  $E_{\text{electron}}/E_{\text{beam}}$  for data and the bottom plot shows the same ratio for Monte Carlo with corrections applied to the electron energy. The mean of the distributions are indicated on top left of each plot. The relative difference between the means is indicated on the top left of the bottom plot.*

### 6.1.6 Electron energy linearity

The purpose is to study how the electron energy scales as a function of the electron energy itself. The electron energy linearity was studied by comparing the electron energy of Bhabha events collected at different centre-of-mass energies. The three energy points used for that were 91 GeV, 189 GeV and 200 GeV. In order to select Bhabha events at the centre-of-mass energies above the Z resonance a few modifications were made to the selection described in section 6.1.4. The event selection for Bhabha events collected at 189 GeV and 200 GeV requires that two electrons identified by REMCLU pass the following cuts:

- A maximum acollinearity of  $10^\circ$ ;
- The number of charged tracks in the event had to be less than 5 for events in the barrel;

- The energy of the highest energetic electron should be greater than 65% of the beam energy  $E_{beam}$ ;
- If the selected electrons were in the forward region then no tracks should be found in the barrel.

Using the selected events the double ratio  $\langle E_{electron}/E_{beam} \rangle_{data} / \langle E_{electron}/E_{beam} \rangle_{MC}$  was evaluated at the three centre-of-mass energies mentioned above. The ratio was determined separately for barrel events and endcap events. The three points obtained were plotted against the beam energy. A slope was determined. The deviation of the slope from zero was found to be 0.013% for the forward region and 0.012% for the barrel. This slope was used to scale the energy of the simulated electrons in the W mass analysis. The resulting electron energy linearity systematic uncertainties are shown in table 6.2.

### 6.1.7 Tau reconstruction

The  $q\bar{q}\tau\nu_\tau$  channel differs from the other two WW semi-leptonic decay channels since these events contain two (or even three for leptonic tau decays) neutrinos in the final state. This means that, in this channel, the W mass in these events is determined from only the decay products of the W decaying hadronically. Thus the systematic uncertainties due to lepton reconstruction described in the previous sections are not relevant to this channel.

### 6.1.8 Jet energy scale

The following study was also performed using events collected during calibration runs at the Z peak. In order to select  $Z \rightarrow q\bar{q}$  events the following cuts were applied [57]:

- The event was required to have at least 4 charged tracks;
- The total charged energy in the event had to represent at least 12% of the centre-of-mass energy;
- If the number of charged tracks in the event was less than 11 the following selection was required in order to reject Bhabha events:

$$\sqrt{E_{for}^2 + E_{back}^2} < 0.9 \cdot E_{beam} \quad (6.2)$$

where  $E_{for}$  and  $E_{back}$  are respectively the energies recorded in the forward and backward sections of the FEMC electromagnetic calorimeter and  $E_{beam}$  is the beam energy.

It is known that the quark content in jets from Z events is not the same as in WW events. In WW events b quarks are very rarely present. In order to make the Z samples have a quark content that is more similar to the one in WW events the b-tagging technique was used to

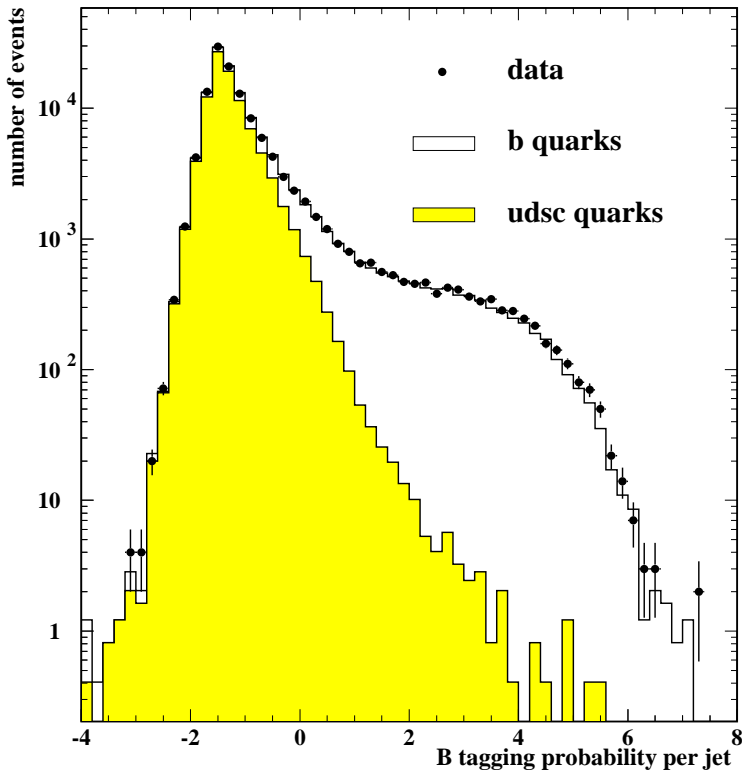


Figure 6.4:  $B$ -tagging variable per jet in  $Z$  decays. The dots represent the data and the histograms represent the Monte Carlo. The grey histogram accounts for events containing  $u$ ,  $d$ ,  $s$  and  $c$  quarks and the white histogram for events containing  $b$  quarks.

exclude  $b$  quarks. The combined  $b$ -tagging, which uses information about the life-time of the particles combined with a search for a secondary vertex, was used [58, 59]. In figure 6.4 one can see the combined  $b$ -tagging variable plotted for all jets, where the contributions from  $b$ -jets and non- $b$ -jets are plotted separately. In order to exclude the  $b$ -jets only events with  $b$ -tagging probability lower than  $-1$  were accepted. Once the events were selected and forced into two jets, standard WWANA corrections to the jet energy were applied to the Monte Carlo [49]. An offset which was a quadratic function of the energy was applied to the jet energy itself. The corrections were determined for four bins of the polar angle.

These corrections were then also applied to  $Z$  Monte Carlo events. After doing that the remaining differences between the mean of the  $E_{jet}/E_{beam}$  for data and Monte Carlo were determined. In figure 6.5 one can see the  $E_{jet}/E_{beam}$  distribution for data events and for Monte Carlo after corrections were applied. The difference between the mean of the two distributions is indicated on the top left corner of the bottom plot. This difference was used to estimate the systematic error due to this correction. Table 6.3 shows the systematic error

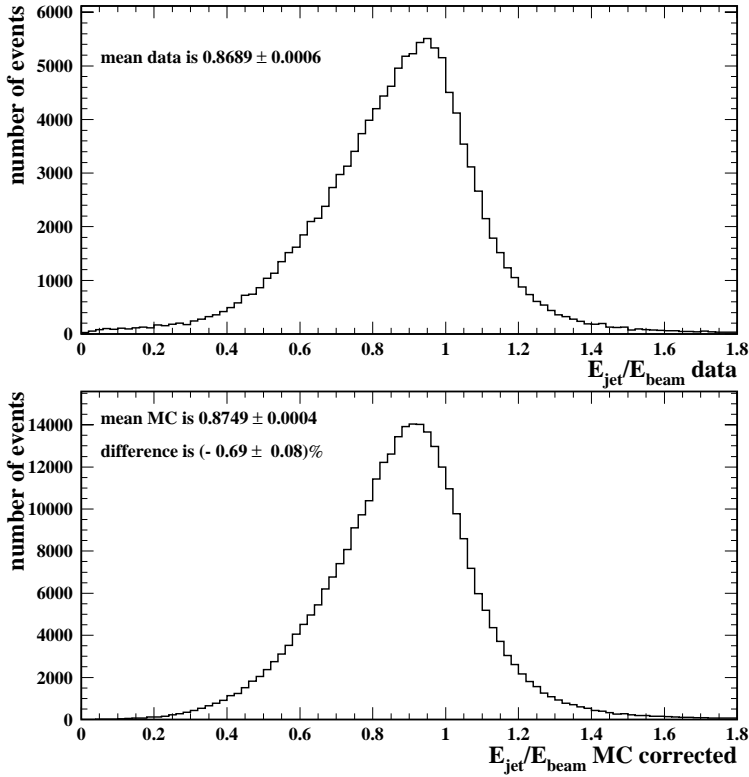


Figure 6.5: *Di-jet events collected during a calibration run in 1999. The top plot shows  $E_{jet}/E_{beam}$  for the data and the bottom shows the same quantity for the corrected Monte Carlo. The mean of the distributions are indicated on the top left corner of both plots. The relative difference between the means is indicated on the top left of the bottom plot.*

on  $m_W$  due to this correction.

### 6.1.9 Jet energy resolution

The standard WWANA corrections consisted of smearing of the jets energy, polar and azimuthal angles in the Monte Carlo [49]. The jet energies were smeared with a Gaussian. The smearing factor was parameterised as a quadratic function of the energy itself with function shown below:

$$(0.51 \pm 0.12) + (0.16 \pm 0.63) \cdot 10^{-2} \cdot E + (0.81 \pm 0.08) \cdot 10^{-3} \cdot E^2 \quad (6.3)$$

The polar and azimuthal angles of the jet were smeared by  $0.36^\circ$  and  $0.45^\circ$  degrees respectively. In order to study the systematic uncertainty introduced by these corrections an extra smearing was applied to the simulation. The magnitude of the smearing was chosen to be

equal to the errors on the parameters used to smear the energy and angles originally. The systematic uncertainty is presented in table 6.3.

Jet systematic errors on $m_W$ (MeV)						
	183 GeV			189 GeV		
Effect	channel					
	$q\bar{q}e\nu_e$	$q\bar{q}\mu\nu_\mu$	$q\bar{q}\tau\nu_\tau$	$q\bar{q}e\nu_e$	$q\bar{q}\mu\nu_\mu$	$q\bar{q}\tau\nu_\tau$
energy scale	10	9	11	13	12	22
energy resolution	4	2	12	5	4	16
energy linearity	0	2	2	2	3	7
forward tracks	2	6	13	2	1	11
	200 GeV			206 GeV		
Effect	channel					
	$q\bar{q}e\nu_e$	$q\bar{q}\mu\nu_\mu$	$q\bar{q}\tau\nu_\tau$	$q\bar{q}e\nu_e$	$q\bar{q}\mu\nu_\mu$	$q\bar{q}\tau\nu_\tau$
energy scale	18	14	22	16	17	29
energy resolution	10	2	2	6	3	4
energy linearity	4	3	2	3	3	1
forward tracks	7	0	2	3	5	16

Table 6.3: Systematic uncertainties on the W mass due to jet reconstruction. The results are all in MeV and are presented at 183 GeV, 189 GeV, 200 GeV and 206 GeV.

### 6.1.10 Jet energy linearity

In order to study how the jet energy scales with the jet energy itself the behaviour of di-jet events above the Z resonance was studied. The event selection used here was slightly different from the one used for di-jet events at the Z peak. The cuts imposed were:

- At least 7 charged tracks;
- The charged energy represents at least 10% of the centre-of-mass energy;
- If the number of charged tracks was less than 11 the following selection was required:

$$\sqrt{E_{for}^2 + E_{back}^2} < 0.9 \cdot E_{beam} \quad (6.4)$$

where  $E_{for}$  and  $E_{back}$  are respectively the energies recorded in the forward and backward sections of the FEMC electromagnetic calorimeter;

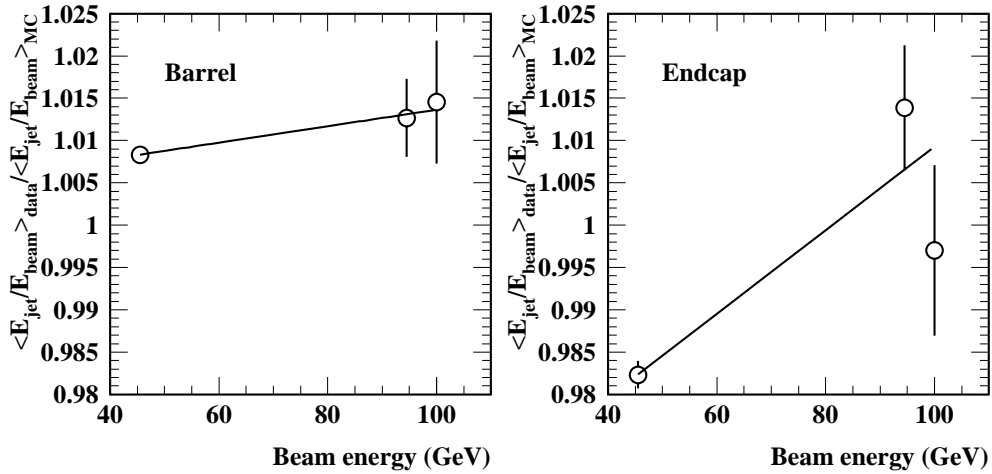


Figure 6.6: The double ratio  $\langle E_{jet}/E_{beam} \rangle_{data} / \langle E_{jet}/E_{beam} \rangle_{MC}$  is plotted as a function of the beam energy for events in the barrel and in the endcaps separately. A linear function was fitted to both plots.

- The transverse energy represents at least 20% of the centre-of-mass energy;
- The effective centre-of-mass energy  $\sqrt{s'}$  should be larger than  $0.95 \cdot \sqrt{s}$ .
- The difference between the estimated jet energy and the beam energy has to be smaller than 10 GeV. See text below for how the jet energy is estimated.

The effective centre-of-mass energy  $\sqrt{s'}$  was determined using three-body kinematics and uses only the angular information from the decay products. The bodies in question were the two jets and a hypothetical photon and their masses were neglected. The photon was assumed to go undetected along the beam direction. The estimated jet energy referred to above is the one obtained using the three-body kinematics.

Events were selected at two high energy points, 189 GeV and 200 GeV. Here again the ratio  $E_{jet}/E_{beam}$  was plotted for the data and for the corrected Monte Carlo. The double ratio of the average values  $\langle E_{jet}/E_{beam} \rangle_{data} / \langle E_{jet}/E_{beam} \rangle_{MC}$  was evaluated. These quantities were plotted against the beam energy for the three data points available as can be seen in figure 6.6 and a slope was determined. The deviation of the slope from zero was found to be 0.05% for the forward region and 0.01% for the barrel. The simulated measured jet energies in the WW analysis were shifted according to the slopes above. The systematic error due to the jet energy linearity was determined by taking the difference between the standard W

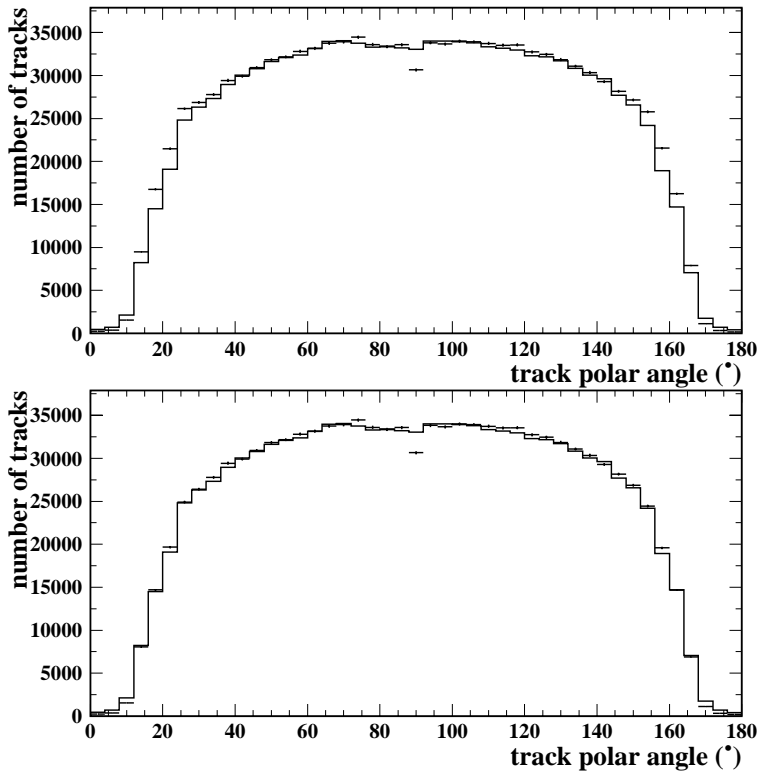


Figure 6.7: *Di-jet events collected during a calibration run in 1999. The top plot shows the polar angle of tracks before corrections and the bottom plot shows the same quantity with corrections applied to the data. The dots represent the data and the histogram represents the Monte Carlo.*

mass analysis and the one with the shift applied to measured jet energies in the Monte Carlo. The jet energy linearity systematic uncertainties are shown in table 6.3.

### 6.1.11 Forward tracks correction

An excess of tracks in the forward region in the data in comparison to Monte Carlo is observed. The most likely cause of this effect is an underestimation of the track reconstruction efficiency for low momentum particles at low polar angles in the simulation. Standard WWANA corrections were applied [36]. The correction was determined using Z peak  $q\bar{q}$  data from calibration runs and was applied to data events. It consisted of randomly removing a fraction of the forward tracks. The distribution of the polar angle of the tracks for data before and after correction and for Monte Carlo can be seen in figure 6.7. The correction was applied for tracks with a polar angle between  $9^\circ$  and  $30^\circ$  and between  $150^\circ$  and  $171^\circ$ .

In order to estimate the systematic uncertainty the residual difference between data and Monte Carlo was computed by calculating the ratio of the number of tracks in data and Monte Carlo. If an excess of data tracks was still observed in the forward region, tracks were randomly discarded. This ratio was determined for forward tracks with polar angles given above and it was done separately for different momentum ranges. The W mass was obtained with these extra corrections applied. A comparison between this value and the W mass obtained with the standard analysis yields an estimate of the systematic uncertainty due to these residual differences. However this value has a large statistical component.

Instead the correction was applied to Monte Carlo. Removing tracks from Monte Carlo will obviously only make the data Monte Carlo agreement worse. But the purpose here is to get an estimate of the magnitude of the systematic uncertainty without large statistical fluctuations playing a significant role. Therefore the difference between the result obtained by applying the correction for the residual difference to Monte Carlo and the standard W mass analysis result was chosen to be quoted as the systematic error. This error is shown in table 6.3.

### 6.1.12 Aspect ratio

The aspect ratio is defined as the length to width ratio of the detector. Its precision is determined by the precision of the position and dimensions of the Vertex Detector, since the DELPHI detector is aligned relative to this detector. A mistake in the determination of the aspect ratio would lead to a bias on the measurement of the polar angle  $\theta$  which would therefore introduce a bias on the reconstructed W mass. The study described in reference [36] determined that the uncertainty on the aspect ratio is  $3 \cdot 10^{-4}$ . In order to study the effect of this uncertainty on the W mass the  $z$  component of the momentum of all tracks was scaled by the same amount. This scaling was applied to simulated events only. The analysis was repeated with this modified Monte Carlo and the W mass was determined. The difference between this value and the value obtained with the standard analysis is what is quoted as systematic uncertainty. The results can be seen in table 6.4.

channel	Aspect ratio error on $m_W$ (MeV)			
	183	189	200	206
$q\bar{q}e\nu_e$	7	5	4	5
$q\bar{q}\mu\nu_\mu$	1	3	2	6
$q\bar{q}\tau\nu_\tau$	5	2	4	5

Table 6.4: Systematic errors due to the uncertainty in the knowledge of the aspect ratio of the detector. The results are shown at four centre-of-mass energies in GeV.

## 6.2 Mixed Lorentz Boosted Zs (MLBZ)

The aim of the Mixed Lorentz Boosted Zs method as used in this thesis is to have a model-independent estimate of the systematic uncertainty due to fragmentation effects. This was done here by using Z events collected during calibration runs to construct fake WW events.

The outline of the method is as follows:

- The first step is to select the relevant Z events. In order to construct a fake semi-leptonic WW event, the so-called MLBZ, one uses one Z event which decays to a pair of quarks and another Z decaying to a pair of leptons. Each Z decay is used to represent in the emulated WW process the decay of the W boson in its rest frame.
- The second step is to generate the so-called MLBZ event. One of the two leptons from the Z di-lepton decay is randomly picked and it is then combined with the quark pair from the Z hadronic decay.
- The event is rotated, scaled and boosted in order to emulate a WW event. In this step a simulated WW event is used as template to the MLBZ.
- After the MLBZ is generated, this WW-like event goes through the complete W mass analysis, *i.e.* the one described in this thesis. This is done for MLBZ events built using Z data events and also for Monte Carlo ones. A W mass is extracted for data events and for Monte Carlo, the difference between these masses is a measurement of the systematic uncertainty.

The following sections describe in more detail each of the steps mentioned above. They will also show the results obtained using the MLBZs and finally discuss the systematic uncertainties which can be estimated by this method. For a more comprehensive description of the method see reference [53].

### 6.2.1 The Z samples and the Z tag

The Z data samples used came from calibration runs taken in 1999. The size of the data and the Monte Carlo samples used are shown below:

- $Z \rightarrow \mu^+ \mu^-$ : 94,000 simulated events,
- $Z \rightarrow e^+ e^-$ : 22,000 simulated events,
- $Z \rightarrow \tau^+ \tau^-$ : 30,000 simulated events,
- $Z \rightarrow q\bar{q}$ : 120,000 simulated events,
- $Z \rightarrow q\bar{q}$ : 115,000 data events.

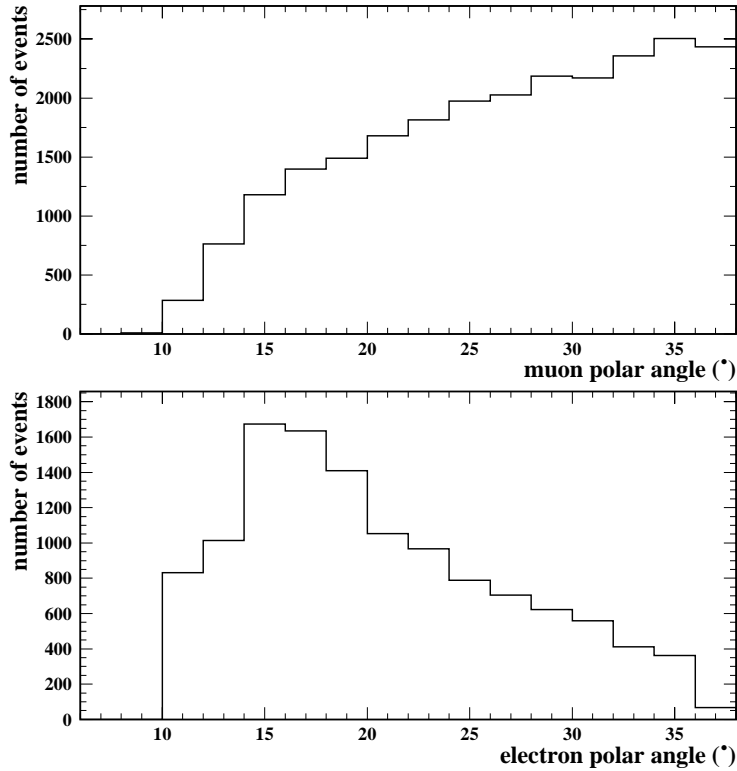


Figure 6.8: Polar angle distributions for muons and electrons in the forward region. These are simulated  $Z \rightarrow \mu^+ \mu^-$  events for the top plot and simulated  $e^+ e^-$  events for the bottom plot. These plots are used to calculate the ratio of muon over electron events explained in the text.

Only simulated leptons were used. The reason for this was the limited data statistics in the di-lepton channel. Besides, the systematic errors due to lepton reconstruction were already covered in sections 6.1.1 to 6.1.6. A simple tagging routine was used to select  $Z \rightarrow q\bar{q}$  events which was the same tagging described in section 6.1.8.

For  $Z \rightarrow l^+ l^-$  no selection was needed since only Monte Carlo events were used. In the case of  $e^+ e^-$  events there are two diagrams, s-channel and t-channel, contributing to this final state while for  $Z \rightarrow \mu^+ \mu^-$  only one. One would like the polar angle distribution for muons and for electrons to be similar for practical purposes. In practice the t-channel electrons tend to be in the forward direction. In order to decrease the number of electrons in the forward region the following cut was applied. The polar angle distribution of  $e^+ e^-$  events was compared to the same distribution for  $Z \rightarrow \mu^+ \mu^-$ . These distributions can be seen in figure 6.8. The ratio of  $\mu^+ \mu^-$  events over  $e^+ e^-$  events is determined and normalised. For the  $e^+ e^-$  channel events were subsequently randomly discarded with a probability obtained

from this ratio.

## 6.2.2 Generating the MLBZs

Once the appropriate Z events were selected the generation of the MLBZ events could begin. The MLBZ event is rotated, scaled and boosted according to the 4-vectors of the chosen WW template event. The template event comes from a list of WW simulated events generated with WPHACT. The list contains the generated 4-vectors of the four fermions. The purpose of this list is to emulate WW events in a more precise way which makes the method as a whole more reliable. The rotation, scaling and boosting goes as follows. The first step is to make sure that the polar angle distribution of the Z events used matches that of the WW template events. To do that one of the decay products of a W from a WW template event is chosen at random. Subsequently a Z event is selected of which the polar angle of the thrust axis matches the polar angle of the selected fermion. The W from the template event is then boosted to its rest frame and the selected Z event is rotated such that the thrust axis is aligned with the angles of the W decay products. The energies of the Z decay products are rescaled by a factor  $m_W/2E_{beam}$  where  $m_W$  is the mass of the W boson in the template event and  $E_{beam}$  is the beam energy of the Z calibration run. Finally the Z event is boosted into the laboratory frame of the template event.

The procedure described above is done once for each W in the WW template event. For the W decaying semi-leptonically, the neutrino in the MLBZ event is faked by removing one hemisphere of the  $Z \rightarrow l^+l^-$  event. The resulting MLBZ events have to lie within the acceptance of the detector, otherwise they are discarded.

Around 900,000 MLBZ events were produced for each channel ( $q\bar{q}e\nu_e$ ,  $q\bar{q}\mu\nu_\mu$  and  $q\bar{q}\tau\nu_\tau$ ) at 200 GeV centre-of-mass energy. In order to produce such a large number of events the original Z events had to be used more than once. Besides that the WW template event can be used more than once too. This introduces some correlations between the generated MLBZ events. Note, however, that due to the many possible ways of matching template events to Z events these correlations are diminished significantly.

The simulated MLBZ events were generated using two simulated Z events, one which decays hadronically and one decaying into two leptons. The data MLBZ events were generated using a data  $Z \rightarrow q\bar{q}$  event and a Monte Carlo  $Z \rightarrow l^+l^-$  event.

These events were then put through the full analysis chain described in chapters 4 and 5 in order to extract the W mass. This was done for the data MLBZs as well as for the Monte Carlo MLBZs.

## 6.2.3 Results and “error on the error”

The systematic uncertainty was obtained by taking the difference between the W mass found using the data MLBZs and the one found using the simulated ones. The MLBZ events were

produced at 200 GeV, the results for the three channels are shown in table 6.5. The statistical error on the mass obtained using MLBZs cannot be extracted in the same way as it is done for the standard W mass analysis. The latter assumes the events are uncorrelated, which is not the case for MLBZs since Z events are used more than once. In order to get an estimate of the statistical error on the W mass the Z sample is split into 10 independent samples and the whole analysis procedure is done for each sample independently. The error on the mass is given by:

$$\frac{RMS}{\sqrt{N_{samples}}} \quad (6.5)$$

where  $RMS$  is the root mean squared of the mass distribution obtained from the 10 independent samples used and  $N_{samples}$  is the number of independent samples. As expected the events turned out not to be highly correlated as the error obtained without splitting samples was almost the same as the one obtained using the split samples.

channel	$m_W^{data} - m_W^{MC}$ (MeV)
$q\bar{q}e\nu_e$	$30.0 \pm 13.5$
$q\bar{q}\mu\nu_\mu$	$12.3 \pm 5.4$
$q\bar{q}\tau\nu_\tau$	$22.2 \pm 8.2$
$q\bar{q}l\nu_l$	$16.8 \pm 4.3$

Table 6.5: MLBZ results at 200 GeV. The table shows the difference in W mass between MLBZs built using data events and MLBZs built using simulation. The last row shows the weighted average of the results for the three channels.

## 6.2.4 Coverage of the MLBZs

Which systematic effects are actually measured by the MLBZ method? In principle one could argue that all systematic effects are covered. In practice there are limitations. These limitations mainly come from the fact that the detector is not Lorentz invariant. For instance the systematic due to the uncertainty in the aspect ratio of the detector is clearly not covered by this method. The rotation of the Z events will destroy the knowledge of any differences between the length and the width of the detector. The fact that only simulated leptons were used also takes away all detector effects which affect the lepton.

However the method is still a very powerful tool to study the jet system and the uncertainties related to it, such as fragmentation and hadronisation and detector effects (concerning jets only). In fact the semi-leptonic channel is a very interesting channel to study the jet description. In the fully hadronic channel, due to the constrained fit some effects which could

disrupt the energy measurement might be wiped out. The same would not happen in the semi-leptonic channel.

It is very hard to determine precisely which systematic effects might or might not be affected by the rotation and boosting of events. It is however worth mentioning that for  $Z \rightarrow q\bar{q}$  events the jets are measured in the  $Z$  rest frame, where they are back-to-back. This means that any measurement errors on the jet angles will have a relatively small influence on the measured invariant mass of the two-jet system. It is therefore assumed here that detector systematics related to measured angles are largely “washed out” due to the inevitable Lorentz boost used by the method. Therefore the systematics due to the correction applied to forward tracks cannot be studied using MLBZs. The systematics on jet energy scale and resolution are less affected by the Lorentz boost. However, conservatively these uncertainties were still estimated separately. Interestingly the fragmentation effects are intrinsically Lorentz invariant and can hence very well be studied in this way. Therefore the obtained data-Monte Carlo difference shown in table 6.5 is interpreted as a model-independent estimate of the systematic error due to fragmentation.

Since the dependence of fragmentation effects on  $\sqrt{s}$  is theoretically well understood the MLBZ study has been performed at only one centre-of-mass energy. The value 200 GeV was chosen because it is close to the central value among all centre-of-mass energies analysed here. In addition there is no reason to believe that fragmentation uncertainties would depend on the lepton in the final state. Indeed no statistically significant difference between the results for the three channels was observed. Therefore the estimated systematic error due to fragmentation was chosen to be the weighted average of the individual results, as shown in table 6.5.

## 6.3 Electroweak radiative corrections

The accuracy in the description of the event by the event generator is of great importance, since the measurements described in this thesis rely on the simulation. The systematic uncertainties quoted in this section are fully based on the studies described in reference [60] and summarised in [22]. The possible sources of uncertainties due to radiative corrections were described in chapter 2. Here the work done in reference [60] in order to extract the systematics errors for each of the effects considered will be briefly described.

The study described in [60] has been performed in the context of the full DELPHI simulation and analysis procedure; furthermore the main uncertainties due to non-CC03 4-fermion background events have been studied. Radiative corrections uncertainties on non 4-fermion background events are included in the uncertainty estimated on the background, which will be addressed in section 6.4.

A summary of the resulting systematic uncertainties due to electroweak radiative corrections is presented in table 6.6.

### 6.3.1 Initial State Radiation

The Initial State Radiation was computed using a leading log  $\mathcal{O}(\alpha^3)$  matrix element. The difference between the best result obtained from implementing the  $\mathcal{O}(\alpha^3)$  matrix element and the  $\mathcal{O}(\alpha^2)$  one gives an estimate of the effect of the higher order missing terms. The missing higher orders lead to the use of a wrong description for events with more than three hard photons or more than one photon with high  $p_t$ .

The difference between the best result and the  $\mathcal{O}(\alpha)$  result includes the previous study, and can be used as an estimate of the upper limit of the effect of missing the non-leading logarithm (NLL) terms at  $\mathcal{O}(\alpha^2)$ ; this effect of missing NLL terms is expected to be smaller than the effect from the LL terms given by this  $\mathcal{O}(\alpha^3)$  to  $\mathcal{O}(\alpha)$  difference.

Also taking into account the study performed in [61], the ISR related uncertainty in the W mass can be conservatively estimated at 1 MeV.

### 6.3.2 Non factorisable corrections

As mentioned in chapter 2, non-factorisable  $\mathcal{O}(\alpha)$  QED interference between W bosons is effectively implemented through the so-called Khoze-Chapovsky ansatz.

The effect of using this ansatz with respect to the Born calculation, where this interference is not described, can be considered as an upper limit of the missing part of the full  $\mathcal{O}(\alpha)$  calculation and of the higher order terms. A dedicated study shows that the effect on the W mass is 1 MeV.

### 6.3.3 Final State Radiation

The Final State Radiation uncertainty due to the hadronic part of the final state is addressed in the fragmentation error. The one due to leptons will be addressed here. Again, the difference between the best result based on NLL and LL treatments provides an estimate of the effect of the missing part of the  $\mathcal{O}(\alpha)$  FSR correction. While the result depends on the semi-leptonic channel, the difference is always less than 1 MeV.

In the study described in [61] the effect of the missing higher orders beyond  $\mathcal{O}(\alpha^2)$  has been found to be negligible at generator level. Simple perturbative QED considerations suggest that the size of the effect should not exceed the size of the effect from the missing part of the  $\mathcal{O}(\alpha)$  FSR correction; therefore conservatively the 1 MeV can be doubled to take into account both of these components of the uncertainty.

### 6.3.4 4-fermion background diagrams: single W

The Double Pole Approximation (DPA) is known to be valid in a few  $\Gamma_W$  intervals around the double resonant pole. The DPA correction is applied only to the CC03 part of the matrix element (and partly to the interference, see [29]); non-CC03 diagram contributions are not

directly affected by the DPA uncertainty (except for possible effects in the interference term which is relevant for the electron channel).

It is clear that this procedure still leaves the problem of the approximated radiative corrections treatment for the non-CC03 part of the matrix element (and the interference). The ISR studies previously discussed can reasonably cover the most relevant part of the electroweak radiative corrections uncertainties present also for the WW-like 4-fermion background diagrams, e.g. the non-CC03 part. There is, however, a notable exception: the so called single W diagrams for the  $q\bar{q}e\nu_e$  final state.

The majority of the single W events are rejected in the W mass analysis, since the electron in these events is lost in the beam pipe. But the CC03 - single W interference is sizeable, and it has a strong impact on the W mass result in the electron channel.

The situation is made even more complex by the cross-talk between channels, e.g. events belonging in reality to one channel but reconstructed as belonging to another one. This cross-talk is particularly relevant between semi-leptonic electron and tau channels, which explains why the  $\tau$  channel analysis is also sensitive to this uncertainty source.

The effect of this uncertainty has been studied in two ways. Firstly, since the uncertainty on the single W rate associated with radiative corrections is known in literature to be about 4%, the non-CC03 part of the matrix element, assumed to be dominated by the single W contribution, has been varied by 4% for  $q\bar{q}e\nu_e$  final states. Another possible source of uncertainty related to 4-fermion background is estimated by partly applying the DPA correction to the interference term [29]. The effect of this way of computing the corrections can be considered as another estimate of the uncertainty related to the 4-fermion background.

The maximal size of these effects is 5.5 MeV for the W mass in the  $q\bar{q}e\nu_e$  channel.

### 6.3.5 Ambiguities in the Leading Pole Approximation definition

One of the two sources of uncertainties mentioned in chapter 2 was the effect of missing higher orders. This can, at least partly, be evaluated by changing the electroweak scheme used in the  $\mathcal{O}(\alpha)$  calculation. This essentially means changing the definition of the QED fine structure constant used in the  $\mathcal{O}(\alpha)$  matrix element [62]. The effect on the W mass is very small, at the limit of the fit sensitivity.

The second, more relevant, source of uncertainty connected to the LPA is in its possible definitions, i.e. the ambiguity present in the way of expanding the amplitude around the double resonant W pole. The standard YFSWW uses the so called  $LPA_A$  definition; a comparison with the  $LPA_B$  one can give an estimate of the effect from the intrinsic ambiguity in the LPA definition. A dedicated study has been performed evaluating the difference between the two in order to evaluate only the effect of the different scheme on the radiative corrections (and not at Born level). The size of the effect is less than 1 MeV for the W mass.

Electroweak Systematic Errors (MeV)			
Uncertainty Source	$q\bar{q}e\nu_e$	$q\bar{q}\mu\nu_\mu$	$q\bar{q}\tau\nu_\tau$
ISR	1	1	1
NF $\mathcal{O}(\alpha)$	1	1	1
FSR	0.5	0.5	1
4- $f$ Background	5.5	0.5	1
LPA	1	1	1
Total	9	4	5

Table 6.6: Summary of the systematic uncertainties on the W mass due to electroweak corrections. Where ISR represents the uncertainty due to Initial State Radiation, NF the one due to non factorisable corrections, 4- $f$  Background the one due to the single W diagrams and LPA the one due to the ambiguity in the definition of the Leading Pole Approximation. The total uncertainty is computed adding linearly the absolute values of all the contributions.

## 6.4 Background description

The two main sources of background events in WW events are 4-fermion and 2-fermion hadronic processes. The theoretical uncertainty due to the 4-fermion background description was already assessed in section 6.3. The dominant source of background comes from  $Z \rightarrow q\bar{q}(\gamma)$  events. The theoretical uncertainty on the 2-fermion cross-section is generally small, not exceeding 2%. In the semi-leptonic channel these events can for instance be selected if there is a high-energy photon emitted within the detector acceptance. This can happen in case of a radiative return to the Z. This is especially true if in addition the photon converts to an electron-positron pair or a random association of forward vertex detector hits to an electromagnetic cluster in the calorimeter occurs. A data-simulation comparison shows that a 10% fluctuation of this type of background cannot be ruled out [22]. Therefore in order to evaluate the systematic uncertainty due to the background level in the semi-leptonic channel a shift of 10% was applied to the  $Z \rightarrow q\bar{q}(\gamma)$  cross-section. The systematic error was determined by comparing the W mass results with and without the rescaling of the  $Z \rightarrow q\bar{q}(\gamma)$  cross-section. The event-by-event-purity used in this analysis helps reduce the impact of the background uncertainty on the W mass.

## 6.5 LEP beam energy measurement

The measured centre-of-mass energy is imposed as a constraint in the kinematic fit. Therefore the precision on this measurement directly affects the precision on the W mass. The relative uncertainty in the W mass will be approximately the same as the relative uncertainty

channel	Background description error (MeV)			
	183	189	200	206
$q\bar{q}e\nu_e$	0	0	1	0
$q\bar{q}\mu\nu_\mu$	0	0	1	0
$q\bar{q}\tau\nu_\tau$	8	13	8	6

Table 6.7: Systematic errors on the  $W$  mass due to the background description.

$E_{\text{cm}}$ (GeV)	183	189	192	196	200	202	206
error on $m_W$ (MeV)	9	9	9	10	10	10	16

Table 6.8: The top row shows the nominal centre-of-mass energy and the bottom one the corresponding error on the  $W$  mass due to the uncertainty on the beam energy

in the centre-of-mass energy itself.

The beam energy estimate was discussed in section 3.1.2. The average LEP collision energy was evaluated every 15 minutes or after significant changes in the beam conditions. The beam energy was estimated using the Nuclear Magnetic Resonance method which was calibrated with the Resonant Depolarisation (RPD) technique. Three different techniques were used as cross-check methods. The errors on the beam energy were already given in table 3.1. For the energy points taken in the year 2000, 205 GeV and 207 GeV, the uncertainty is higher than in previous years. There is an additional uncertainty due to the ‘Bending Field Spreading’ strategy, in which corrector magnets were powered in a coherent manner to increase the overall dipole field and therefore the energy boost [35].

The corresponding uncertainties on the  $W$  mass are shown in table 6.8. Note that in the work described in this thesis the data at 205 GeV and 207 GeV centre-of-mass energies were combined and were referred to as the 206 GeV data set. Therefore the uncertainty quoted for the results at 206 GeV are the luminosity weighted average of the uncertainties for the 205 GeV and 207 GeV centre-of-mass energies.



# Chapter 7

## Final results and conclusions

The combined W mass measurement result for the full data sample of  $641 \text{ pb}^{-1}$  is presented in this chapter. The result is compared to the DELPHI results published in [22] as well as to the current world average.

### 7.1 Correlations

Before combining the results presented in chapters 5 and 6 the correlations among channels, years of data taking and centre-of-mass energies of the systematic uncertainties have to be addressed. The systematic uncertainties in the three channels analysed,  $q\bar{q}e\nu_e$ ,  $q\bar{q}\mu\nu_\mu$  and  $q\bar{q}\tau\nu_\tau$ , are treated as fully correlated in the combination. The uncertainties for different years within one channel, *e.g.*, the systematic errors for the  $q\bar{q}e\nu_e$  channel for the different years of data taking, are conservatively treated as fully correlated, except for the beam energy error. A brief explanation of why this was done follows in the next paragraph. Within one year of data taking with more than one centre-of-mass energy point the systematic errors for a given effect are considered to be identical and therefore also fully correlated, as already discussed in chapter 6.

The systematic error due to fragmentation, which was assessed using the MLBZ method, is treated as identical at different centre-of-mass energies. The error used in the combination was the weighted average of the results obtained for the individual channels. The systematic error due to radiative corrections was also treated as identical at different centre-of-mass energies. All detector systematics were treated as fully correlated since the detector was essentially the same every year. The systematics due to the uncertainty on the knowledge of the background description should also be treated as fully correlated, since this knowledge again does not vary with the centre-of-mass energy. The error due to the uncertainty on the beam energy is treated as fully correlated between channels, but partially correlated for different centre-of-mass energies.

## 7.2 Results and combination

The combination of the results was made taking the correlations discussed above in section 7.1 into account. The results are presented in figure 7.1. This figure shows the  $W$  mass per channel for each centre-of-mass energy with the statistical and systematic uncertainties indicated. The position of the grey vertical band represents the value of the combined  $W$  mass for all centre-of-mass energies and its width the combined uncertainty on it.

The final result for the  $W$  mass, combining the data collected at all seven centre-of-mass energies, which corresponds to  $641 \text{ pb}^{-1}$  of integrated luminosity, is

$$m_W = 80.455 \pm 0.071(\text{stat.}) \pm 0.029(\text{syst.}) \pm 0.009(\text{LEP}) \text{ GeV}, \quad (7.1)$$

where ‘‘LEP’’ indicates the systematic error on the beam energy uncertainty. All the individual results are in agreement within two standard deviations with the combined result.

The  $W$  mass result for the semi-leptonic channel corresponding to a data sample with an integrated luminosity of  $660 \text{ pb}^{-1}$  published in [22] by the DELPHI collaboration is

$$m_W = 80.339 \pm 0.069(\text{stat.}) \pm 0.029(\text{syst.}) \pm 0.009(\text{LEP}) \text{ GeV}. \quad (7.2)$$

The result presented in this thesis is in agreement with the published results. The difference in the magnitude of the statistical error is small and there was no difference in the total systematic uncertainty. Note that the two analyses differ in many important aspects. Most importantly, in the work presented here the fragmentation error is obtained using a model independent approach. This was not done for the semi-leptonic channel in any of the other LEP experiments nor in the work presented in [22]. In addition the approach taken in this thesis is considered to be conservative since it is assumed that the detector effects on jet reconstruction were not covered by the MLBZ method and were thus estimated separately.

The  $W$  mass results per channel for all centre-of-mass energies combined are: for the  $q\bar{q}e\nu_e$  channel

$$m_W = 80.450 \pm 0.147(\text{stat.}) \pm 0.032(\text{syst.}) \pm 0.009(\text{LEP}) \text{ GeV}, \quad (7.3)$$

for the  $q\bar{q}\mu\nu_\mu$  channel

$$m_W = 80.371 \pm 0.096(\text{stat.}) \pm 0.033(\text{syst.}) \pm 0.009(\text{LEP}) \text{ GeV}, \quad (7.4)$$

for the  $q\bar{q}\tau\nu_\tau$  channel

$$m_W = 80.657 \pm 0.147(\text{stat.}) \pm 0.033(\text{syst.}) \pm 0.009(\text{LEP}) \text{ GeV}. \quad (7.5)$$

For completeness a comparison between the results presented in this thesis and the ones in [22] for each of the three selection channels is presented in figure 7.2. As can be seen the largest difference between results happens for the  $q\bar{q}\tau\nu_\tau$  channel. This is perhaps not

surprising given that the selection is performed quite differently in the two analyses and also the special treatment of the tau in the ideogram analysis described in chapter 5.

Note that the individual systematic errors, such as for instance the fragmentation error, are considered to be fully correlated only between channels. Within one channel the individual systematic errors are considered as uncorrelated, which makes sense since for instance the fragmentation error and the uncertainty on the LEP beam energy are evidently independent. When combining the results for the different channels care should be taken. Since for different channels different individual systematic effects contribute with different weights. Therefore the total systematic errors per channel will not be fully correlated. To take the correlations properly into account the order in which the results are combined is important. One should first combine the individual systematic errors over the three channels before adding the resulting errors in quadrature. For both the analysis presented in this thesis as well as for the analysis published in [22], this leads to a somewhat smaller systematic error on the final W mass than would naïvely be expected from looking at the total systematic errors of the individual channels, as can be observed in figure 7.2.

## 7.3 Conclusions and outlook

The final result for this W mass measurement in the semi-leptonic channel is

$$m_W = 80.455 \pm 0.077 \text{ GeV}. \quad (7.6)$$

This result is in good agreement with the current world average [63]:

$$m_W = 80.398 \pm 0.025 \text{ GeV}. \quad (7.7)$$

As already mentioned in chapter 1 the measurement of the W mass provides a powerful check of the Standard Model. The result of the work described in this thesis, no matter how indirectly, adds one more grain of sand to the pile of results that are in support of the Standard Model. As for the coming grains of sand, the current Tevatron results are still preliminary and are going to be improved. The start of the LHC is in sight and the prospects of a linear collider will keep open the possibilities for ever more precise checks to come. By performing a scan around the W-pair production threshold at TESLA, for example, one expects to reach an uncertainty of 6 MeV on the W mass [64]! The expected error on the top mass would be around 100 MeV. These numbers enable a constraint at the level of 5% on the Higgs mass. In case the Higgs boson would not have been found by that time one would know very well where to look for it. Another possibility is that its measured mass would be inconsistent with the predicted value and therefore the Standard Model would no longer be fail proof.

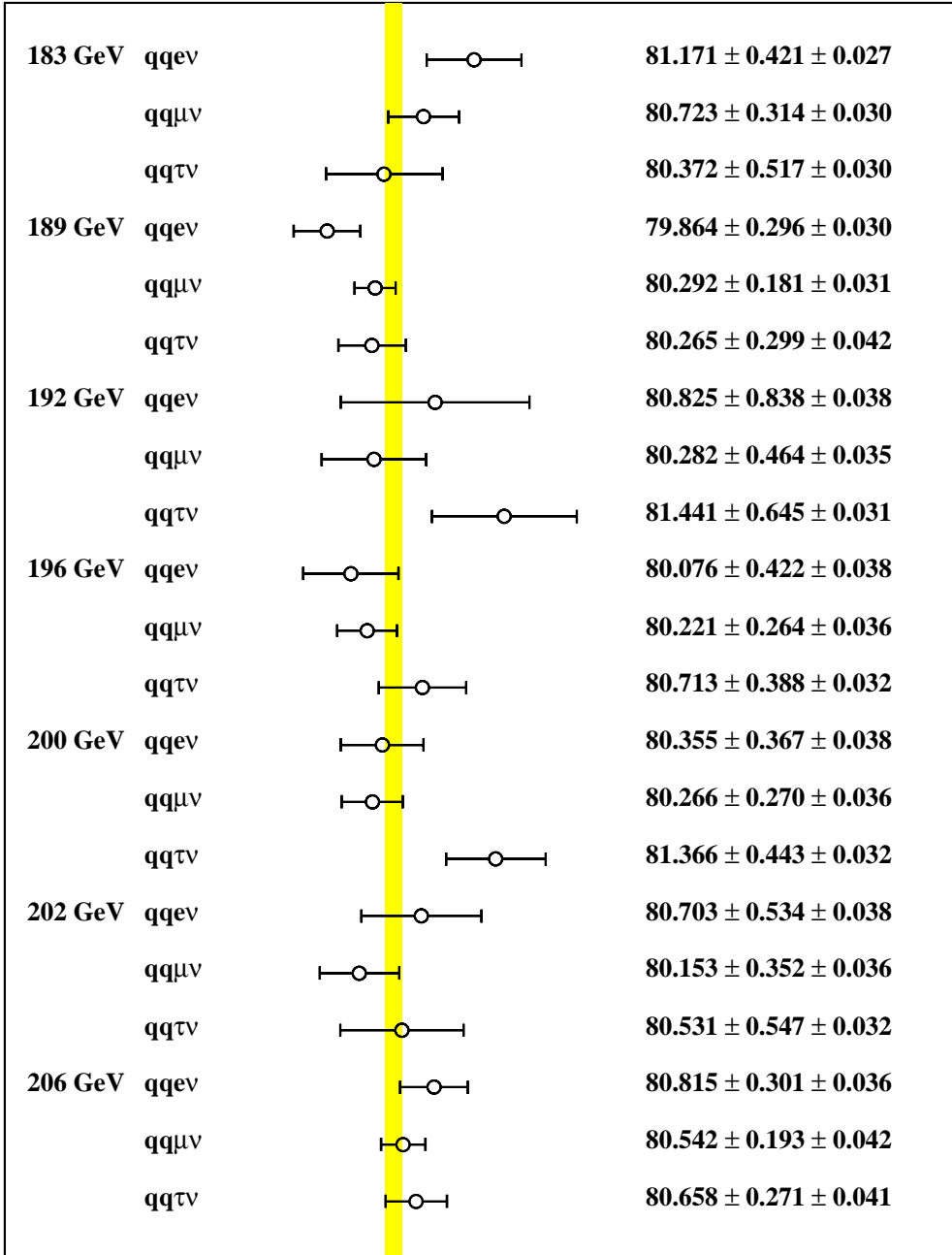


Figure 7.1: This figure shows the final  $W$  mass results for each channel at all centre-of-mass energies. The dots represent the  $W$  mass values and the error bars for the statistical and systematic uncertainties are plotted. The centre-of-mass energy and the channel are indicated on the left side and the value of each point is indicated on the right hand side. The grey band represents the combined  $W$  mass and the width of the band indicates the total uncertainty on it.

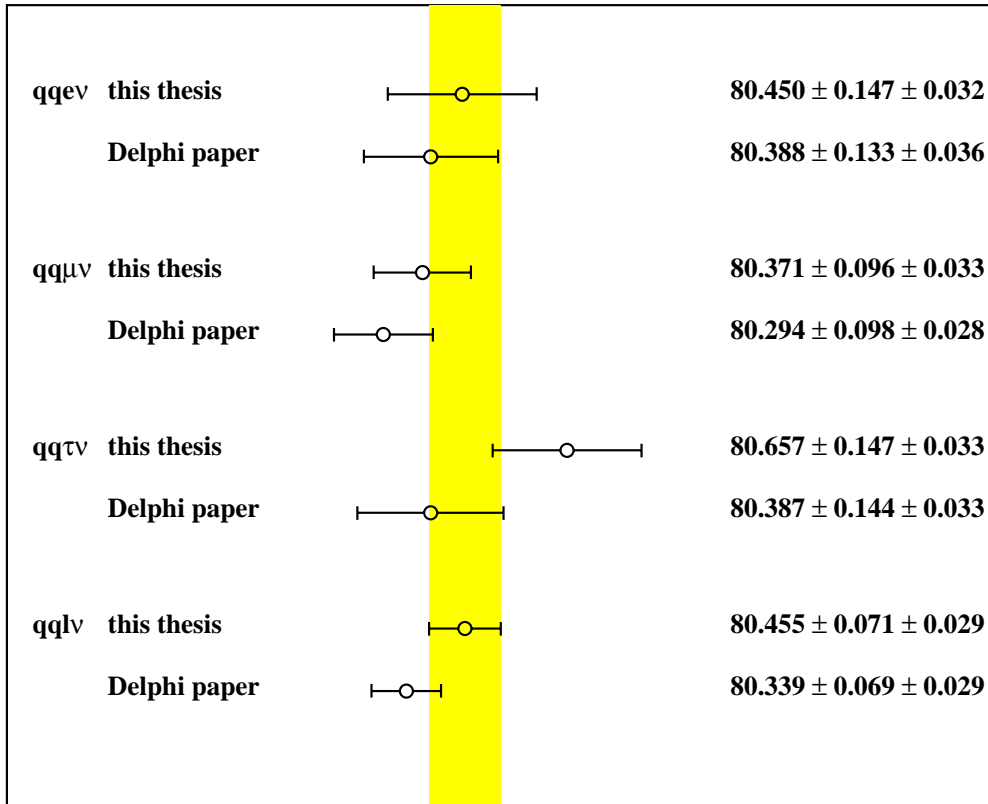


Figure 7.2: This figure shows the final  $W$  mass results for each channel for all centre-of-mass energies combined for this thesis and for reference [22]. The dots represent the  $W$  mass values and the error bars for the statistical and systematic uncertainties are plotted excluding the error on the LEP beam energy. The grey band represents the combined  $W$  mass result for this thesis and the width of the band indicates the total uncertainty on it.



# Appendix A

## Selection variables

### A.1 Variables at 189 GeV and 206 GeV

The observables used to construct the discriminant variables as well as the resulting discriminant variables themselves at 189 GeV and 206 GeV are shown here. The first plots shown are for the event selection at 189 GeV centre-of-mass energy. Figure A.1 shows the observables used to construct the discriminant variable in the  $q\bar{q}e\nu_e$  channel and figure A.2 the first and second discriminant variables for that channel. Figures A.3 and A.4 show the corresponding plots for the  $q\bar{q}\mu\nu_\mu$  channel. The plots for the  $q\bar{q}\tau\nu_\tau$  channel are shown in figures A.5, A.6 and A.7 and the corresponding plots for the  $q\bar{q}\tau_{1p}\nu_\tau$  channel follow in figures A.8 and A.9. Figures A.10 to A.18 show the same distributions used for the 206 GeV event selection.

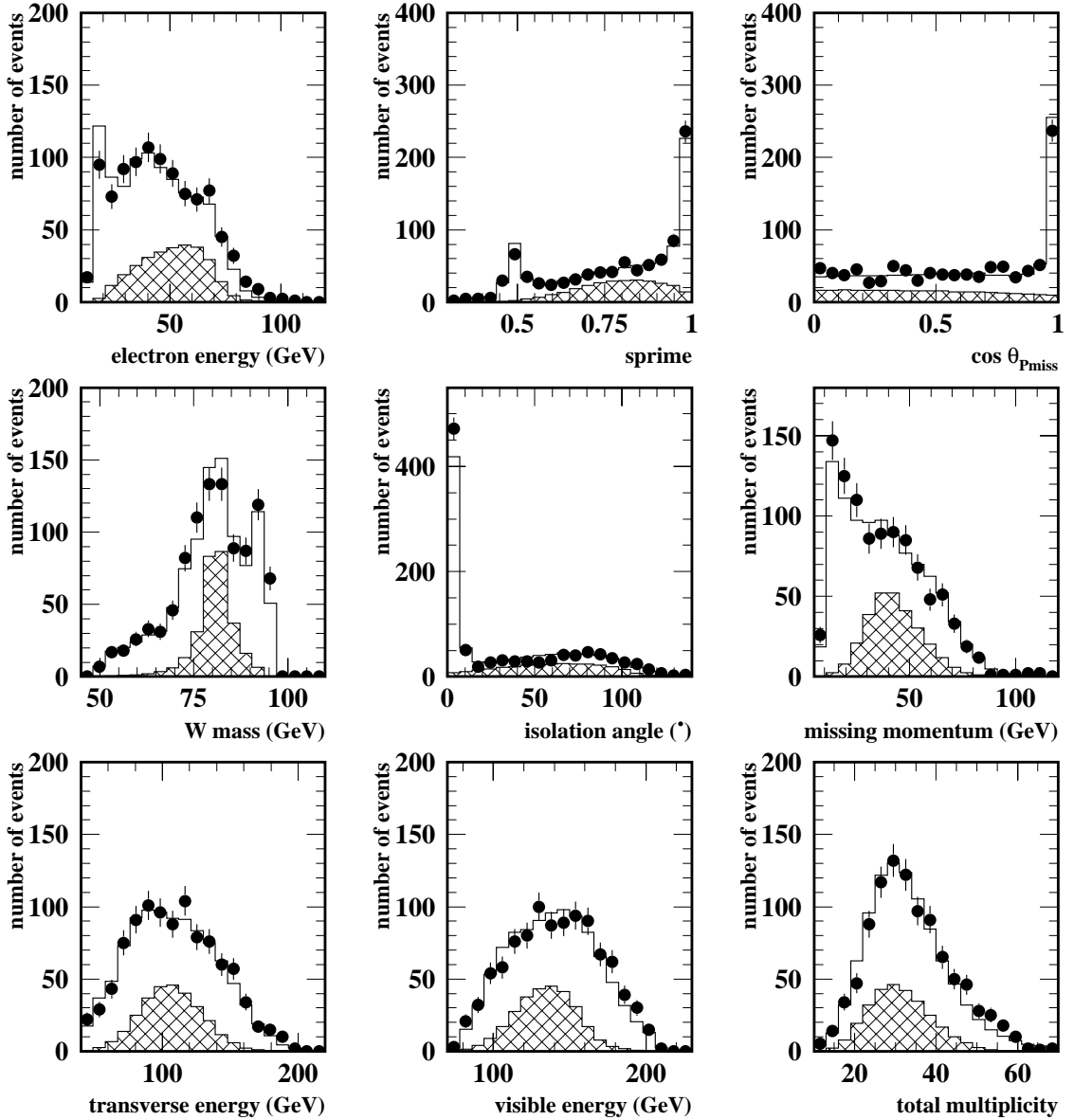


Figure A.1: *Data-Monte Carlo agreement plots for the observables used to construct the discriminant variables for electrons at 189 GeV. The dots represent the data, the hatched histograms represent the signal events and the white histograms account for signal plus all background processes combined. These plots were made with events which passed the pre-selection. This legend is valid for all subsequent plots in this appendix.*

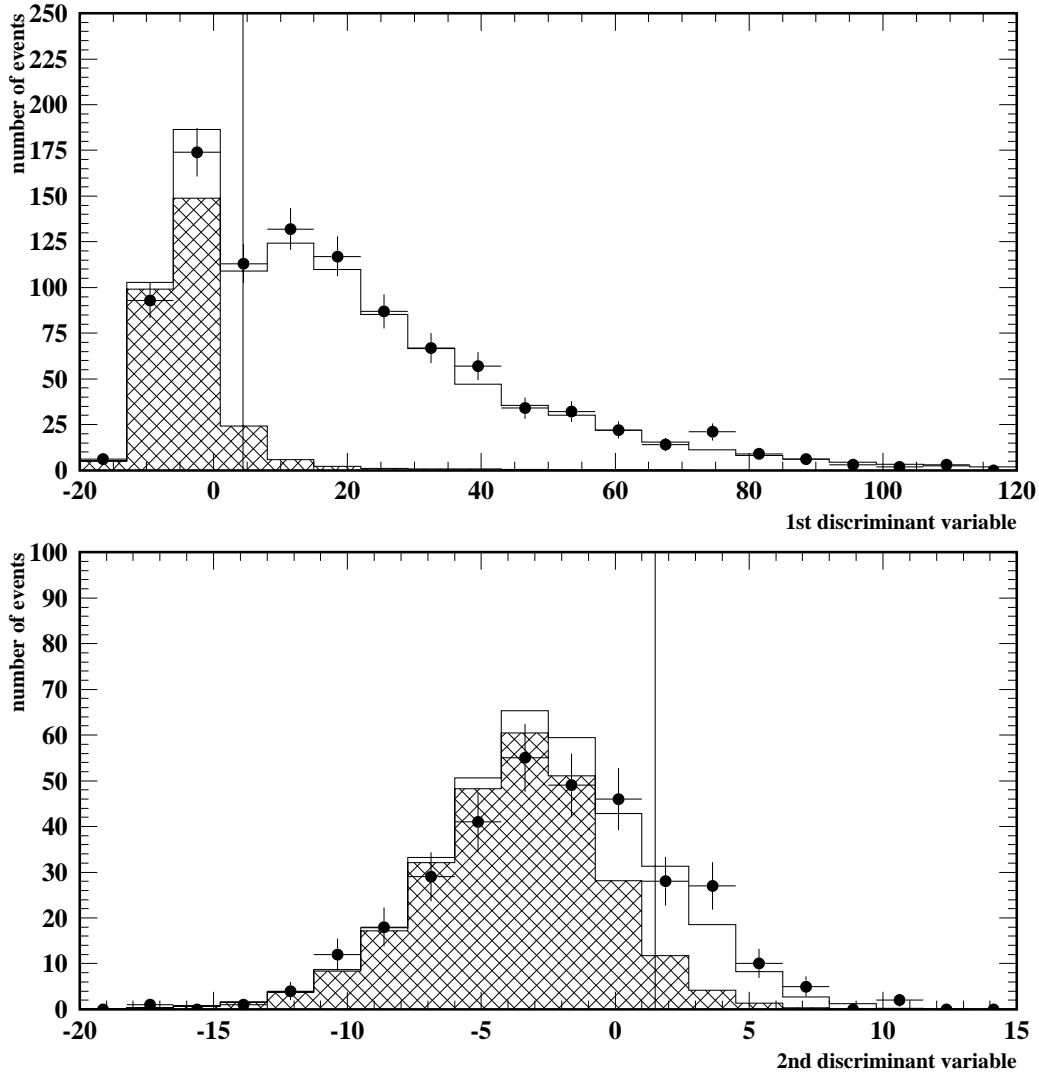


Figure A.2: First and second discriminant variables for electrons at 189 GeV. The vertical line represents the cut in the distribution in order to distinguish signal events from background ones. The events which pass the cut on the first discriminant variable are used as input for the second discriminant variable. The events which pass the cut on the second discriminant variable are selected.

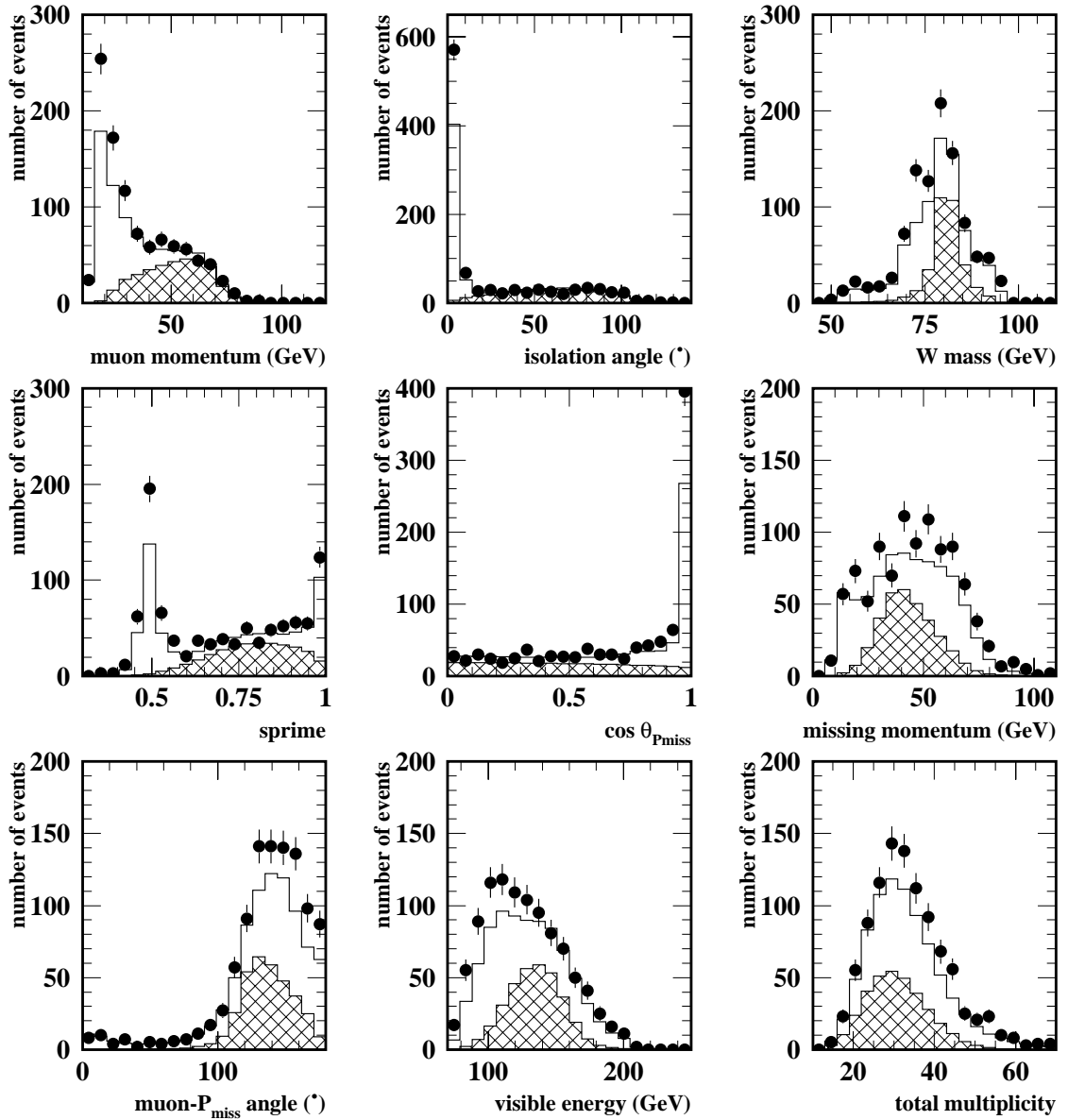


Figure A.3: Observables used to construct the discriminant variables for muons at 189 GeV.

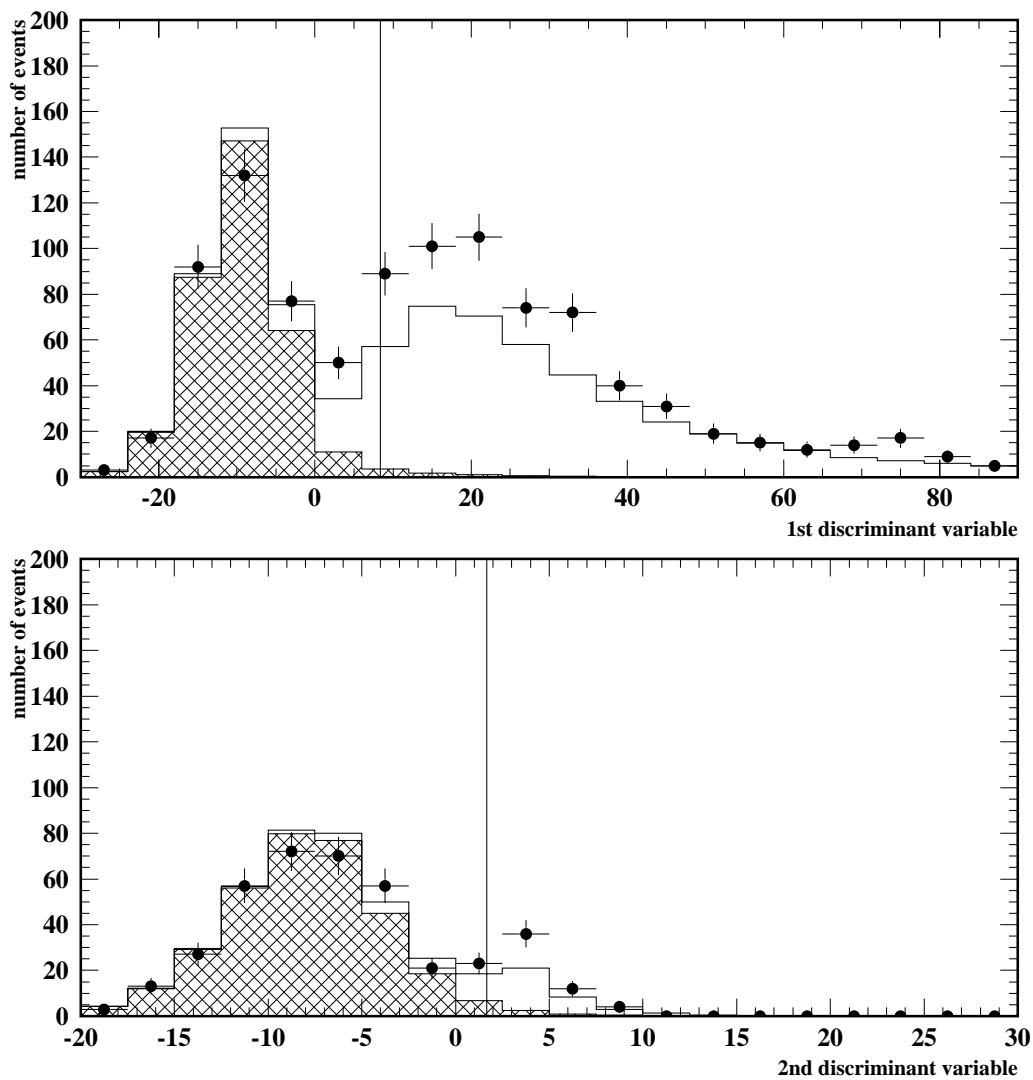


Figure A.4: First and second discriminant variables for muons at 189 GeV.

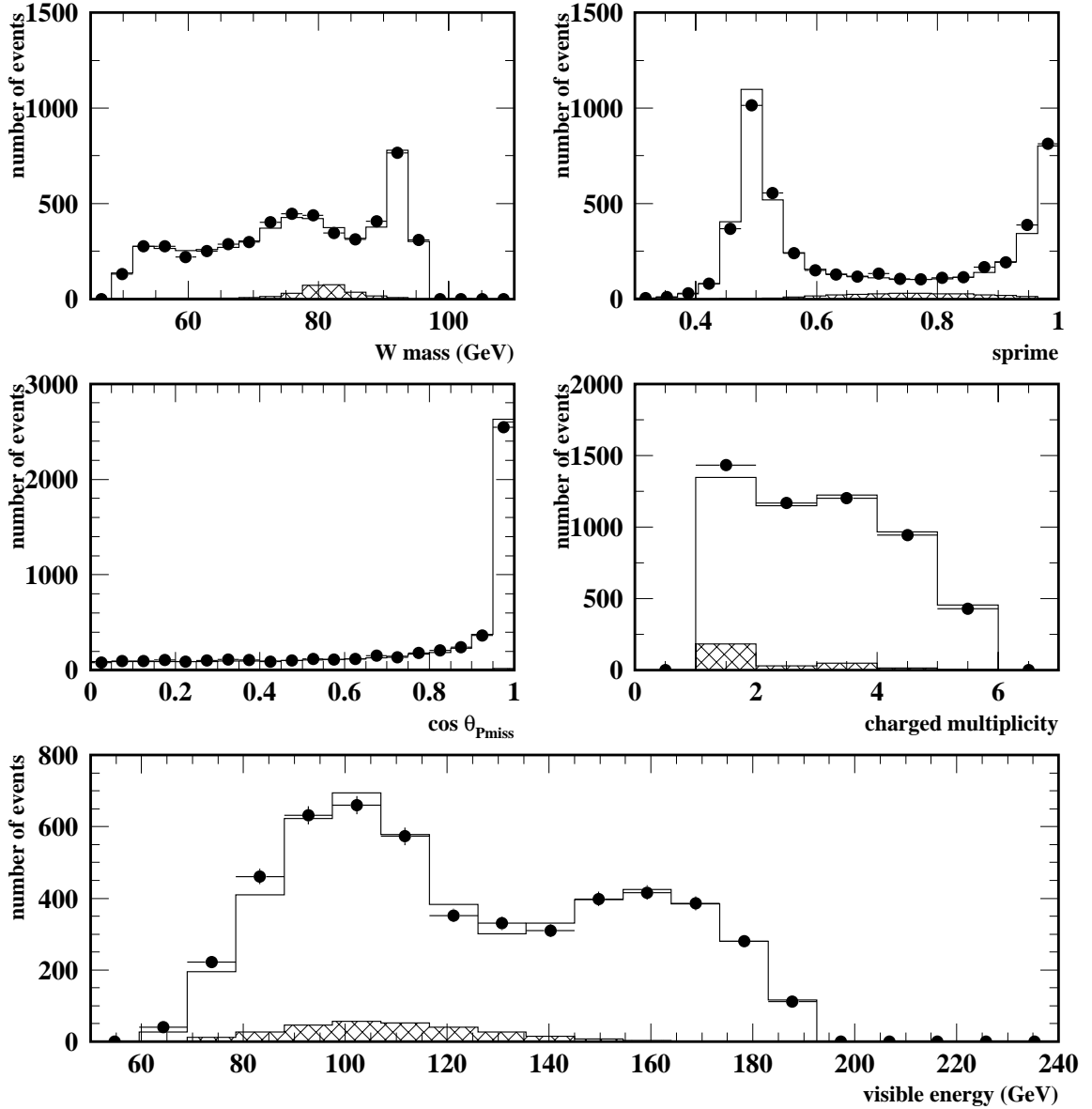


Figure A.5: Observables used to construct the discriminant variables for narrow-jet taus at 189 GeV.

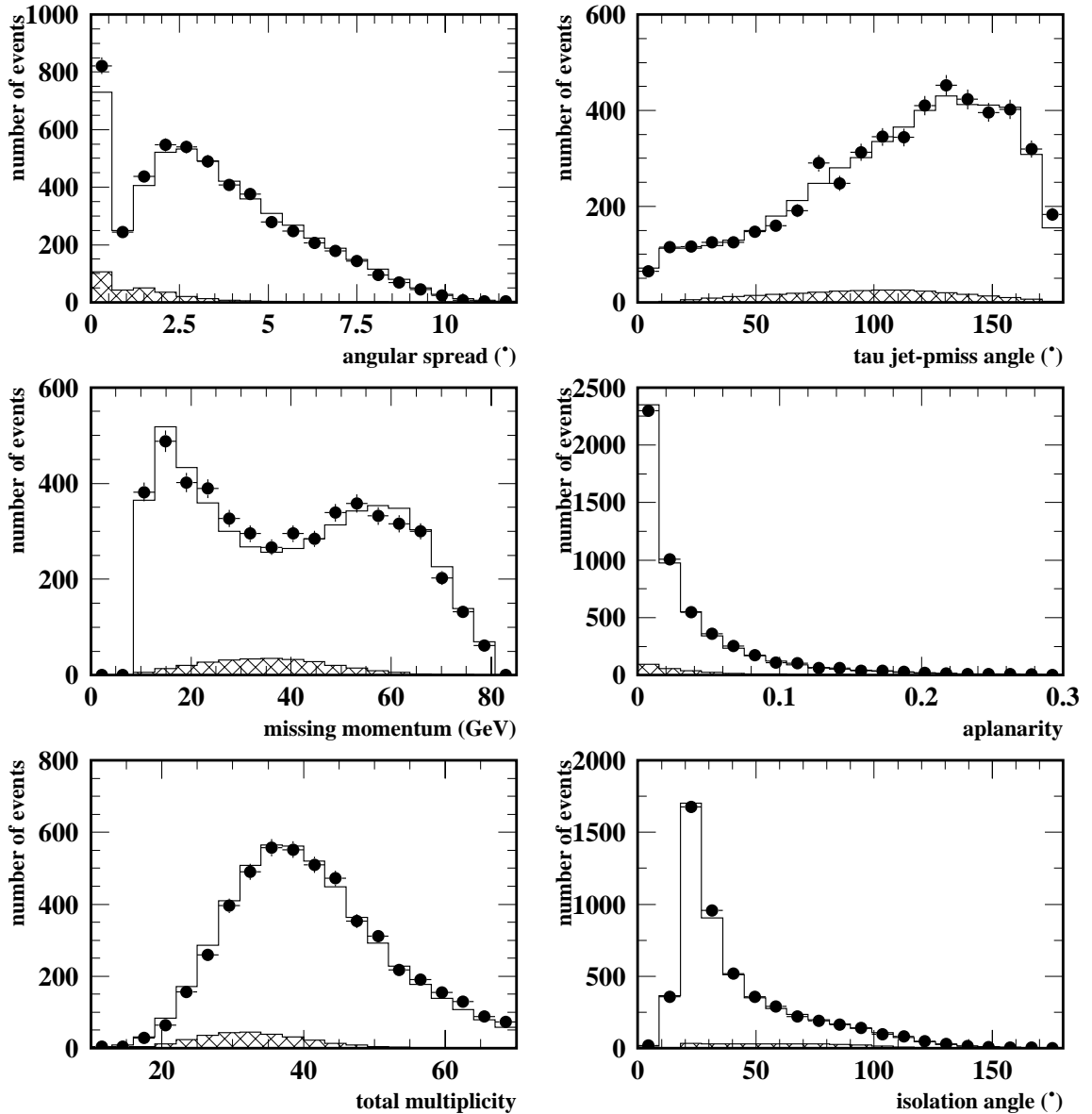


Figure A.6: Observables used to construct the discriminant variables for narrow-jet taus at 189 GeV.

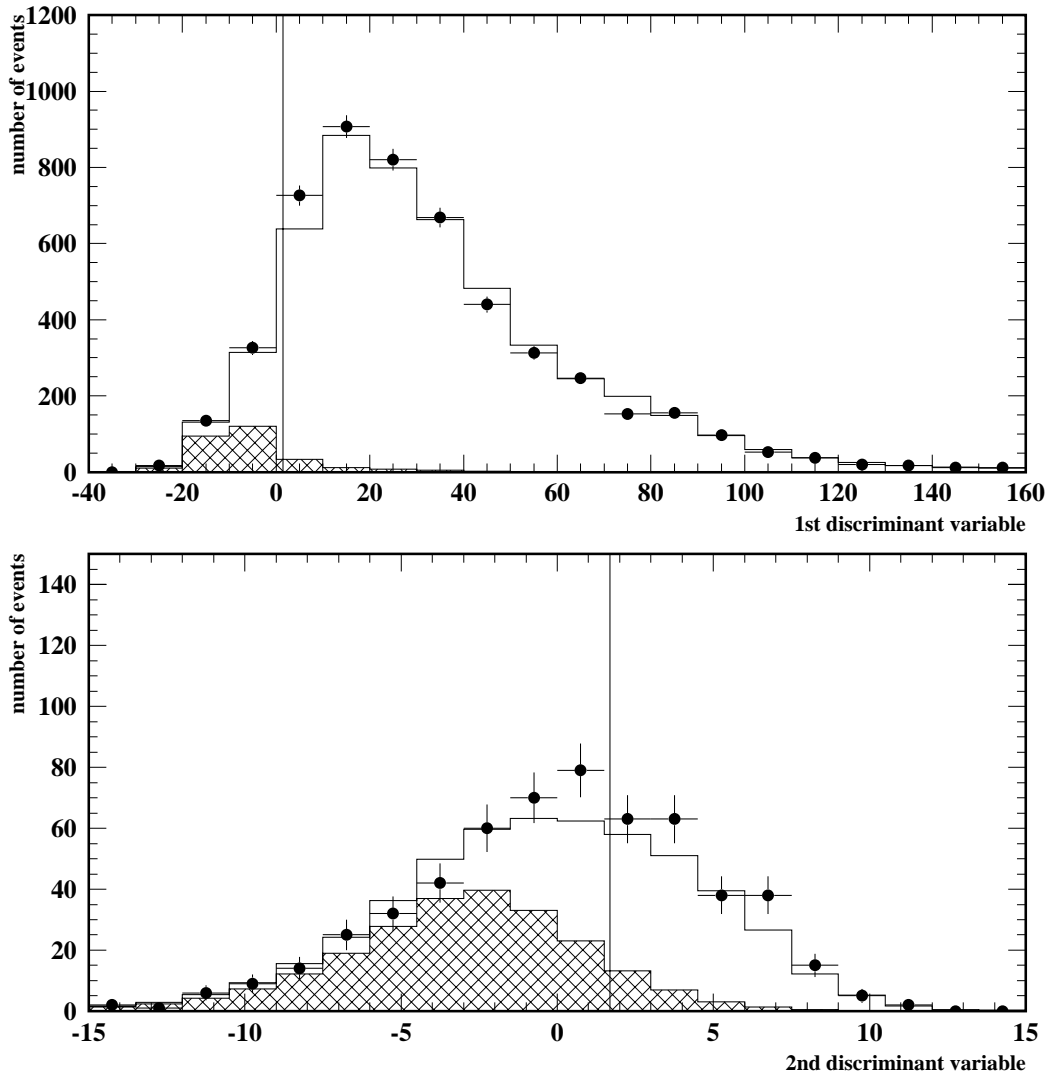


Figure A.7: *First and second discriminant variables for narrow-jet taus at 189 GeV.*

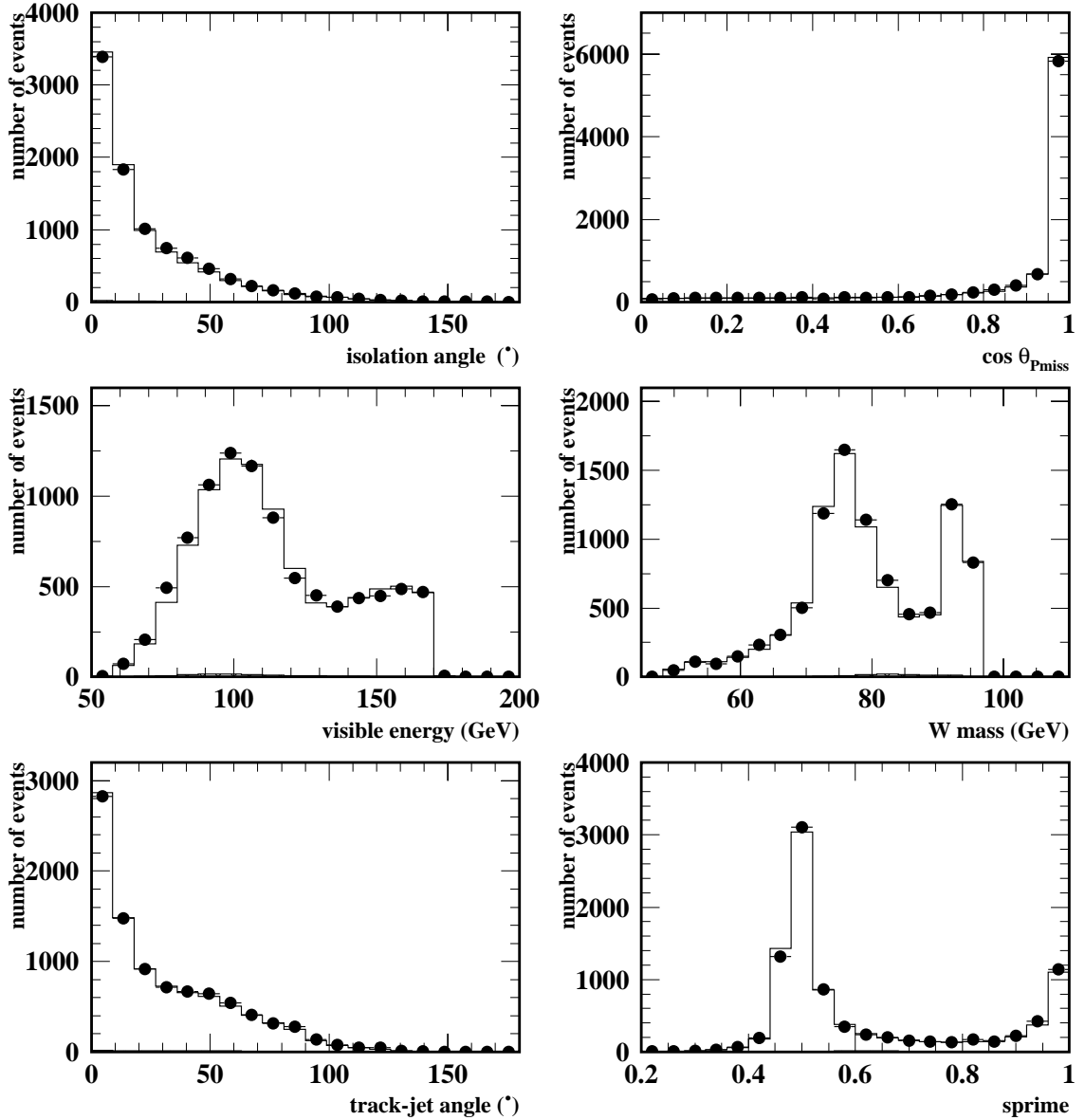


Figure A.8: Observables used to construct the discriminant variables for one-prong taus at 189 GeV.

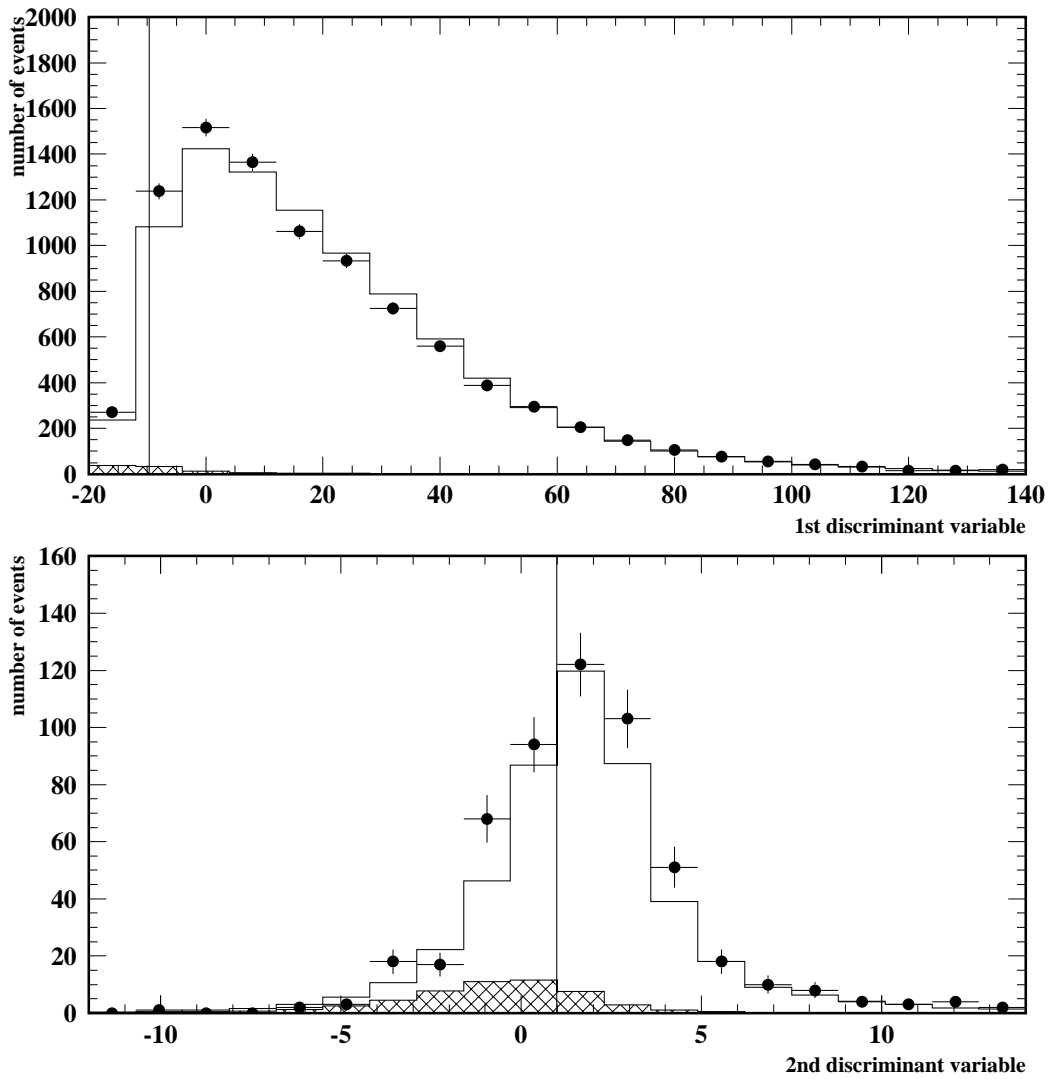


Figure A.9: *First and second discriminant variables for one-prong taus at 189 GeV.*

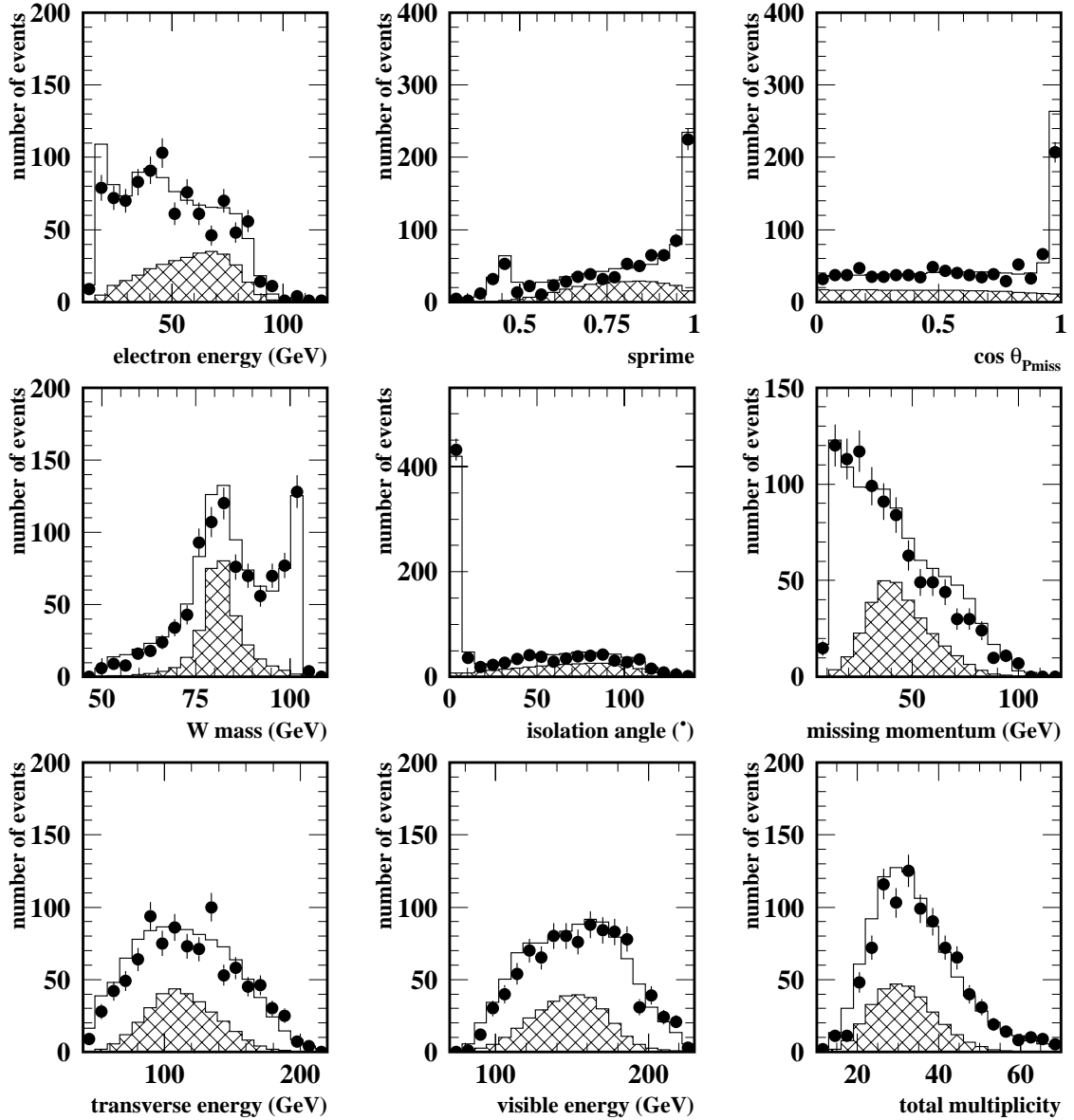


Figure A.10: *Observables used to construct the discriminant variables for electrons at 206 GeV.*

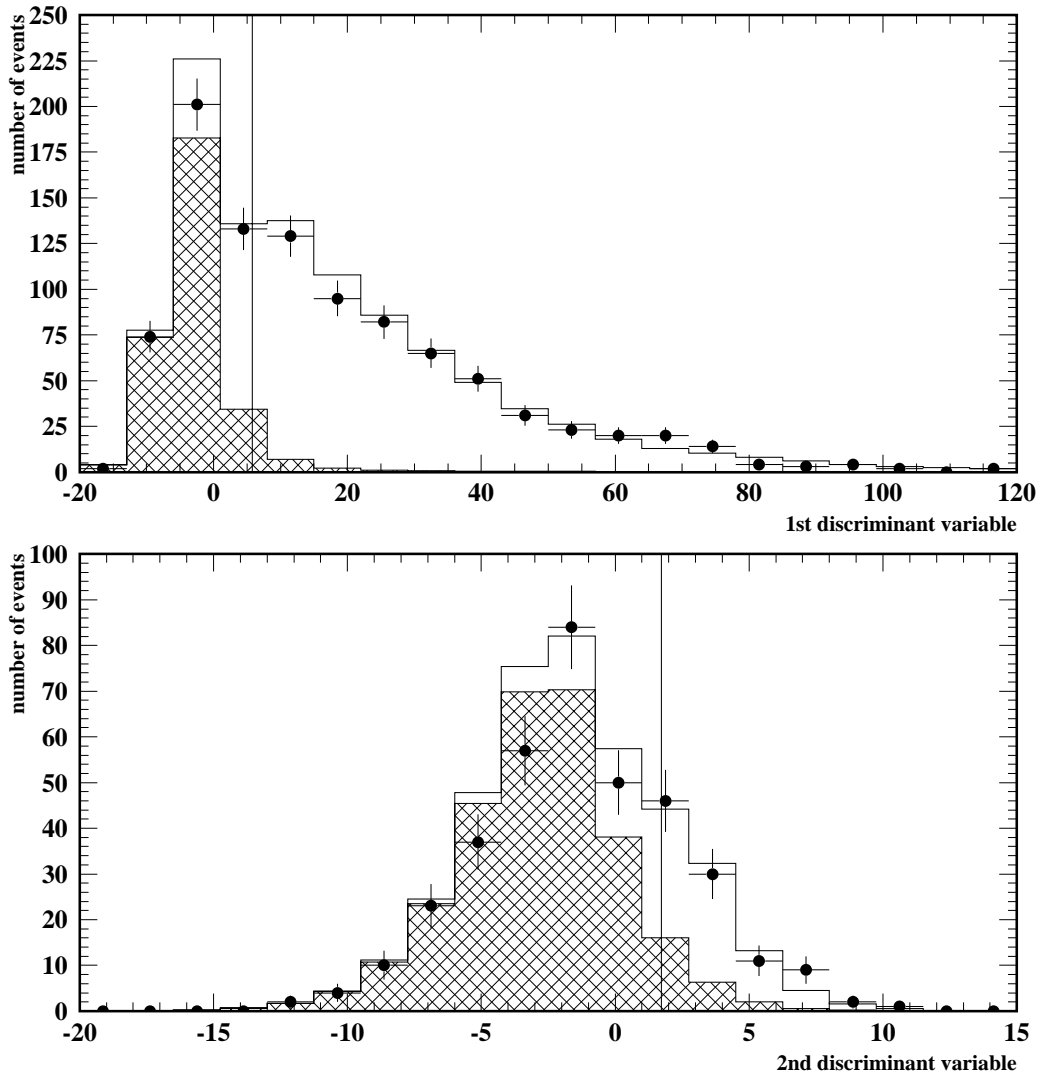


Figure A.11: *First and second discriminant variables for electrons at 206 GeV.*

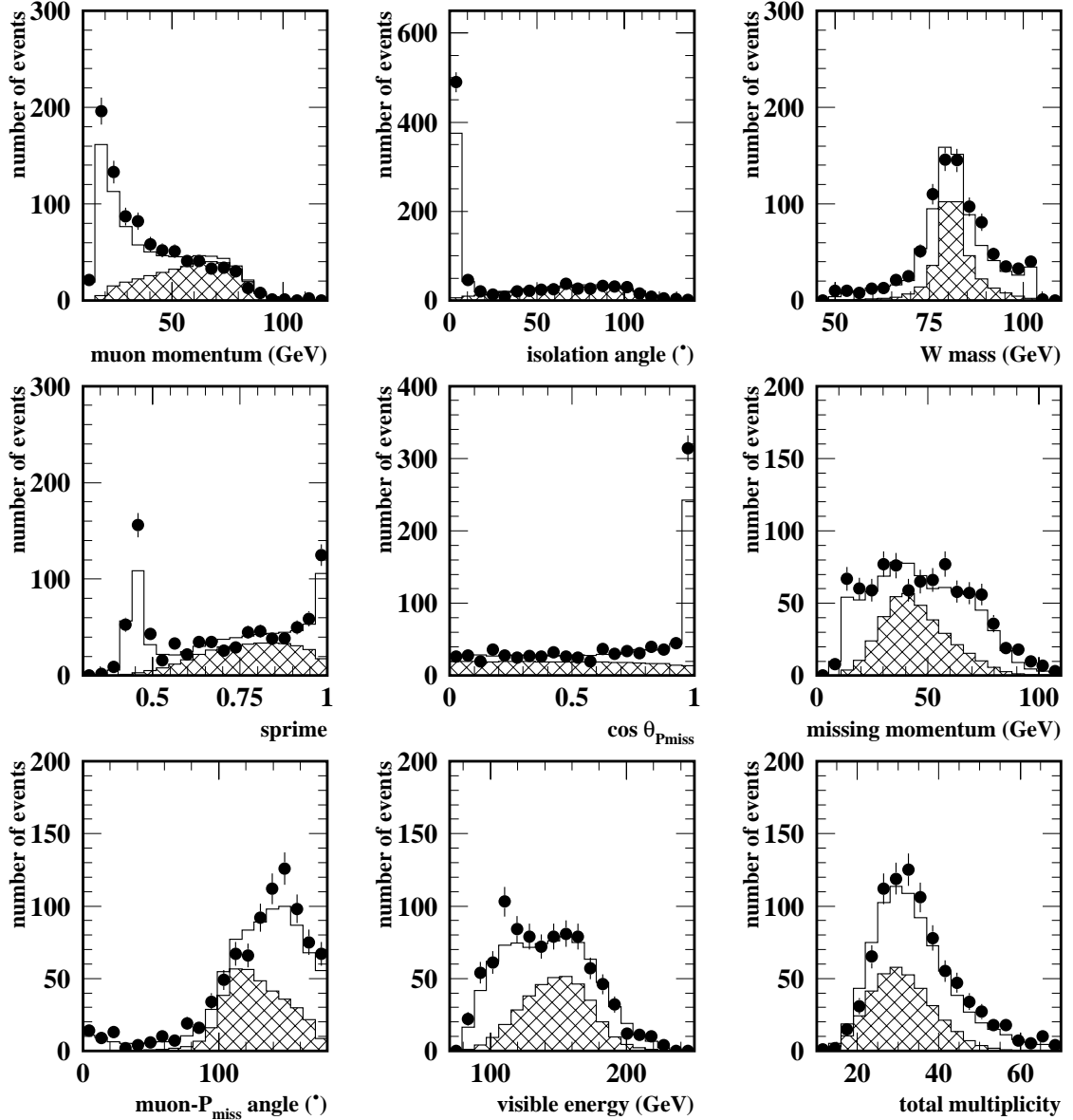


Figure A.12: *Observables used to construct the discriminant variables for muons at 206 GeV.*

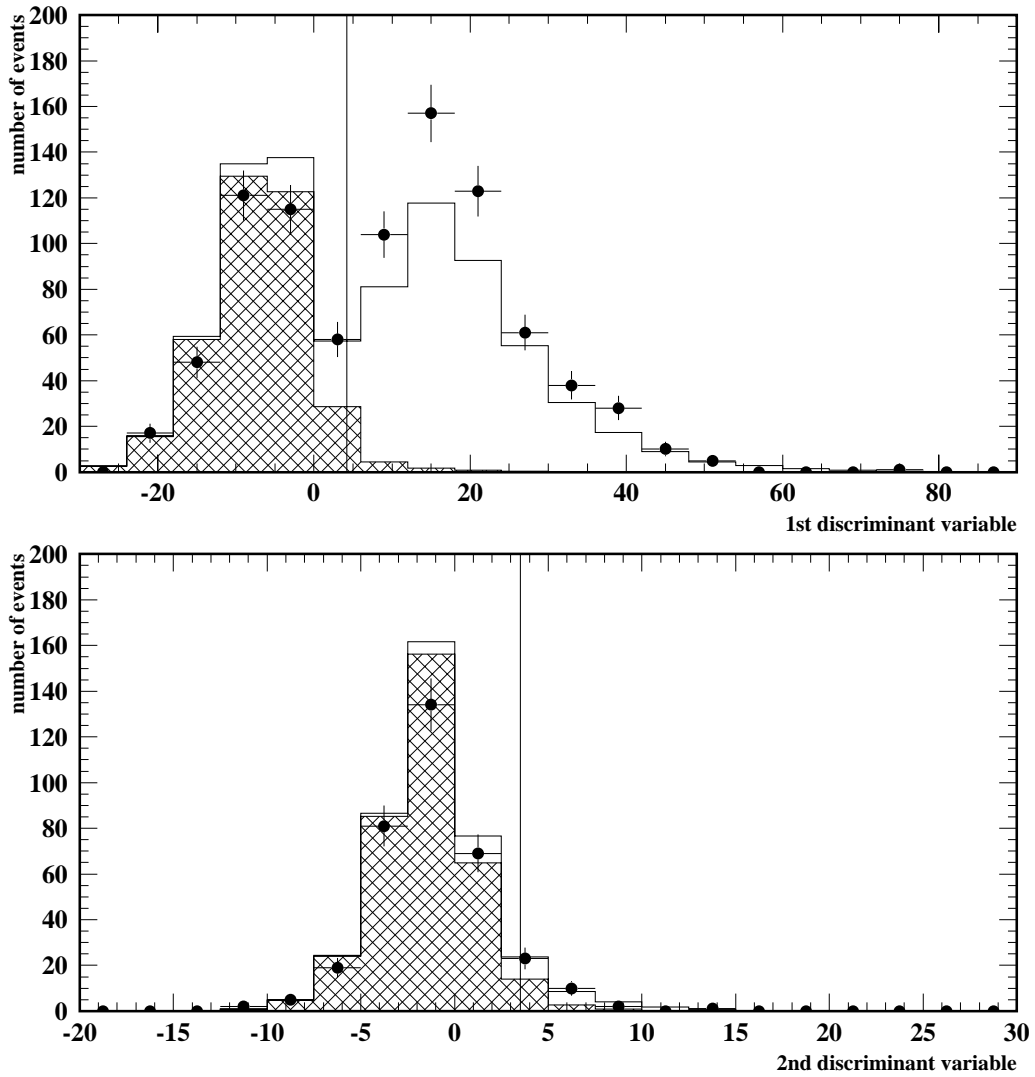


Figure A.13: *First and second discriminant variables for muons at 206 GeV.*

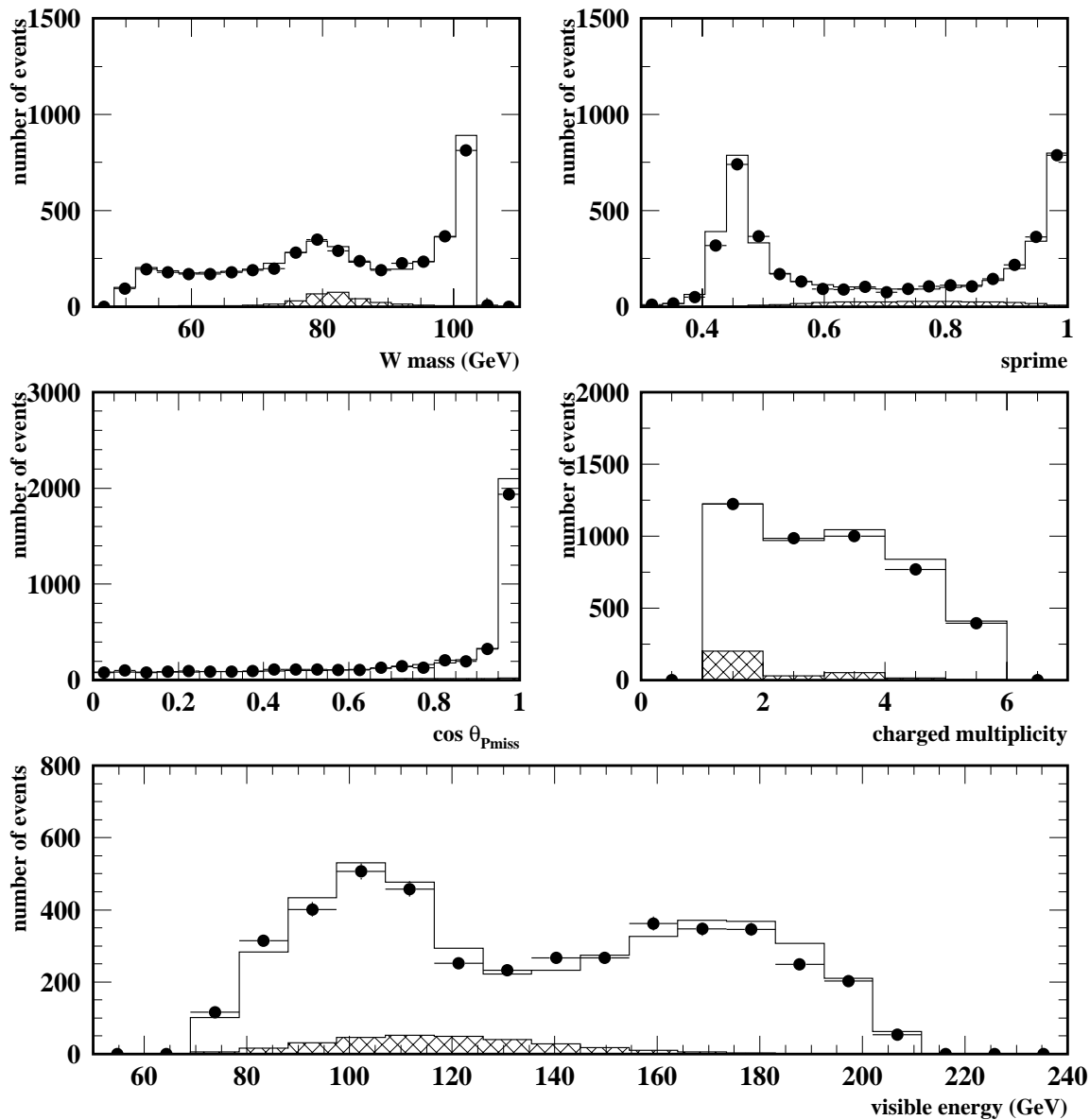


Figure A.14: *Observables used to construct the discriminant variables for narrow-jet taus at 206 GeV.*

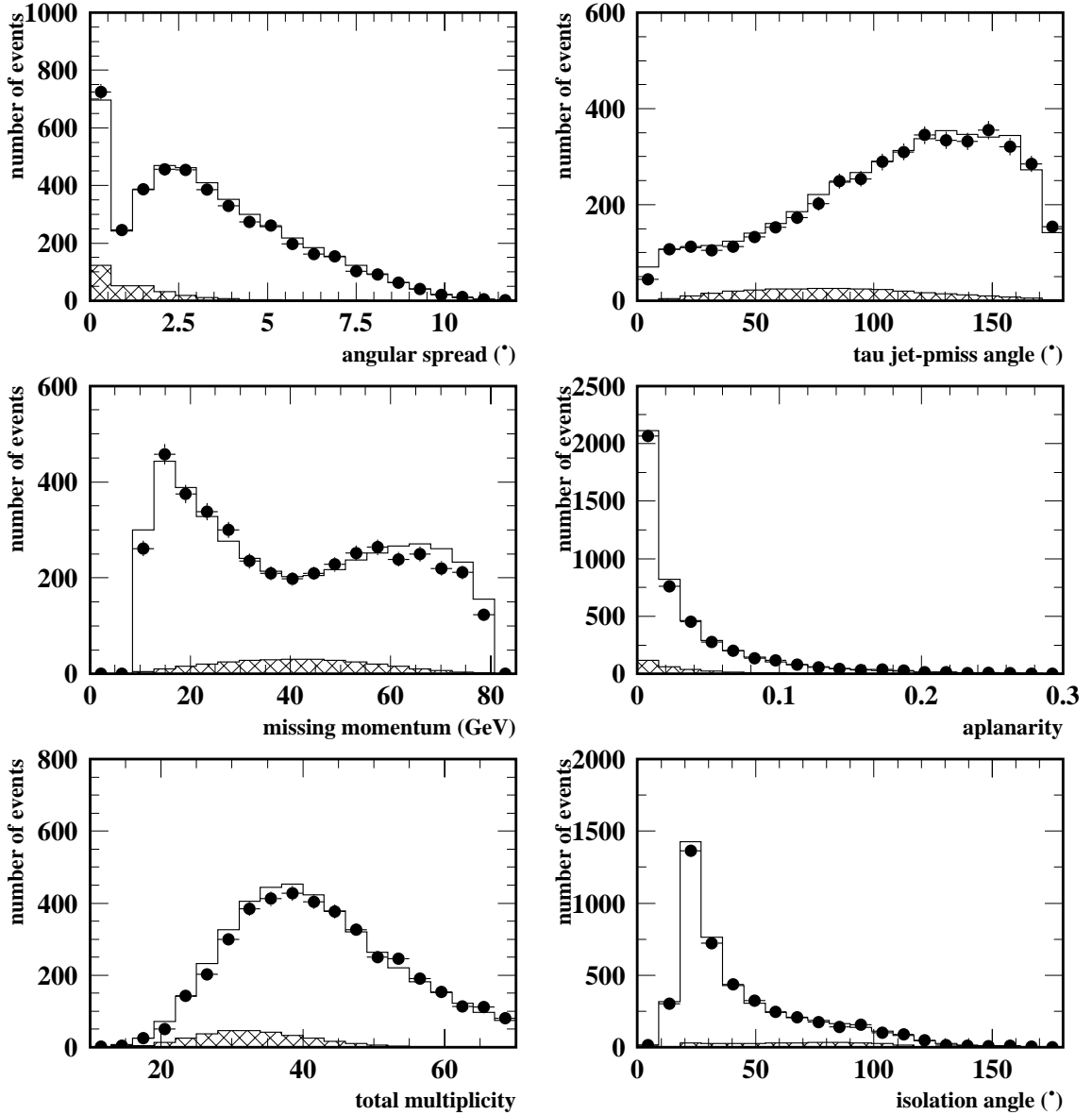


Figure A.15: *Observables used to construct the discriminant variables for narrow-jet taus at 206 GeV.*

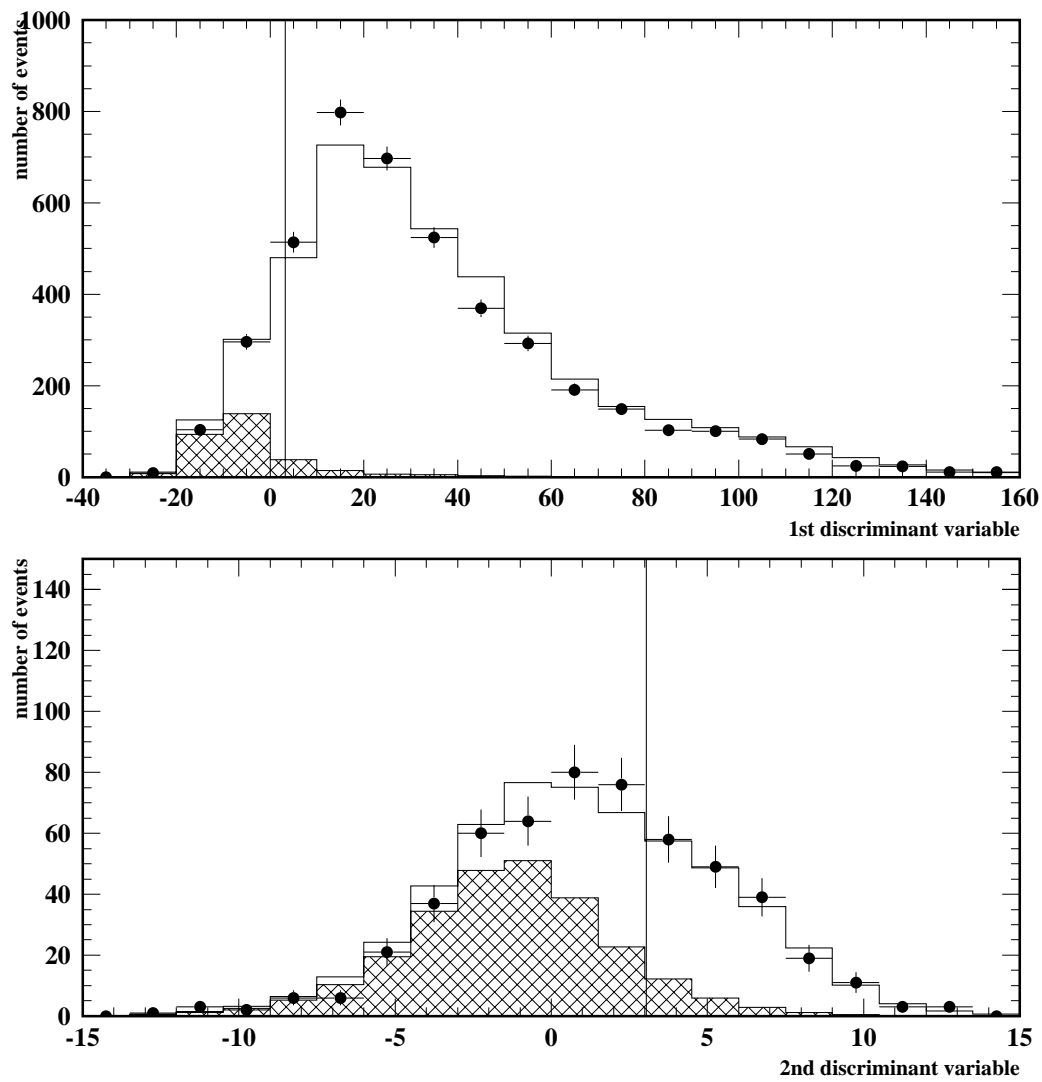


Figure A.16: *First and second discriminant variables for narrow-jet taus at 206 GeV.*

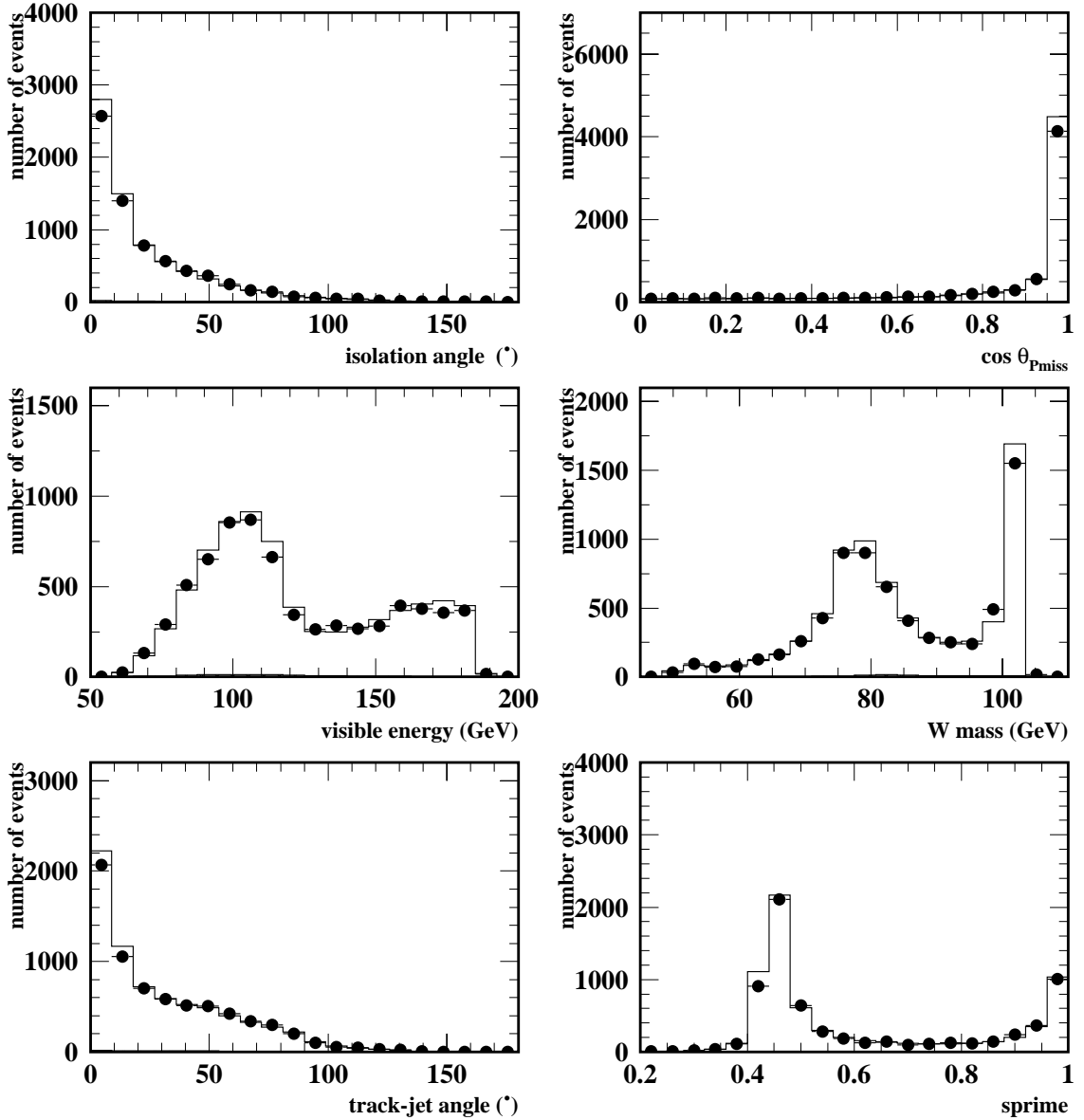


Figure A.17: *Observables used to construct the discriminant variables for one-prong taus at 206 GeV.*

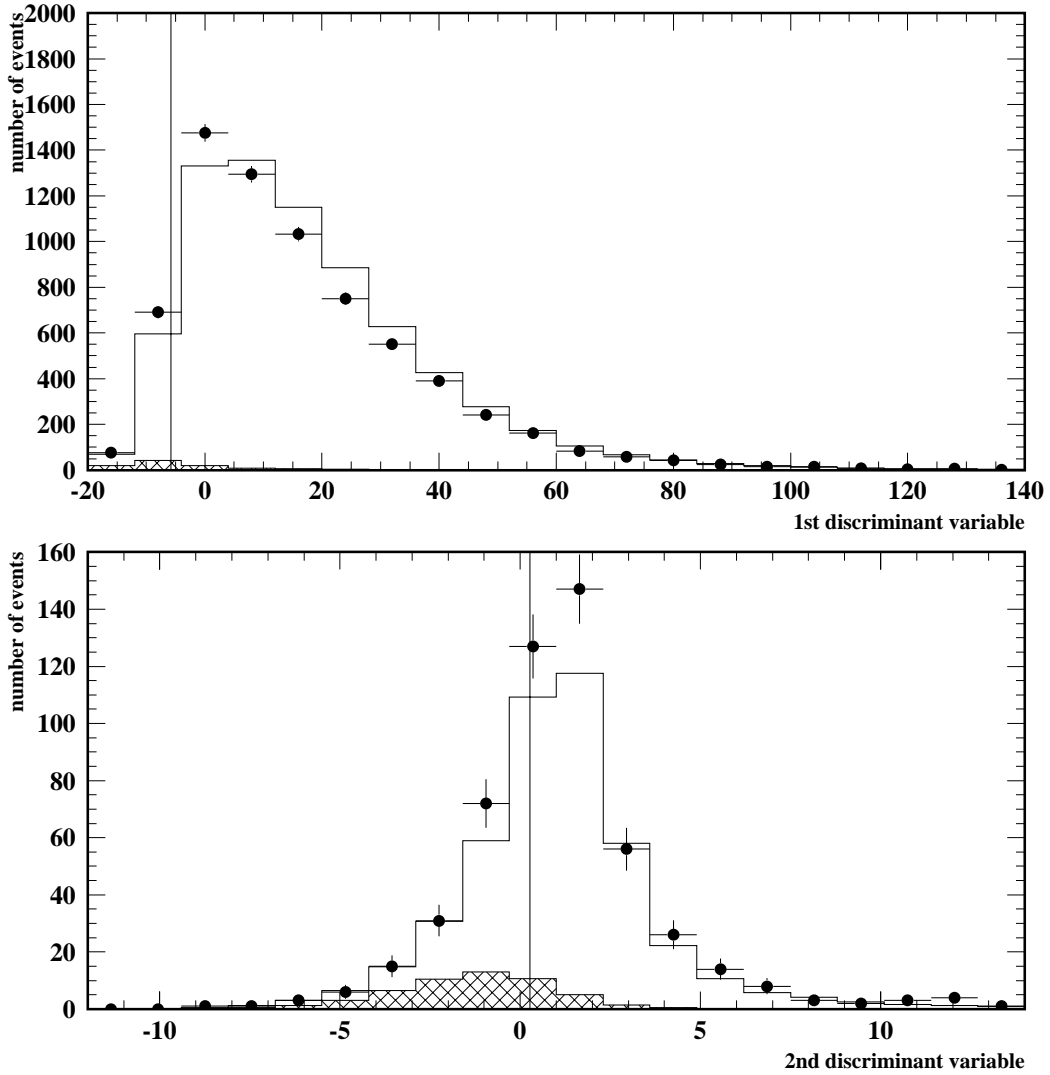


Figure A.18: *First and second discriminant variables for one-prong taus at 206 GeV.*



# Appendix B

## Event-by-event purity

The event-by-event purities were estimated as a function of the second discriminant variable for each selection channel. Figure B.1 shows the purities obtained for 200 GeV and B.2 for 206 GeV .

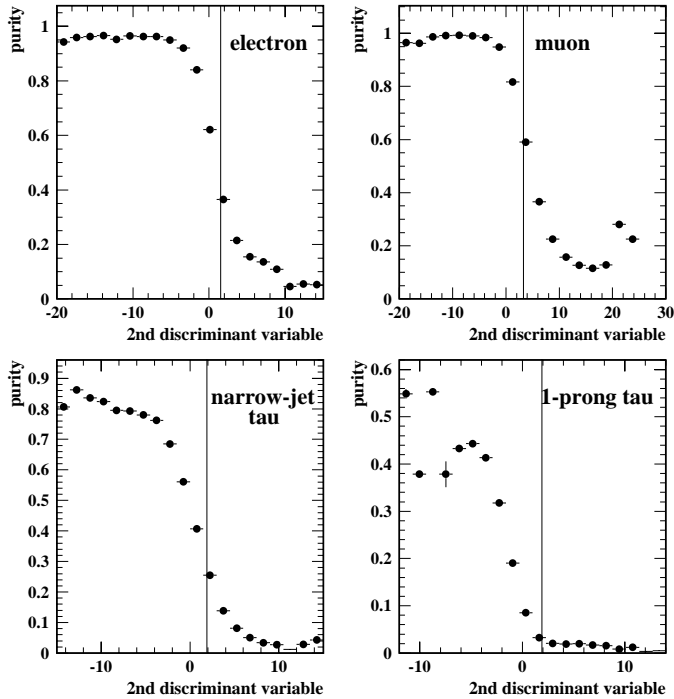


Figure B.1: *Event purity as a function of the second discriminant variable for each channel,  $q\bar{q}e\nu_e$ ,  $q\bar{q}\mu\nu_\mu$ ,  $q\bar{q}\tau\nu_\tau$  and  $q\bar{q}\tau_{1p}\nu_\tau$ , at 200 GeV. The vertical lines represent the cut on the discriminant variable in order to select events. Events to the left of the line are selected.*

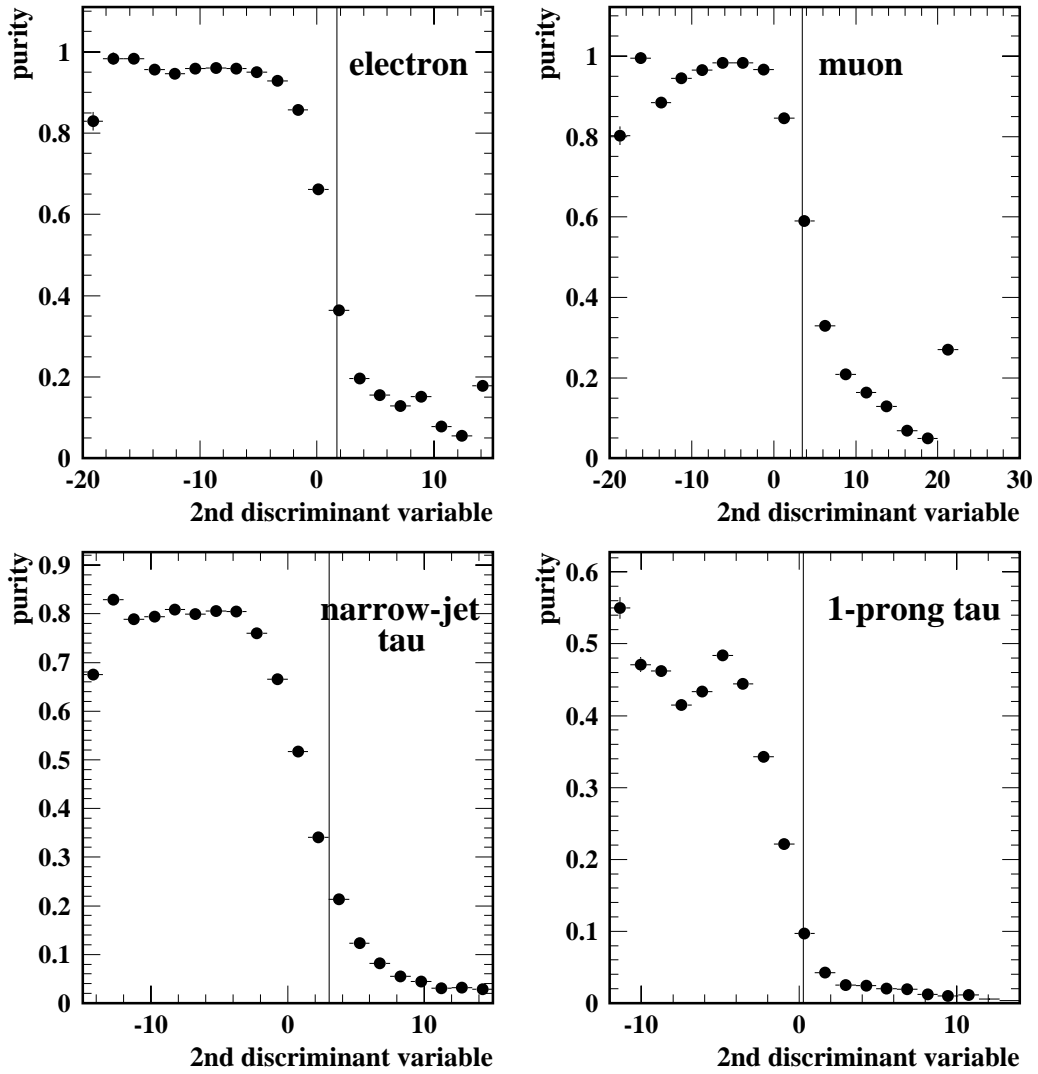


Figure B.2: Event-by-event purity calculated as a function of the second discriminant variable at 206 GeV.

# Bibliography

- [1] P. W. Higgs, *Broken symmetries, massless particles and gauge fields*, Phys. Lett. **12** (1964) 132, F. Englert and R. Brout, *Broken symmetry and the mass of Gauge vector mesons*, Phys. Rev. Lett. **13** (1964) 321, *ibid.* *Broken symmetries and the masses of gauge bosons*, **13** (1964) 508, P. W. Higgs, *Spontaneous symmetry breakdown without massless bosons*, Phys. Rev. **145** (1966) 1156.
- [2] S.L. Glashow, *Partial symmetries of weak interactions*, Nucl. Phys. **22** (1961) 579, S. Weinberg, *A model of leptons*, Phys. Rev. Lett. **19** (1967) 1264, A. Salam, in *Elementary particle theory*, ed. N. Svartholm, Almquist and Wiksell, Stockholm (1968) 367.
- [3] G. 't Hooft and M. J. G. Veltman, *Regularization and renormalization of gauge fields*, Nucl. Phys. **B44** (1972) 189–213.
- [4] F. J. Hasert *et al.* The Gargamelle Neutrino Collaboration, *Observation of neutrino-like interactions without muon or electron in the gargamelle neutrino experiment*, Phys. Lett. **B46** (1973) 138–140.
- [5] G. Arnison *et al.*, *Experimental observation of isolated large transverse energy electrons with associated missing energy at  $\sqrt{s} = 540$  GeV*, Phys. Lett. **B122** (1983) 103–116.
- [6] M. Banner *et al.*, *Observation of single isolated electrons of high transverse momentum in events with missing transverse energy at the CERN anti- $p$ - $p$  collider*, Phys. Lett. **B122** (1983) 476–485.
- [7] J. Alcaraz *et al.*, *A combination of preliminary electroweak measurements and constraints on the Standard Model*, (2006).
- [8] H. Burkhardt and B. Pietrzyk, *Low energy hadronic contribution to the QED vacuum polarization*, Phys. Rev. **D72** (2005) 057501.
- [9] F. Jegerlehner, *Physics of precision experiments with Zs*, Prog. Part. Nucl. Phys. **27** (1991) 1–76.

- [10] W. Beenakker, F. A. Berends, and A. P. Chapovsky, *Radiative corrections to pair production of unstable particles: Results for  $e^+e^- \rightarrow 4$  fermions*, Nucl. Phys. **B548** (1999) 3–59.
- [11] A. Denner, S. Dittmaier, M. Roth, and D. Wackerth, *Electroweak radiative corrections to  $e^+e^- \rightarrow WW \rightarrow 4$  fermions in double-pole approximation: The RACOONWW approach*, Nucl. Phys. **B587** (2000) 67–117.
- [12] S. Jadach, W. Placzek, M. Skrzypek, B. F. L. Ward, and Z. Was, *Precision predictions for (un)stable  $W^+W^-$  pair production at and beyond LEP2 energies*, Phys. Rev. **D65** (2002) 093010.
- [13] A. Denner, S. Dittmaier, M. Roth, and D. Wackerth,  *$O(\alpha)$  corrections to  $e^+e^- \rightarrow WW \rightarrow 4$  fermions( $+\gamma$ ): First numerical results from RACOONWW*, Phys. Lett. **B475** (2000) 127–134.
- [14] D. R. Yennie, S. C. Frautschi, and H. Suura, *The infrared divergence phenomena and high-energy processes*, Ann. Phys. **13** (1961) 379–452.
- [15] A. P. Chapovsky and V. A. Khoze, *Screened-Coulomb ansatz for the non-factorizable radiative corrections to the off-shell  $W^+W^-$  production*, Eur. Phys. J. **C9** (1999) 449–457.
- [16] E. Barberio and Z. Was, *PHOTOS: A universal Monte Carlo for QED radiative corrections. Version 2.0*, Comput. Phys. Commun. **79** (1994) 291–308.
- [17] T. Sjostrand, *High-energy physics event generation with PYTHIA 5.7 and JETSET 7.4*, Comput. Phys. Commun. **82** (1994) 74–90.
- [18] L. Lönnblad, *ARIADNE version 4: A program for simulation of QCD cascades implementing the Color Dipole Model*, Comput. Phys. Commun. **71** (1992) 15.
- [19] G. Marchesini *et al.*, *HERWIG version 5.9: A Monte Carlo event generator*, (1996).
- [20] T. Sjostrand and V. A. Khoze, *On color rearrangement in hadronic  $W^+W^-$  events*, Z. Phys. **C62** (1994) 281–310.
- [21] J. Abdallah *et al.*, *Investigation of Colour Reconnection in WW events with the DELPHI detector at LEP-2*, Eur. Phys. J. **C51** (2007) 249–269.
- [22] P. Abreu *et al.*, *Measurement of the mass and width of the W boson in  $e^+e^-$  collisions at  $\sqrt{s} = 161 - 209$  GeV*, CERN-PH-EP 2007-026.
- [23] L. Lönnblad, *Reconnecting colored dipoles*, Z. Phys. **C70** (1996) 107–114.

- [24] L. Lönnblad, *Modeling Bose-Einstein correlations at LEP2*, Prepared for 8th International Workshop on Multiparticle Production: Correlations and Fluctuations '98 (CF 98) Matrahaza Hungary 14-21 Jun 1998.
- [25] J. Abdallah *et al.*, *Bose-Einstein correlations in  $W^+W^-$  events at LEP2*, Eur. Phys. J. **C44** (2005) 161–174.
- [26] E. Accomando, A. Ballestrero, and E. Maina, *WPHACT 2.0: A fully massive Monte Carlo generator for four fermion physics at  $e^+e^-$  colliders*, Comput. Phys. Commun. **150** (2003) 166–196.
- [27] S. Jadach, Z. Was, R. Decker, and J. H. Kuhn, *The tau decay library TAUOLA: Version 2.4*, Comput. Phys. Commun. **76** (1993) 361–380.
- [28] S. Jadach, B. F. L. Ward, and Z. Was, *The precision Monte Carlo event generator KK for two-fermion final states in  $e^+e^-$  collisions*, Comput. Phys. Commun. **130** (2000) 260–325.
- [29] A. Ballestrero, R. Chierici, F. Cossutti, and E. Migliore, *Four-fermion simulation at LEP2 in DELPHI*, Comput. Phys. Commun. **152** (2003) 175–190.
- [30] ALEPH Collaboration, *A detector for electron-positron annihilations at LEP*, Nucl. Inst. Meth. **A 294** (1990) 121.
- [31] DELPHI Collaboration, *The DELPHI detector at LEP*, Nucl. Inst. Meth. **A 303** (1991) 233.
- [32] L3 Collaboration, *The construction of the L3 experiment*, Nucl. Inst. Meth. **A 289** (1990) 35.
- [33] OPAL Collaboration, *The OPAL detector at LEP*, Nucl. Inst. Meth. **A 305** (1991) 275.
- [34] Vol.I LEP Design Report, *The LEP injector chain*, Preprint CERN-LEP/TH/83-29, CERN, 1983.
- [35] R. Assmann *et al.*, *Calibration of centre-of-mass energies at LEP2 for a precise measurement of the W boson mass*, Eur. Phys. J. **C39** (2005) 253–292.
- [36] J. Abdallah *et al.*, *A determination of the centre-of-mass energy at LEP2 using radiative 2-fermion events*, Eur. Phys. J. **C46** (2006) 295–305.
- [37] R. Barate *et al.*, *Determination of the LEP centre-of-mass energy from  $Z\gamma$  events*, Phys. Lett. **B464** (1999) 339–349.
- [38] P. Achard *et al.*, *Measurement of the Z-boson mass using  $e^+e^- \rightarrow Z\gamma$  events at centre-of-mass energies above the Z pole*, Phys. Lett. **B585** (2004) 42–52.

- [39] G. Abbiendi *et al.*, *Determination of the LEP beam energy using radiative fermion-pair events*, Phys. Lett. **B604** (2004) 31–47.
- [40] P. A. Aarnio *et al.*, *The DELPHI detector at LEP*, Nucl. Instrum. Meth. **A303** (1991) 233–276.
- [41] P. Abreu *et al.*, *Performance of the DELPHI detector*, Nucl. Instrum. Meth. **A378** (1996) 57–100.
- [42] V. Perevozchikov and N. Smirnov, *PHDST package description V.3 VZD - Viewer of Zebra Data for DELPHI user's manual*, DELPHI note **DELPHI 92-118 PROG 189** (1994).
- [43] F. Cossutti, *Improvements to Skelana for version 2.0*, DELPHI note **DELPHI 99-175 PROG 239** (1999).
- [44] R. Chierici and C. Parkes and A. Tonazzo, *WWANA a standard package for W analysis*, DELPHI note **DELPHI 96-128 PROG 218** (1996).
- [45] F. Cossutti, A. Tonazzo, and F. Mazzucato, *REMCLU: a package for the Reconstruction of Electromagnetic CLusters at LEP200*, DELPHI note **DELPHI 2000-164 PROG 242** (2000).
- [46] M. Feindt, C. Kreuter, and O. Podobrin, *ELEPHANT reference manual*, DELPHI note **DELPHI 96-82 PROG 217** (1996).
- [47] L. De Boeck and G.R. Wilkinson, *MUFLAG - a framework for muon identification*, DELPHI note **DELPHI 93-14 PHYS 263** (1993).
- [48] J. Abdallah *et al.*, *Measurement of the W pair production cross-section and W branching ratios in  $e^+e^-$  collisions at  $\sqrt{s} = 161$  GeV to 209 GeV*, Eur. Phys. J. **C34** (2004) 127–144.
- [49] D. Jeans, *A Study of  $e^+e^- \rightarrow W^+W^-$  at centre-of-mass energies between 161 GeV and 209 GeV*, Ph.D. thesis, Oxford University, 2001.
- [50] G. Cowan, *Statistical Data Analysis*, Oxford University Press (1998).
- [51] D. Jeans, *A discussion of discriminant techniques*, DELPHI note **DELPHI 2001-135 TRACK 97** (2001).
- [52] P. Abreu *et al.*, *The estimation of the effective centre of mass energy in  $q\bar{q}\gamma$  events from DELPHI*, Nucl. Instrum. Meth. **A427** (1999) 487–494.
- [53] M. Mulders, *Direct measurement of the W boson mass in  $e^+e^-$  collisions at LEP*, Ph.D. thesis, NIKHEF, 2001.

- 
- [54] S. Catani, Yuri L. Dokshitzer, M. Olsson, G. Turnock, and B. R. Webber, *New clustering algorithm for multi - jet cross-sections in  $e^+ e^-$  annihilation*, Phys. Lett. **B269** (1991) 432–438.
- [55] T. Sjostrand, *PYTHIA 5.7 and JETSET 7.4: Physics and manual*, (1995).
- [56] A. Behrmann and P.J. Holt, *Muon measurement and muon chamber efficiency corrections for LEP II*, DELPHI note **DELPHI 2002-017 PHYS 918** (2002).
- [57] P. Abreu *et al.*, *Improved measurements of cross-sections and asymmetries at the Z resonance*, Nucl. Phys. **B418** (1994) 403–427.
- [58] G. Borissov, *Combined b-tagging*, DELPHI note **DELPHI 1997-94 PHYS 716** (1997).
- [59] I. van Vulpen, *private communication*.
- [60] F. Cossutti, *Electroweak corrections uncertainty on the W mass measurement at LEP*, Eur. Phys. J. **C44** (2005) 383–393.
- [61] S. Jadach, W. Placzek, M. Skrzypek, B. F. L. Ward, and Z. Was, *On theoretical uncertainties of the W boson mass measurement at LEP2*, Phys. Lett. **B523** (2001) 117–126.
- [62] S. Jadach, W. Placzek, M. Skrzypek, B. F. L. Ward, and Z. Was, *Exact  $O(\alpha)$  gauge invariant YFS exponentiated Monte Carlo for (un)stable  $W^+ W^-$  production at and beyond LEP2 energies*, Phys. Lett. **B417** (1998) 326–336.
- [63] <http://lepewwg.web.cern.ch/LEPEWWG/Welcome.html>.
- [64] *TESLA Technical Design Report part III*, Physics at an  $e^+e^-$  Linear Collider. March 2001.



# Summary

The W boson is the charged mediator of the weak interaction which is one of the four kinds of interactions present in nature. The W boson is, for particles standards, a heavy particle, it weighs around  $1.43 \cdot 10^{-25}$  kg. In addition, it lives for a very short time before it decays into other particles, its lifetime is only  $3.2 \cdot 10^{-25}$  seconds. These are the reasons why one does not observe W bosons in daily life. The W boson was discovered in 1983 together with its neutral counterpart, the Z boson, at the UA1 and UA2 experiments at CERN. Their properties were not accurately known experimentally until the start of LEP in 1989.

LEP was an  $e^+e^-$  collider built at CERN near Geneva. In the first phase of the LEP program, which lasted from 1989 until the end of 1995, electrons and positrons were accelerated and collided at a centre-of-mass energy sufficient to produce a Z boson at rest. Using the data collected during this phase the properties of the Z boson were measured with unprecedented accuracy ( $2 \cdot 10^{-5}$  relative uncertainty on the Z mass and around  $1 \cdot 10^{-3}$  on the (partial) widths). In 1996, after an upgrade of the LEP machine, the second phase of the program began. During this phase, known as LEP-2, the centre-of-mass energy was increased to the threshold of W-pair production and above that in the following years. Logically, during the LEP-2 phase the properties of the W boson were extensively studied by the LEP community.

The subject of this thesis is the direct measurement of the mass of the W boson in semi-leptonic events. In this kind of events one of the two W bosons decays into a quark and an anti-quark and the other decays into a lepton and its corresponding neutrino. This measurement was performed using the data collected by the DELPHI experiment at LEP.

The data analysed in this thesis was collected at seven different centre-of-mass energies ranging from 183 GeV to 206 GeV. The events were selected using an Iterative Discriminant Analysis, which builds a discriminant variable using a set of observables in order to distinguish between signal and background. The events which passed this selection were analysed using the Ideogram method. In this method a likelihood curve was constructed for every event and per event even for two different hypotheses. The method aims to include the maximum obtainable amount of information in the event in order to minimise the statistical uncertainty. After extracting a W mass value and its statistical uncertainty a thorough analysis of the possible sources of systematic uncertainties was performed. A total of 14 systematic uncertainties were evaluated. The error due to the uncertainty in the knowledge of the fragmentation process was estimated in a model independent way using the Mixed

Lorentz Boosted Z method. This method was first developed for the WW fully hadronic channel but was used in semi-leptonic events for the first time in this thesis.

The final result for the W mass measurement in the semi-leptonic channel using a data sample with an integrated luminosity of  $641 \text{ pb}^{-1}$  was found to be

$$m_W = 80.455 \pm 0.071(\text{stat.}) \pm 0.029(\text{syst.}) \pm 0.009(\text{LEP}) \text{ GeV.}$$

This result is in very good agreement with the current world average

$$m_W = 80.398 \pm 0.025 \text{ GeV.}$$

One can expect the uncertainties on the current world average to still decrease considerably in future. With contributions from the Tevatron, the LHC and from the next linear collider the error in the W mass might reach an impressive 6 MeV.

# Samenvatting

Het W is de geladen drager van de zwakke interactie, één van de vier soorten interacties die er bestaan. Het W boson is, voor een elementair deeltje, relatief zwaar en weegt ongeveer  $1.43 \cdot 10^{-25}$  kg. Daarbij komt dat het maar voor een zeer korte tijd bestaat voordat het vervalt in andere deeltjes, zijn levensduur is slechts zo'n  $3.2 \cdot 10^{-25}$  seconden. Door deze twee oorzaken zien we geen W bosonen in ons dagelijks leven. Het twee boson is in 1983 ontdekt tegelijk met zijn neutrale tegenhanger, het Z boson, door de UA1 en UA2 experimenten aan het CERN. Hun eigenschappen waren niet nauwkeurig gemeten tot de start van LEP in 1989.

LEP was een  $e^+e^-$  versneller gebouwd op het CERN in de buurt van Genève. In de eerste fase van het LEP programma, wat van 1989 tot het einde van 1995 duurde, werden elektronen en positronen versneld en tot botsing gebracht op zwaartepuntsenergie die voldoende waren om Z bosonen te produceren. Gebruikmakend van de gegevens die in deze fase werden verzameld zijn de eigenschappen van het Z boson gemeten met ongekende precisie ( $2 \cdot 10^{-5}$  relatieve onzekerheid op de Z massa en rond de  $1 \cdot 10^{-3}$  op de breedte). In 1996 begon de tweede fase van het programma, bekend als LEP-2. In deze fase werd de zwaartepuntsenergie verhoogd tot de drempel voor de productie van W-paren en in latere jaren tot ruim daarboven. Logischerwijs werden in deze tijd de eigenschappen van het W boson uitgebreid bestudeerd door de LEP-gemeenschap.

Het onderwerp van dit proefschrift is de directe meting van de massa van het W boson in semi-leptonische gebeurtenissen. In dit type gebeurtenissen vervalt één van de twee W bosonen in een quark en een anti-quark en de andere vervalt in een lepton en het corresponderende neutrino. Deze meting werd uitgevoerd gebruikmakend van de gegevens verzameld door het DELPHI experiment aan LEP.

Deze gegevens zijn verzameld op zeven verschillende zwaartepuntsenergiën variërend van 183 GeV tot 206 GeV. De gebeurtenissen werden geselecteerd gebruikmakend van een Iteratieve Onderscheidings Analyse. In deze analyse wordt op basis van een aantal waarneembare grootheden een variabele geconstrueerd om achtergrond en signaal van elkaar te kunnen onderscheiden. De gebeurtenissen die op deze wijze werden geselecteerd zijn vervolgens geanalyseerd met behulp van de Ideogram methode. In deze methode werd per gebeurtenis voor verschillende hypothesen van waarschijnlijkheidscurve geconstrueerd. Op deze wijze is getracht de grootst mogelijke hoeveelheid informatie in de gebeurtenis te gebruiken om de uiteindelijke statistische onnauwkeurigheid te minimaliseren. Naast het

bepalen van een waarde voor de W massa en de bijbehorende statistische onnauwkeurigheid is een uitgebreide analyse gemaakt van de mogelijke systematische onnauwkeurigheden. In totaal zijn 14 systematische onnauwkeurigheden geëvalueerd. De onnauwkeurigheid tengevolge van de gebrekkige kennis van het fragmentatieproces is geschat op een modelonafhankelijke wijze met de hulp van de Mixed Lorentz Boosted Z methode. Deze methode is oorspronkelijk ontwikkeld voor gebeurtenissen waarin beide W bosonen vervallen naar een quark en een anti-quark en is in dit proefschrift voor het eerst toegepast voor semi-leptonische gebeurtenissen.

Gebruikmakend van een gegevensset met een geïntegreerde luminositeit van  $641 \text{ pb}^{-1}$  is het uiteindelijke resultaat voor de meting van de W massa in het semi-leptonische vervalkanaal bepaald op

$$m_W = 80.455 \pm 0.071(\text{stat.}) \pm 0.029(\text{syst.}) \pm 0.009(\text{LEP}) \text{ GeV.}$$

Dit resultaat is in goede overeenstemming met het huidige wereldwijde gemiddelde

$$m_W = 80.398 \pm 0.025 \text{ GeV.}$$

Het ligt in de lijn der verwachtingen dat de onnauwkeurigheden van het wereldwijde gemiddelde in de toekomst nog aanzienlijk zullen afnemen. Met bijdragen van het Tevatron, de LHC en de next linear collider zou de precisie van de meting uiteindelijk een indrukwekkende 6 MeV kunnen bedragen.

# Acknowledgements

I cannot really believe I am actually writing the acknowledgements of my thesis, finally! When you take so long to finish a PhD, 7 years, 10 months and a few days, the list of people to thank also becomes longer. But I consider myself fortunate to have had some many people help me getting to the finish line.

The very first person I want to thank is my supervisor Jan Timmermans. Thanks to Jan I could start my PhD at Nikhef, since he was the one who hired me. But also thanks to Jan I could finish it. Jan, thank you so much for stepping in again at the last year and half of my PhD. Thanks for the very useful and thorough discussions and for the very careful reading of my thesis, I am very grateful for your timmermansoog. Second on my list, but certainly not less important is my promotor Nicolo de Groot. Nicolo became my promotor about a year and half before I finished writing my thesis. Nicolo, thanks for believing I could get this to an end when most others thought I would never manage. It really helped a lot to have your support. Thanks for the encouragement, the discussions, the reading and for helping me manage to get into the plane to Brazil in time! Jan and Nicolo it was pleasure to have worked with both of you!

Many thanks to Martijn Mulders, who helped me a lot to get started on the W mass measurement and who helped me get settled in The Netherlands. Martijn many thanks for teaching me so much about the ideograms and the W mass when I know you were very busy writing your thesis! Thanks for helping me sort out all the paper work I needed to do when I moved to The Netherlands. Mandarijntje, I am very happy to have you in my committee!

While I was at CERN I could count on the help from many colleagues. Jan van Eldik, who I was lucky to have as an office mate, thank you so much for helping me out with all programming related questions I had (which were many)! Thanks to Daniel Jeans for helping me understand the IDA selection and for answering my questions about it long after he left Delphi. Thanks to Chris Parkes for the useful input and specially for all the help with the MLBZs!

Life in Geneva was great fun and lots of people contribute to that. Jeffrey, Makoto and Paul, my money friends, I had great fun with you guys! Tony and Freddie, Jan van Eldik and Maria, Juan Palacios, Mark Feathers, Tainá Meirelles, you all made Geneva a place where I will always want to go back to. Thank you to Blandine, for the good times in Geneva too, but also for the friendship that is still there after so many years.

You all know that I went through some rough paths during my PhD. There are some people who helped a great deal to keep a *mens sana in corpore sano*. I could call them my healing team. Hein Halfschepel, Steven van Rijn and Martin Keuper, it is very simple, no way I would have finished without your help!

The roughest of all paths was obviously losing my mother. I would like to thank all my friends for the support I got, you were all great! Special thanks here go to Fátima, Sandra and Jord, Marc, and Tainá.

Still on the tough times, a general thank you for all the people who thought I could pull this off. There were times I thought I would never finish, having the support of my friends was crucial to me! Many thanks to all of my friends for that!

Back to happier times. Thanks to the crowd at Nikhef who made it a nice place to go to. Alex Koutsman, Andrea, Aras, Barbara, Despoina, Gabriel, Gordon, Jeff, Manouk, Menelaos, Patrick, Niels Tuning, Nigel, Siphon and Zdenko, you guys just rock! Also big thanks to my last office mates for standing me on the last months of writing, Despoina and Ante, you two were great! Thanks again to Manouk. Chica, the train trips without you are not the same, you will always be my favorite companion in the stilted coupes! Andrea, aka Chiquilina, thanks for hanging in there with me till the end! And to you two chicas, thanks for being my paraninfen.

Once again thanks to Juan Palacios. Juanito, thanks for all the useful discussions on the W mass and big thanks for all the good times we spent together in Geneva and in Amsterdam!

I would like to thank my friend Jeff Templon for helping me whenever I needed and for being my friend!

Many thanks to the gladies, Cláudia, Katell and Kateryna for the many lunches and dinners together and for your friendship of course! It was very helpful being able to share the worries of doing a PhD with you girls.

Thank you to Daniël Boer and Beatriz Noheda for the many good times we had together and also for the support I got from you guys! Thanks to Daniël Boer once more for finding out the truth about Yukawa.

Nessa and Andrea, I hope you two know how important a role you played in this PhD, thank you so much for always being there for me! Sandra, who was there from the very beginning, thank you for your friendship! It feels very good to have someone like you I can always count on!

A huge thank you to Fátima, a friend for good and bad moments. Fátima, eu me considero uma pessoa de muita sorte por ter uma amiga tão leal como você, obrigada por tudo!

I also got a lot of support from my other Brazilian friends here in Holland. Dani, Luana e Paty; meninas, muito obrigada pelo apoio, carinho e compreensão.

A big thank you to Kaia and Rego, who were originally Daniël's friends. I am privileged and honoured to be able to call you my friends! Musi-musi.

All computer related problems, which of course tend to increase the less time you have, were taken care of by a group of very nice guys! Jan van Eldik, Olof Barring, Richard Gokieli

---

and Ulrich Schwickerath, you guys are my heroes!!! Thank for all your help!

Despite the distance, there are lots of people in Brazil who also played an important part in this enterprise. My former supervisor, Leandro de Paula, thank you for everything! Pra mim você sempre continuará sendo meu orientador. Tatinha querida, minha amiga do coração, obrigada pela força e por seu apoio incondicional. Tinex, mesmo longe, sempre tive absoluta certeza de poder contar com você.

Thanks to my high school teacher; Jorge, obrigada por abrir meus olhos para o mundo da física. Many thanks to my three classmates at University. Dedé, Lili e Rafa, não importa quão grande seja a distância, eu sempre vou trazê-los comigo no coração.

Elisa, pra você o meu super obrigada pela capa da tese, fiquei muito feliz por você ter aceitado fazer a capa, mas mais feliz ainda com o resultado final. Mas sobretudo o meu obrigada pela sua amizade! Aos meus irmãos queridos, Dani e Darlan, eu tenho um orgulho enorme de tê-los como irmãos, amo vocês! Pai, muuuuito obrigada pelo amor e por tudo o que você fez por mim!

À minha mãe, que infelizmente não está mais aqui; mãe, pra você eu dedico essa tese. Obrigada pelo seu amor incondicional, mesmo depois da sua morte eu nunca deixei de senti-lo e com certeza, mesmo depois da sua morte eu nunca vou deixar de te amar!<sup>1</sup>

The last person to be thanked is of course the most important one. Daniël, no way I can express on paper the love I have for you and my gratitude for all you have done for me! I consider myself the luckiest person on earth for having you in my life. You were always on my side no matter how tough things got. Having had your support through this journey meant the world to me! Thank you also for all the scientific help, it was very learnful and helpful to have a W mass expert at home. Thank you so much for your patience and support especially towards the end. I would never have managed without you! Te amo mais que tudo nessa vida!

---

<sup>1</sup>To my mother, who unfortunately is no longer here, mum, I dedicate this thesis to you. Thank you for the unconditional love, even after your death I never stopped feeling it and certainly even after your death I will never stop loving you!